UNIVERSITY OF LIVERPOOL

Development of Spectral Domain Optical Coherence Tomography for Pharmaceutical and Medical Application

Thesis submitted in accordance with the requirements of the University of Liverpool for the degree of Doctor of Philosophy

by

Yue Dong

March 2015

Department of Electrical Engineering & Electronics

Acknowledgments

This thesis could not be finished without the help and support of many people who are gratefully acknowledged here. Firstly, I would like to express my deepest gratitude to my supervisor, Dr. Yaochun Shen. He has always given me valuable ideas, suggestions and comments with his profound knowledge and rich research experience and guided me in the right direction. He was easily available and accessible and willing to discuss whenever I needed his guidance and support. Then, I owe special thanks to Dr. Lu Gan and Dr. Vahid Abolghasemi for supporting part of this research. I could not accomplish my thesis without their kind support and valuable suggestions. I also would like to thank Prof. Yi Huang and Dr. Yalin Zheng for supporting and guiding me in my research. I have learnt from them a lot not only about research, but also about the professional ethics.

I would like to thank my postgraduate colleagues, who never failed to give me great encouragement and suggestions. Special thanks should go to Dr. Hao Shen, Mr. Lin Liu and Miss Chen Li for their kindly supports and suggestions.

Last but not least, I would like to thank my family members, especially my wife, Lin Zhang, and my parents, Mr. Fucai Dong and Mrs Guoping Zhao. My wife has to live alone for such a long time when I was busy in doing research at the University. This thesis would not be possible without her encouragement. Without my parents' support during my whole research duration, I also could not be able to achieve my goals.

Abstract

Spectral-domain optical coherence tomography (SD-OCT) is a type of non-destructive imaging technique that is capable of resolving the inner structure of a sample with micrometre spatial resolution. SD-OCT is based on low coherence interferometry. It utilises a spectrometer to grab the spectral interferogram between the back reflected/scattered light from a reference mirror and a sample. The depth profile, which carries the sample inner structure information, is then generated by a data interpolation and Fourier Transform (FT).

Functional coating of solid oral dosage forms optimises the release profile of active pharmaceutical ingredient (API) and results in a desirable API absorption rate in the human body. Therefore, the characterisation of the coating structure is significant in the pharmaceutical industry. In order to resolve the coating structure of film coated pharmaceutical tablets off-line, a general-purpose free space SD-OCT system is firstly implemented. The axial and lateral resolution of the SD-OCT system is 2.6 µm and 16 µm respectively, and it requires a mechanical lateral scan by rotating a galvo mirror to generate a cross-sectional image. The coating thickness quantified by the mean depth profile is in the range of 30 µm to 220 µm.

The diameter of a pharmaceutical pellet is typically at the sub-millimetre scale, which leads to stronger scattering compared with a tablet with typical dimensions larger than 5 mm. The galvo mirror based scanning system sweeps the sample beam on the sample to perform the mechanical lateral scan. It increases the incident angle of the sample beam and collects less backscattered sample beam at the side of the pellet sample. To address this issue, a translation stage replaces the galvo mirror to move the pellet sample. The sample beam always stays at the centre of the lens, thus more backscattered light from a sample can be collected. Moreover, to realise the online measurement, a fibre based SD-OCT system with a flexible probe head was

implemented to reduce the system dimensions. The fibre based SD-OCT system has the advantage of compactness and portability. The fibre sensor head can be easily integrated into a pharmaceutical coater.

In the well-established clinical application of OCT, one has to minimise the motion artefact associated with the movement of human eyes to assess the corneal structure in vivo. One solution to solve this problem is to grab multiple A-scans simultaneously. A single-shot SD-OCT system with a two-dimensional detector array is built to grab multiple spectral interferograms in parallel. The single-shot SD-OCT system is successfully applied to evaluate the corneal thickness under different pressures. Furthermore, we demonstrated for the first time that change in corneal thickness variance down to nanometre resolution can be quantified using the phase information of the complex depth profile. We are in the process of applying for a patent to protect the developed technology. Built on the success of this work, a major project has also been funded (NIHR i4i scheme) to develop this technology further for medical applications.

The algebraic reconstruction technique (ART) based optical coherence tomography (OCT) allows reconstruction of the depth profile of a sample directly in the wavelength domain using the sparse approximation method. We propose a fast sparse approximation algorithm which combines the orthogonal matching pursuit (OMP) method with a spectrum split approach for the reconstruction of the depth profile of a sample. As a demonstration, we applied ART-OCT to study pharmaceutical tablet coatings in a thickness range of 30-183 μm. We showed that the proposed reconstruction method has low computational complexity which leads to a much faster reconstruction speed as compared with the more widely used l1-optimisation method. Furthermore, the novel combination of the OMP method with the spectrum split approach has also led to over 3.7dB improvement in signal to noise ratio (SNR) of the reconstructed cross-sectional image of the coated tablets. This work has been presented at 2014 UCL-Duke Workshop on Sensing and Analysis of High-

Dimensional Data, and a paper based on this work has been drafted and will be submitted for journal publication.

Table of contents

List of Figures

Abbreviation:

ADC: analogue to digital converter

API: active pharmaceutical ingredients

ART: algebraic reconstruction technique

CCD: charge coupled device

CCT: central corneal thickness

CL: cylinder lens

CMOS: complementary metal-oxide semiconductor

CS: compressive sensing

CT: computed tomography

DAQ: data acquisition

DOF: depth of field

ELM: external limiting membrane

FD: Fourier domain

FF-OCT: full field optical coherence tomography

FFT: fast Fourier Transform

FT: Fourier transform

FWHM: full width at half maximum

HPMC: hydroxypropyl

IV-US: intravascular ultrasound

LCI: low coherence interferometry

LED: light emitting diode

MCC: microcrystalline cellulose

methylcellulose

MRI: magnetic resonance imaging

NA: numerical aperture

NMSC: non-melanoma skin cancer

OCT: optical coherence tomography

OMP: orthogonal matching pursuit

ONL: outer nuclear layer

OPD: optical path length difference

OPL: outer plexiform layer

PAT: process analytical tool

PS-OCT: polarization sensitive optical coherence tomography

PZT: piezoelectric

RIN: relative intensity noise

RM: reference mirror

RNFL: retinal nerve fibre layer

RPE: retinal pigment epithelium

SD: spectral domain

SD-OCPM: spectral domain optical coherence phase microscopy

SDPM: spectral domain phase microscopy

SLD: superluminescence laser diode

SNR: signal to noise ratio

SS: swept source

TD: time domain

TPI: terahertz pulsed imaging

2D: two-dimensional

3D: three-dimensional

Chapter 1 Introduction

1.1 Introduction to optical coherence tomography

Optical coherence tomography (OCT) is a non-invasive imaging technique that provides high spatial resolution cross-sectional images by measuring the backscattered light from the sample object and the reference mirror. Normally, an OCT system has an axial resolution of 1-15 μm which is one or two orders of magnitude lighten than many other imaging techniques including ultrasound, magnetic resonance imaging (MRI), terahertz pulsed imaging (TPI), and X-ray computed tomography (CT). On the other hand, the imaging depth of an OCT system is typically a few millimetres, which is deeper than some other high resolution imaging techniques such as confocal microscopy. Therefore, as shown in Fig. 1.1 (a), OCT fills a gap between ultrasound and microscopy. Furthermore, OCT could achieve a high imaging speed of more than 300k A-scans per second. Hence, OCT is a practical imaging tool for real-time applications. Figure 1.1 (b) shows the development of OCT A-scan acquisition speed.

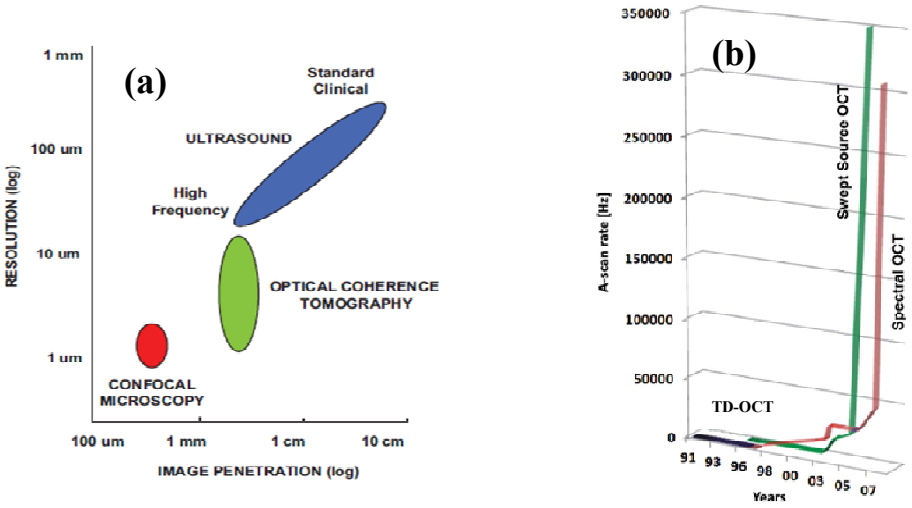

Figure 1.1 (a) Imaging depth and axial resolution of different imaging techniques. (b) A-scan acquisition speed development of OCT. Figure reprinted from: M. Wojtkowski, "High-speed optical coherence tomography: basics and applications," Applied Optics, 49: D30-D61, (2010) copyright @ 2010 Optical Society of America.

Initially, OCT was developed in time domain (TD) and employed for ophthalmic applications [1]. Since the original work, TD-OCT has been applied for various biomedical applications including dermatological diagnosis [2], dentistry [3], and endoscopy [4]. In the past decade, Fourier domain (FD) OCT including spectral domain (SD) and swept source (SS) OCT have been developed. It has been proven that FD-OCT has better signal to noise ratio (SNR), sensitivity and imaging speed than TD-OCT [5]. Therefore FD-OCT gradually replaced TD-OCT. It has been used in a larger amount of applications, not only for medical diagnosis but also in many nonmedical fields, such as thickness measurement of paper [6], fluttering foils [7], characterisation of laser-drilled holes [8], investigation of polymer solar cells [9] and pharmaceutical tablet coating imaging [10-12].

1.2 Motivations

1.2.1 Pharmaceutical application

The coating of solid pharmaceutical dosage forms has many functions including

masking bitter tastes and unacceptable odours, improving aesthetic appearance, increasing stability and separating incompatible substances [13]. More importantly, the coating controls the release of the active pharmaceutical ingredient (API) and can be designed to achieve desirable API absorption rate in the human body [14]. To ensure consistency and quality, it is necessary to quantify the coating thickness during the coating operations in the manufacturing process.

Traditionally, only the average coating thickness of a batch of solid dosage forms could be evaluated by calculations of the weight gain in respect to the amount of coating solution applied [15]. To precisely characterise and control the pharmaceutical coating structure in the coating process, non-destructive imaging tools are required. Since most pharmaceutical excipients used in film coating are either transparent or semi-transparent in the terahertz frequency range [16], TPI [16-19] has proven to be a practical tool for evaluating the coating structure on tablets with diameter larger than 5 mm. However, due to its relatively low spatial resolution (~200 μm) which is limited by the relatively long wavelength (0.1 mm to 1 mm) of terahertz radiation, TPI can only resolve coating structures thicker than 40 μm [11]. However, OCT usually uses near infrared light, which has a much shorter wavelength as compared with terahertz radiation, thus OCT has an intrinsically higher spatial resolution than the terahertz imaging method. Consequently, OCT is capable of characterising the fine coating structure of much smaller sized pellets and thin coating layer less than 40 μm of pharmaceutical tablet.

1.2.2 Medical application

Central corneal thickness (CCT) is an important parameter in both diagnostic and therapeutic assessment such as planning karetorefractive surgical procedures and early diagnosis of glaucoma [20-24]. To date, ultrasound pachymetry is the most commonly used tool for clinical evaluation of cornea thickness. However, there are many limits to the use of ultrasound pachymetry. Firstly, it is an invasive method as it requires its probe to make contact with the patient's eye. Secondly, ultrasound pachymetry measures only the thickness of a single point on the cornea. Finally, the resolution of the ultrasound pachymetry is several tens of micrometres. Therefore,

many other high resolution and non-invasive imaging techniques, including specular microscopy [25], confocal microscopy [26], scanning slit topography and OCT [27] have been proposed for evaluation of the CCT.

The conventional SD-OCT system scans the sample point after point laterally to generate a cross-sectional image. Hence it cannot image 2-dimentional (2D) dynamics. In our study, a single shot SD-OCT configuration [28] based on a 2D CMOS camera was developed to image the human cornea and to evaluate the cornea thickness and its dynamics. The single-shot SD-OCT system measures multiple spectra in a single exposure without any mechanical depth and lateral scanning process. Therefore, the single-shot SD-OCT system improves the imaging speed and is free of both axial and lateral motion artefacts.

1.2.3 Algebraic reconstruction technique based optical coherence tomography

In a SD-OCT system, the imaging depth is limited by the spectral resolution of the spectrometer. A high-resolution spectrometer is thus required in order to achieve sufficient large imaging depth. On the other hand, the spectrometer has to be broadband to achieve high axial resolution. Therefore there is an ultimate trade-off between the axial resolution and imaging depth because the high resolution and broadband spectral range cannot always be achieved simultaneously for a given spectrometer with a fixed number of sensor elements [29].

The algebraic reconstruction technique (ART) allows a high axial resolution and large imaging depth to be achieved simultaneously. More importantly, the ART-OCT method might be able to significantly reduce the data acquisition time and volume because it requires fewer measurement points than is conventionally required, in a similar way as the recently developed compressive sensing (CS) technology [29-35]. However, the widely used L1- optimisation approach in ART-OCT and CS-OCT is a time-consuming approach. We used a greedy sparse optimisation approach to reconstruct OCT images. It improves the reconstruction speed and SNR compared with L1-optimisation.

1.3 Organisation of the thesis

Chapter 2 introduces the principle and applications of OCT techniques. Firstly, a brief introduction of the TD-OCT technique is made. Then the principle of SD-OCT is discussed including its mathematical model, signal processing method, imaging depth, spatial resolution, SNR, and sensitivity. In addition, practical aspects such as light sources and detectors are discussed. After that, this chapter shows many different modalities and applications of the OCT system.

Chapter 3 shows the implementation of two in-house free space SD-OCT configurations, namely the single-point SD-OCT and the single-shot SD-OCT system. The setups of both systems are shown firstly. The single-shot SD-OCT measurement does not require the lateral scan that is essential in single-point SD-OCT. The performances of the two systems, including axial resolution, lateral resolution and imaging depth, were characterised by imaging glass slides. Finally, human finger-tips, cornea and onion peel were imaged by the two systems to test their capability of imaging real-world samples.

Chapter 4 reports the application of SD-OCT for imaging and quantifying the coating structures of pharmaceutical tablets and small sized pellets. In the experiments, the coated tablets and pellets were imaged by both the single-point and single-shot SD-OCT systems. The mean coating thicknesses are evaluated from the mean depth profiles. In addition, the effect of increased quantisation noise due to the reduced ADC bit depths is discussed. Finally, a fibre based SD-OCT configuration was implemented for online evaluation of multiple layered coating structures.

Chapter 5 reports the application of the single-shot SD-OCT system for quantifying the CCT of both the human and bovine corneas. In this chapter, five human donor and bovine corneas were measured by our in-house single-shot SD-OCT system under three different saline solution pressures. Apart from the CCT, the corneal thickness

dynamics and surfaces movement are determined in nanometre scale by the phase information extracted from the Fourier transformed complex depth profile.

Chapter 6 discusses the ART/CS-OCT. It employs sparse optimisation algorithms such as L1-optimisation and OMP, to reconstructed OCT depth profile and images by only a fraction of measured spectra data points. These reconstruction techniques break the Shannon-Nyquist sampling theorem and improve imaging depth and axial resolution simultaneously. OCT images of coated tablets are reconstructed by both L1-optimisation and OMP. The performances of the two reconstruction algorithms are characterised and compared.

Chapter 7 summarises the work and discusses future work.

1.4 List of Publications

Journal papers

1. H. Shen, L. Gan, N. Newman, ***Y. Dong***, C. Li, Y. Huang and Y. C. Shen (2012) ñSpinning disk for compressive imaging,ò Optics Letters vol 37 issue 1 pp 46-48.
2. C. Li, J.A. Zeitler, ***Y. Dong***, Y.C. Shen (2014) ñNondestructive evaluation of polymer coating structures on pharmaceutical pellets using full field optical coherence tomography,ò J. Pharmaceutical Sciences vol 103 pp 161-166.
3. ***Y. Dong***, L. Gan, C. Li, V. Abolghasemi, Y.C. Shen (2014) ñAssessment of pharmaceutical tablets coating thickness by algebraic reconstruction technique based optical coherence tomography,ò (to be submitted)
4. ***Y. Dong***, Y.L. Zheng, Y.C. Shen (2014) ñDevelopment of an ultrasensitive single-shot OCT system for medical application,ò (to be submitted)

Conference paper and posters:

5. C. Li, ***Y. Dong*** and Y.C. Shen, ñCharacterization of tablet coating using infrared optical coherence tomography,ò IoP Photon 12 (Durham, 2012).
6. ***Y. Dong***, L. Gan and Y.C. Shen, ñOrthogonal matching pursuit to reconstruct optical coherence tomography image,ò 2014 UCL-Duke Workshop on Sensing and Analysis of High-Dimensional Data (London, 2014).
7. L. Liu, L. Gan, ***Y. Dong*** and Y. C. Shen, ñTerahertz imaging via block based compressive sensing,ò 2014 UCL-Duke Workshop on Sensing and Analysis of High-Dimensional Data (London, 2014).

References:

1. D. Huang, E.A. Swanson, C.P. Lin, J.S. Schuman, W.G. Stinson, W. Chang, M.R. Hee, T. Flotte, K. Gregory, C.A. Puliafito, J.G. Fujimoto, "Optical coherence tomography," Science **254**:1178ï 1181 (1991).
2. G. Häusler and M.W. Lindner, ñCoherence radar and spectral radar ð New tools for dermatological diagnosis,ò J. Biomed. Opt. **3**, 21-31 (1998).
3. F.I. Feldchtein, G.V. Gelikonov, V.M. Gelikonov, R.R. Iksanov, R.V. Kuranov, A.M. Sergeev, N.D. Gladkova, M.N. Ourutina, J.A. Warren, D.H. Reitze, ñIn vivo OCT imaging of hard and soft tissue of the oral cavity,ò Opt. Express **3**: 239-250 (1998).
4. A. M. Sergeev, V. M. Gelikonov, G. V. Gelikonov, F. I. Feldchtein, R. V. Kuranov, N. D. Gladkova, N. M. Shakhova, L. B. Snopova, A. V. Shakhov, I. A. Kuznetzova, A. N. Denisenko, V. V. Pochinko, Yu. P. Chumakov, and O. S. Streltzova, ñIn vivo endoscopic OCT imaging of precancer and cancer states of human mucosa,ò Opt. Express **1:** 432-440 (1997).
5. R. Leitgeb, C. Hitzenberger, and A. Fercher, ñPerformance of Fourier domain vs. time domain optical coherence tomography,ò Opt. Express **11**: 889-894 (2003).
6. T. Fabritius, E. Alarousu, T. Prykari, J. Hast, R. Myllyla, ñCharacterisation of optically cleared paper by optical coherence tomography,ò Quantum Electron **36**: 181-187 (2006).
7. A. Nemeth, R. Gahleitner, G. Hannesschlager, G. Pfandler, M. Leitner, ñAmbiguity-free spectral-domain optical coherence tomography for determining the layer thicknesses in fluttering foils in real time,ò Opt. Laser Eng. **50**: 1372-1376 (2012).
8. P.J.L. Webster, J.X.Z. Yu, B.Y.C. Leung, M.D. Anderson, V.X.D. Yang, J.M. Fraser, ñIn situ 24 kHz coherent imaging of morphology change in laser percussion drilling,ò Opt. Lett. **35**: 646-648 (2010).
9. L. Thrane, T.M. Jørgensen, M. Jørgensen, F.C. Krebs, ñApplication of optical coherence tomography (OCT) as a 3-dimensional imaging technique for roll-to-roll coated polymer solar cells,ò Sol. Energy. Mater. Sol. Cells. **97**:181-185 (2012).
10. J.M. Mauritz, R.S. Morrisbv, R.S. Hutton, C.H. Legge, C.F. Kaminski, ñImaging

pharmaceutical tablets with optical coherence tomography,ò J. Phar. Sci. **99**: 385-391 (2010).

11. S. Zhong, Y.C. Shen, L. Ho, R.K. May, J.A. Zeitler, M. Evans, P.F. Taday, M. Pepper, T. Rades, K.C. Gordon, R. Muller, P. Kleinebudde, ñNon-destructive quantification of pharmaceutical tablet coatings using terahertz pulsed imaging and optical coherence tomography,ò Opt. Laser Eng. **49**: 361-365 (2011).
12. D.M. Koller, G. Hannesschlager, M. Leitner, J.G. Khinast, "Non-destructive analysis of tablet coatings with optical coherence tomography," Eur. J. Pharm. Sci. **44**:142-148 (2011).
13. G.C. Cole, Introduction and overview of pharmaceutical coating, In: G. Cole, J. Hogan, A. Michael (Eds.), Pharmaceutical Coating Technology, Taylor & Francis Ltd, Philadelphia, 1995, pp. 1ï 5.
14. G.M. Jantzen, J.R. Robinson, Sustained and controlled-release drug delivery systems, In: G.S. Banker, C.T. Rhodes (Eds.), Modern pharmaceutics, Marcel Dekker, New York, 2002, pp. 501ï 528.
15. J.D. Perez-Ramos, W.P. Findlay, G. Peck, K.R. Morris, "Quantitative analysis of film coating in a pan coater based on in-line sensor measurements," AAPS PharmSciTech **6**: 127ï 136 (2005).
16. Y.C. Shen, P.F. Taday, "Development and application of terahertz pulsed imaging for non-destructive inspection of pharmaceutical Tablet," IEEE J. Sel. Top. Quant. Electron. **14**: 407-415 (2008).
17. Y.C. Shen, "Terahertz pulsed spectroscopy and imaging for pharmaceutical applications: A review," Int. J. Pharm. **417**: 48-60 (2011);
18. Y.C. Shen and B.B. Jin, Terahertz applications in pharmaceutical industry and science, In: D. Saeedkia (Eds.), Handbook of Terahertz Technology for Imaging, Sensing and Communications, Woodhead Publishing Ltd, Cambridge, 2013, pp. 579-614.
19. J.A. Zeitler, Y.C. Shen, C. Baker, P.F. Taday, M. Pepper, T. Rades, "Analysis of coating structures and interfaces in solid oral dosage forms by three dimensional terahertz pulsed imaging," J. Pharm. Sci. **96**: 330ï 340 (2007).
20. R.C. Wolfs, C.C. Klaver, J.R. Vingerling, D.E. Grobbee, A. Hofman, P.T. deJong, "Distribution of central corneal thickness and its association with intraocular pressure: the Rotterdam Study," Am. J. Ophthalmol. **123**:767ï 772 (1997).

21. L.W. Herndon, S.A. Choudhri, T. Cox, K.F. Damji, M.B. Shields, R.R. Allingham, "Central corneal thickness in normal, glaucomatous, and ocular hypertensive eyes," Arch. Ophthalmol. **115**:1137ï 41 (1997).
22. W.A. Argus, "Ocular hypertension and central corneal thickness," Ophthalmology **102**: 1810ï 1812 (1995).
23. F.A. Medeiros, P.A. Sample, L.N. Zangwill, C. Bowd, M. Aihara, R.N. Weinreb, "Corneal thickness as a risk factor for visual field loss in patients with preperimetric glaucomatous optic neuropathy," Am. J. Ophthalmol. **136**: 805ï 13 (2003).
24. F.A. Medeiros, P.A. Sample, R.N. Weinreb, "Corneal thickness measurements and visual function abnormalities in ocular hypertensive patients," Am. J. Ophthalmol. **135**:131ï 137 (2003).
25. L.J. Módis, A. Langenbucher, B. Seitz, "Corneal endothelial cell density and pachymetry measured by contact and noncontact specular microscopy," J. Cataract. Refract. Surg. **28:**1763ï 1769 (2002).
26. B.R. Masters, G. Kino, Confocal microscopy of the eye. In: Masters BR, ed. Non-invasive Diagnostic Techniques in Ophthalmology. NY: Springer-Verlag NY Inc, New York, 1990, pp: 152ï 71.
27. Y. Feng, T.L. Simpson, "Comparison of human central cornea and limbus in vivo using optical coherence tomography," Optom. Vis. Sci. **82**:416ï 419 (2005).
28. B. Grajciar, M. Pircher, A.F. Fercher, R.A. Leitgeb, "Parallel Fourier domain optical coherence tomography for in vivo measurement of the human eye," Opt. Express **13**:1131-1137 (2005).
29. X.A. Liu, and J.U. Kang, ñCompressive SD-OCT: the application of compressive sensing in spectral domain optical coherence tomography,ò Opt. Express **18**, 22010-22019 (2010).
30. C.Y. Liu, A. Wang, K. Bizheva, P. Fieguth, and H.X. Bie, ñHomotopic, non-local sparse reconstruction of optical coherence tomography imagery,ò Opt. Express **20**, 10200-10211 (2012).
31. S. Schwartz, C.Y. Liu, A. Wang, D.A. Clausi, P. Fieguth, and K. Bizheva, ñEnergy-guided learning approach to compressive FD-OCT,ò Opt. Express **21**: 329-344 (2013).

32. D.G. Xu, N. Vaswani, Y.Huang and J.U. Kang. ñModified compressive sensing optical coherence tomography with noise reduction,ò Opt. Lett. **37**: 4209-4211 (2012).

33. N. Zhag, T.C. Ho, C.M. Wang, T.Y. Chen, J.G. Zheng, and P. Xue, ñCompressed sensing with linear-in-wavenumber sampling in spectral domain optical coherence tomography,ò Opt. Lett. **37**: 3075-3077 (2012).

34. R. Nayak, and C.S Seelamantula, ñOptimal sparsifying bases for frequency-domain optical coherence tomography,ò Opt. Lett. **37**: 4907-4909 (2012).

35. L.Y. Fang, S.T. Li, Q. Nie, J.A. Izatt, C.A. Toth, and S. Farsiu, ñSparsity based denoising of spectral domain optical coherence tomography images,ò Biomed. Opt. Express **3**: 927-942 (2012).

Chapter 2 Background

2.1 Early development of OCT

OCT is based on the low coherence interferometry (LCI) principle. The LCI technique was developed by Fercher and Roth for the application of in vivo human eye length measurement [1-2]. They recorded the sample depth structure as a sequence of partial time-coherence interferograms generated by the back reflected light from sample object and a moving reference mirror in TD. In 1990, Fercher et al. generated a 2-D cross sectional eye fundus structure data by adjacent LCI depth scans [3]. Then, in 1991, Huang et al. published a 2-D cross-sectional image of a human eye fundus [4]. After that, the first two in vivo OCT images were generated independently by Fercher et al. in Vienna [5] and Swanson et al. in MIT [6]. Both of the image data acquisition processes were performed in TD.

The FD-OCT [7, 8] was developed in the mid-1990s based on the FD-LCI [9, 10] and was shown to have the same axial resolution as TD-OCT [11]. In 2003, three groups independently demonstrated that FD-OCT had better sensitivity and SNR compared with TD-OCT [12-14]. In addition, FD-OCT allowed a very high A-scan data acquisition rate as it required no mechanical scanning process in axial direction. The popularity of FD-OCT in research and medical applications has increased dramatically in recent years.

2.2 Principle of OCT

OCT measures the optical time delay of backscattered light from a semi-transparent sample object and reference mirror. Using a broadband low time coherence light source, it generates a depth reflectivity profile with an axial resolution of cellular level. In this section, the principle and implementation of both TD- and FD-OCT are discussed.

2.2.1 Time domain optical coherence tomography

The standard TD-OCT measurement is performed in a Michelson interferometer. Fig. 2.1 shows the schematic diagram of a typical TD-OCT system. The low coherence light source is divided by a beam splitter into two arms, namely the reference arm and the sample arm. In the reference arm, the reference beam is back-reflected by a reference mirror; and in the sample arm, the sample beam is back-reflected/backscattered by sample tissue. Both the back-reflected reference beam and the back-reflected/backscattered sample beam come back to the beam splitter and interfere at the exit of the interferometer. Finally, the interference beam is delivered to the detector which is a single pixel photodiode in a standard TD-OCT.

Assuming that there are N layers inside the sample object, the final electric field at the exit of the Michelson interferometer E_d can be expressed as the superposition of the electric field from the reference mirror and the sample object [15]:

$$E_d(t) = E_r(t) + \sum_{n=1}^{N} E_s(t + \tau_n) \tag{2.1}$$

where E_r and E_s are the electric field of the back-reflected/backscattered beam from the reference mirror and the sample object respectively; $\tau_n = 2nz_n/c$ is the optical time delay between the reference mirror and the n-th interface inside the sample object which is dependent on their optical path length difference (OPD) $2nz_n$. Hence the intensity detected by the photodiode is its modulus:

$$I_d = E_d(t) \cdot E_d^*(t) \tag{2.2}$$

here, $E_d^*(t)$ is the conjugate of the electric field $E_d(t)$. When substituting Eq. (2.1) into Eq. (2.2), the detected intensity could be rewritten as:

$$I_d = I_0\{a_r + \sum_{n=1}^{N} a_n + 2\sum_{n=1}^{N-1} \sqrt{a_r a_n}\, \mathrm{Re}[\gamma_{sn}(\tau_{n-1})] + 2\sum_{n=2}^{N} \sqrt{a_r a_n}\, \mathrm{Re}[\gamma_s(\tau_n)]\} \tag{2.3}$$

where I_0 is the intensity of the light source, a_r is the attenuation coefficient including the reflectivity of reference mirror R_r and coupling coefficient of beam splitter a_r, a_n is the attenuation coefficient including the reflectivity of sample tissue R_s, the coupling coefficient of beam splitter a_s and optical loss in the n-th layer of the sample [15], $\gamma(\tau)$

is the complex degree of the coherence defined by the correlation function $\tilde{u}(\tau_n)$ [15-17]:

$$\gamma(\tau_n) = \frac{\Gamma(\tau_n)}{\sqrt{I_r I_s}} = |\gamma(\tau_n)|\exp(-\omega_0 \tau_n) \tag{2.4}$$

where I_r and I_S are the optical power intensity from the reference mirror and sample respectively. The correlation function is defined as:

$$\Gamma(\tau_n) = E_r(t) E_s^*(t + \tau_n) \tag{2.5}$$

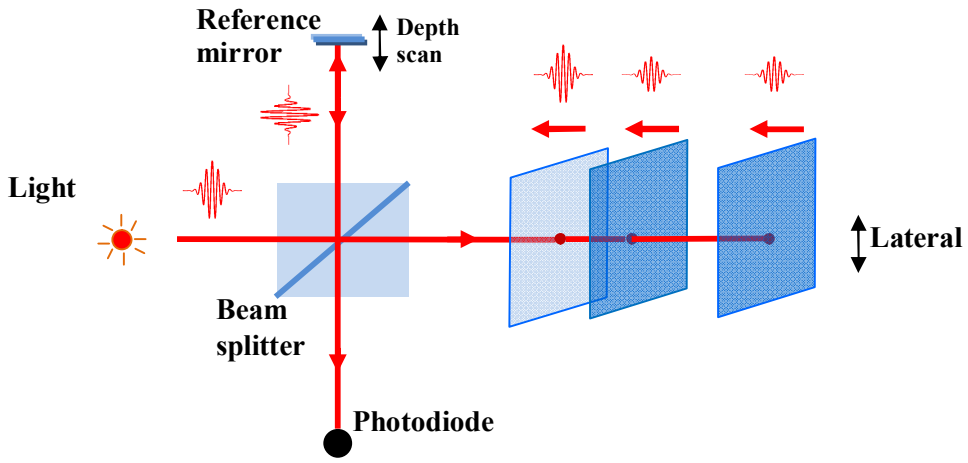

Figure 2.1 Schematic diagram of time domain optical coherence tomography.

In Eq. (2.3), the first two terms denote the light intensity reflected from the reference mirror and sample respectively. In the third term, τ_{mn} represents the optical time delay between different layer interfaces inside the sample. This term is independent of the position of the reference mirror. Hence, it always remains a constant during the depth scan of the reference mirror. The last term is the cross-correlation between the reference mirror and the sample interfaces. This term carries the inner structural information of the sample object and its value depends on the position of the reference mirror if the sample remains stationary. When the reference mirror locates at a certain position in relation to the sample object, the signal detected by the photodiode is only a single value of the depth interference pattern. In order to obtain the entire depth interferogram in relation to the position of the reference mirror, a

mechanical depth scan of the reference mirror is required. This is also called A-scan in TD-OCT. After the depth scan, the depth interferogram signal detected by the photodiode can be expressed as follows [15-17]:

$$I_d(z) = A + 2\sqrt{I_r I_s}\,|\gamma(z_r)|\cos(\phi_r) \tag{2.6}$$

where z is the variable in relation to the position of the reference mirror. A is a constant that is equal to the value of the first three terms in Eq. (2.3) and it remains a constant during the depth scan. The second term in Eq. (2.6) carries the inner structural information of the sample. Due to the broadband nature of the light source, the interference pattern could be observed only if the OPD z_n between the reference mirror and the n-th sample interface is within the coherence length of the light source. Fig. 2.2 (a) shows a simulated depth interferogram of a two-layered sample. The depth profile shown in Fig. 2.2 (b) could be demodulated by taking its Hilbert transform $\mathcal{H}(I_d)$ [18].

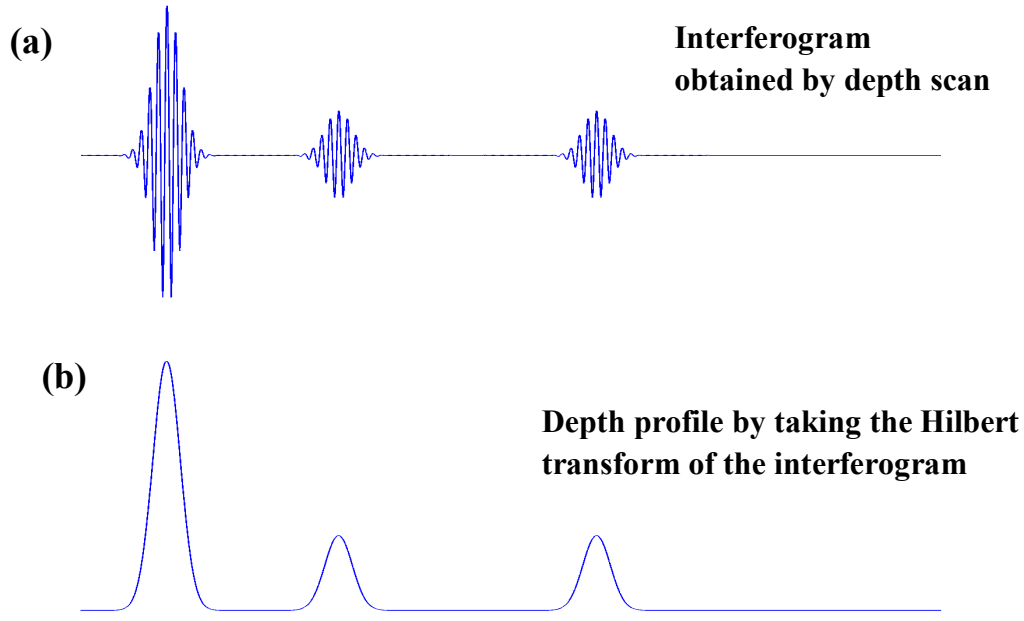

Figure 2.2 (a) A simulated depth interferogram in TD-OCT and (b) its depth profile.

Furthermore, to generate a cross-sectional (B-scan) image, hundreds of A-scans are required. Hence, the depth scan is repeated hundreds of times on adjacent lateral

positions on sample tissue. It is very time-consuming compared with the later developed FD techniques. The full-field [19] configuration based on a 2D detector array could obtain multiple depth profiles in a single depth scan, and more or less improves the measurement speed in TD-OCT. However, since FD-OCT has been proven to have better sensitivity and SNR, FD-OCT replaces TD-OCT gradually.

2.2.2 Fourier domain optical coherence tomography

Unlike TD-OCT, the FD-OCT measures the spectral interferogram between the reference mirror and the sample object rather than measuring the depth interferogram directly. The depth profile in FD-OCT is extracted by Fourier transform (FT) of the spectral interferogram and does not require any mechanical depth scan. Generally, there are two types of FD-OCT techniques. The first type is spectral domain (SD-) OCT. SD-OCT measures the spectral interferogram using a line camera based spectrometer with thousands of pixels in the wavelength domain. The second type is swept source (SS-) OCT that uses a tunable light source. In SS-OCT, the spectral interferogram is recorded by a single photodiode in the wavenumber domain. In this section, only the SD-OCT is discussed in detail because the signal processing method of the two types of FD-OCT are almost the same and most of my work is performed on SD-OCT.

The schematic diagram of a SD-OCT system is shown in Fig. 2.3. The core component is also a Michelson interferometer. In contrast to the TD-OCT, it uses a line camera based spectrometer instead of the photodiode as the detector. The Fourier domain electric field of the interferogram at the exit of the interferometer could be expressed as:

$$E_{\square}(k) = E_{\square}(k) + \sum_{\square}^{\square} E_{\square}(k) \cdot \exp(-jk\Delta z_{\square}) \tag{2.7}$$

where $k=2\pi/\lambda$ is the wavenumber, and E_r and E_s are the electrical field of the back-reflected reference beam and backscattered sample beam, respectively. The intensity of the interferogram is:

$$I_{\square} = E_{\square}(k) \cdot E_{\square}^{*}(k) \tag{2.8}$$

Substitute Eq. (2.7) into Eq. (2.8). The spectral interferogram grabbed by the spectrometer can be expressed as follows [16]:

$$I(k) = S(k)\left(R_r + \sum_n R_n + 2\sum_{n<m} \sqrt{R_n R_m}\cos[k(z_n - z_m)] + 2\sum_n \sqrt{R_r R_n}\cos(k\Delta z_n)\right) \quad (2.9)$$

I(k) is the spectral interferogram and S(ϰ) is the spectral power density of the light source. Other notations have the same physical meaning as discussed in TD-OCT. In practice, the line camera measured spectral interferogram is in wavelength domain which is inversely proportional to wavenumber in Eq. (2.9). Hence, the spectral interferogram must be converted from the wavelength domain to wavenumber domain by a data interpolation before the consequent FT.

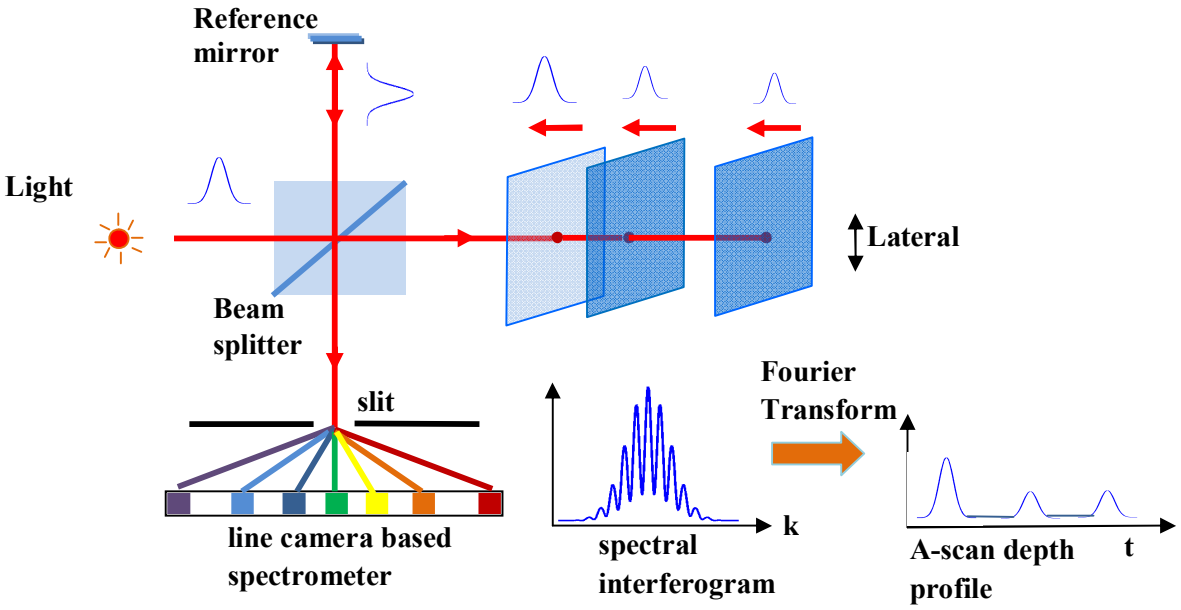

Figure 2.3 Schematic diagram of SD-OCT system.

2.2.3 Data processing in SD-OCT

After data interpolation, the depth profile is obtained by FT of Eq. (2.9) [16]:

$$\Gamma(z) = R_r + \sum_n R_n\,\Gamma(z) + \sum_{n<m} \sqrt{R_n R_m}\,\Gamma(z) \otimes [\delta(z \pm \Delta z_n)]$$

$$+ \sum_{} \sqrt{} \Gamma(z) \otimes \delta(z \pm \Delta z_{}) \quad (2.10)$$

where ũ(z) is the envelope of coherence function as determined by the FT of the spectral power density of light source. ŭ denotes the delta function and ⊗ means convolution. The first term of the depth profile is called the DC-component and the second term is the autocorrelation component produced by the self-interference between different sample interfaces. The last term is the cross-correlation that contains the inner structural information of the sample. In the TD-OCT measurement the autocorrelation and the DC terms are always a constant. However, in SD-OCT, these features will be in the depth profile, and they will contaminate the cross-sectional image. In reality, the DC peak can be easily removed by a low pass filter, but the autocorrelation peaks are not easy to remove. If the intensity of the light beam reflected from the reference mirror is much larger than the light beam backscattered from the sample object ($R_r >> R_s$), the autocorrelation peaks in depth profile will be much smaller than the cross-correlation peaks. In this case, the effect of autocorrelation could be neglected [8]. If the intensity of the sample beam is comparable with the reference beam, both the DC and autocorrelation peaks can be removed by introducing a phase shifting method [20-23]. The phase shifting can be achieved using a piezoelectric (PZT) actuator [20, 21], a tilt reference mirror [22] or an electro-optic phase modulator [23]. If the reference mirror is shifted with a phase of ű, the Fourier transformed depth profile is as follows:

$$(z) = + \Gamma(z) + \sqrt{} \Gamma(z) \otimes \delta(z \pm \Delta z_{})$$

$$+ \sum_{} \sqrt{} \Gamma(z) \otimes \delta(z \pm \Delta z_{}) \cdot \exp(\varphi) \quad (2.11)$$

By subtracting Eq. (2.11) from Eq. (2.10), the DC and autocorrelation terms are eliminated and the Eq. (2.12) will be obtained:

$$I(z, \varphi) = \sum_{} \sqrt{} \{\Gamma(z) \otimes \delta(z \pm \Delta z_{}) \cdot [1 - \exp(\varphi)]\} \quad (2.12)$$

If the shifted phase ű is equal to ´, the cross-correlation term will be amplified by a factor of 2 [21]. Fig. 2.4 shows two SD-OCT depth profiles of a transparent tape on a glass slide. The light source used is a halogen lamp. The depth profile in Fig. 2.4(a) is generated by one of the measured interferograms. Apart from the tape surface peak,

plastic/glue interface peak and glue/glass interface peak, two additional peaks representing the autocorrelation between these layers are also visible. Fig. 2.4 (b) shows the depth profile generated by the differential spectral interferogram between two measured spectra with a phase difference of ´. In this depth profile, the DC components reduced dramatically and the autocorrelation components are removed.

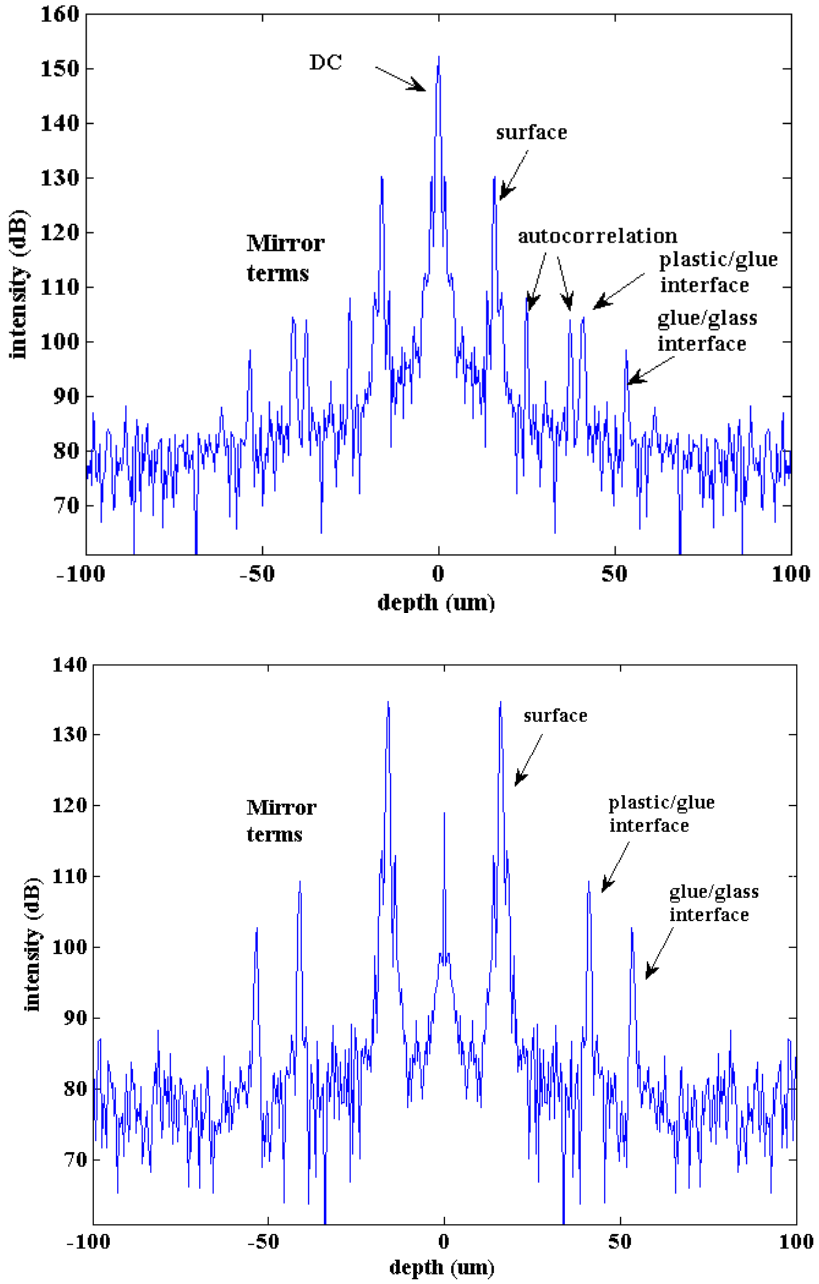

Figure 2.4 Depth profile of a transparent tape generated by (a) one of the measured spectrum, and (b) differential interferogram between two measured spectra with a phase difference.

In addition, as the measured interferogram is a real-value function, the Hermitian problem will occur [24]. Two symmetrical depth profiles will be generated, as shown in Fig. 2.4, which reduces the measurement range of SD-OCT by a factor of 2. In order to address this issue, several full-range SD-OCT techniques were proposed [24-29] by employing a phase shift mechanism to obtain the complex conjugate data of the measured spectrum. Recently, the dispersion compensation based approach has been demonstrated as a powerful tool for achieving full-range images in SD-OCT without any additional measurements [30, 31].

2.2.4 Resolution, imaging depth and depth of field

Axial resolution

Axial resolution is one of the most important parameters for characterising the performance of an OCT system because most of the biomedical application requires cellular level axial resolution. The axial resolution of an OCT system is defined by the coherence length of the light source. The coherence length of the light source can be determined by the full width at half maximum (FWHM) of its coherence function as generated by the FT of the light source. Here, we assume the spectral intensity of the used light source has a Gaussian shape in the Fourier domain. The axial resolution could be expressed as:

$$l_c = \frac{2\ln 2}{\pi} \frac{\lambda_0^2}{n} \frac{2}{\Delta\lambda} \tag{2.13}$$

where λ_0 is the centre wavelength of the light source and $\Delta\lambda$ is the light spectral FWHM in wavelength domain; n is the refractive index. The axial resolution is inversely proportional to the spectral FWHM of the light source. In other words, a broader light source results in higher axial resolution. Fig. 2.5(a) shows the SD-OCT depth profile of a transparent tape by using a halogen lamp with a spectral FWHM of 260 nm; and Fig. 2.5(b) shows the SD-OCT depth profile of the same transparent tape by using a superluminescence diode (SLD) with a spectral FWHM of 50 nm. In

practice, their axial resolutions, as determined by the FWHM of the main peak in the depth profile are 0.9 ε m and 5.5 ε m respectively.

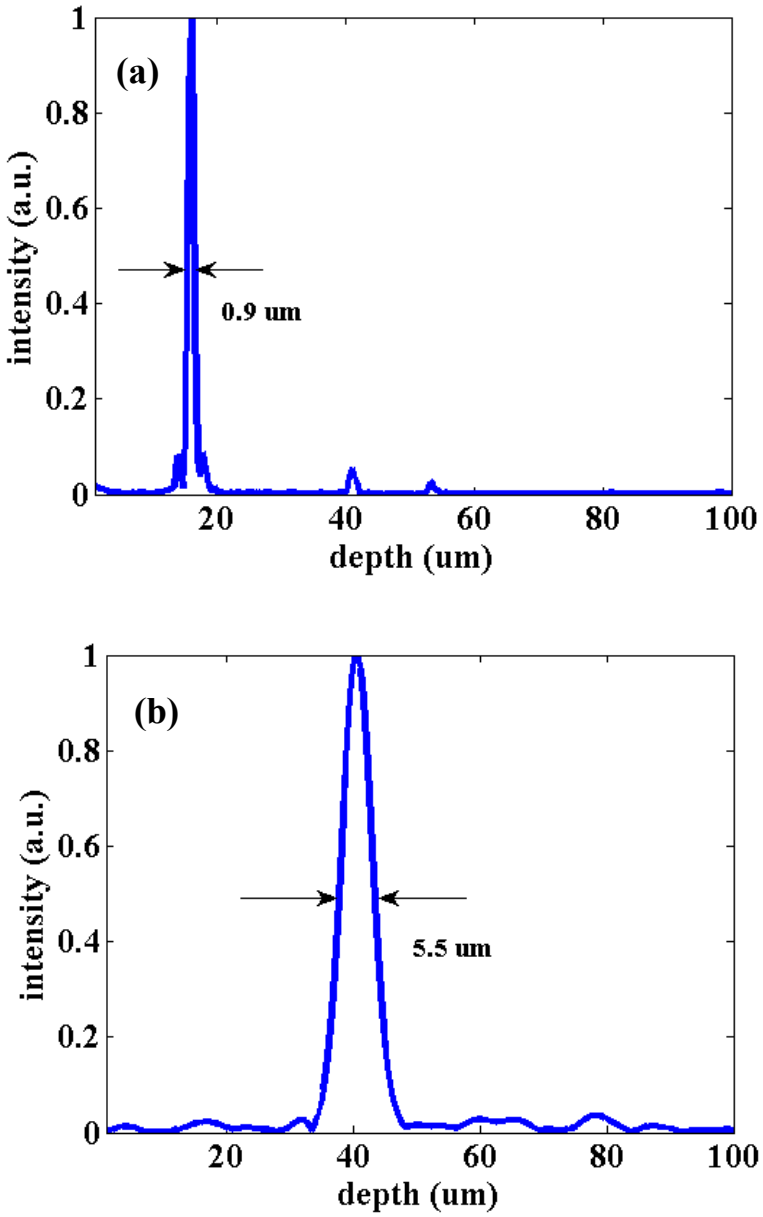

Figure 2.5 Achieved axial resolution of the SD-OCT system by using (a) halogen lamp with spectral FWHM of 260 nm and (b) SLD with spectral FWHM of 50 nm.

Lateral resolution

The lateral resolution of an OCT system is limited by the diameter of the focus spot of the sample beam, and the lateral resolution is decoupled from its axial resolution. For a Gaussian beam, the lateral resolution Δx could be defined as the FWHM of the beam waist [15, 17]:

$$\Delta x = \sqrt{2\ln 2}\, w_0 = \sqrt{2\ln 2}\,\frac{\lambda_0}{\pi \cdot NA} \tag{2.14}$$

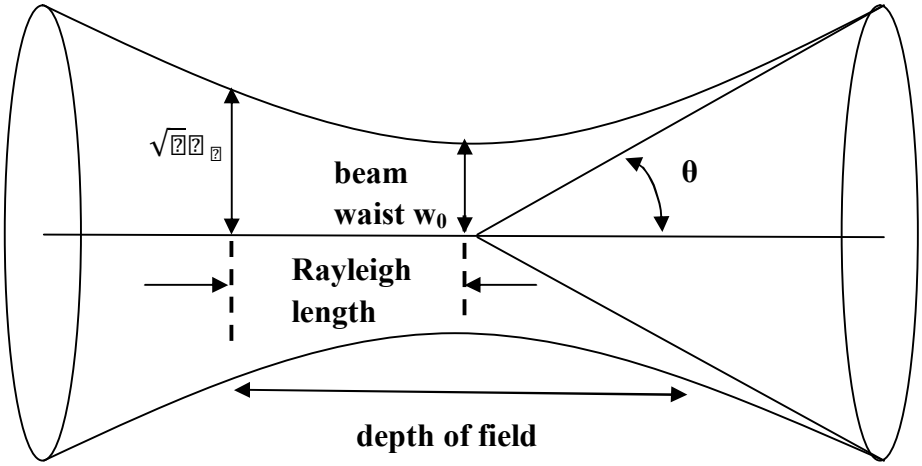

Figure 2.6 Beam width of a focus sample beam.

where w_0 is the beam waist of the sample beam and NA is the numerical aperture of the sample beam.

Depth of field

The depth of field (DOF) is double of the Rayleigh length, which is the distance along the propagation from the waist to the place where the area is doubled. Hence the DOF is given by:

$$\mathrm{DOF} = \frac{2\pi w_0^2}{\lambda_0 M^2} \tag{2.15}$$

In order to obtain higher lateral resolution, higher NA is required. However, a higher NA will reduce the DOF, and the detected signal out of the DOF will be reduced dramatically. Hence, there is a trade-off between the lateral resolution and DOF. Fig.

2.7 shows the curve lateral resolution versus DOF of a beam with a centre wavelength of 850 nm.

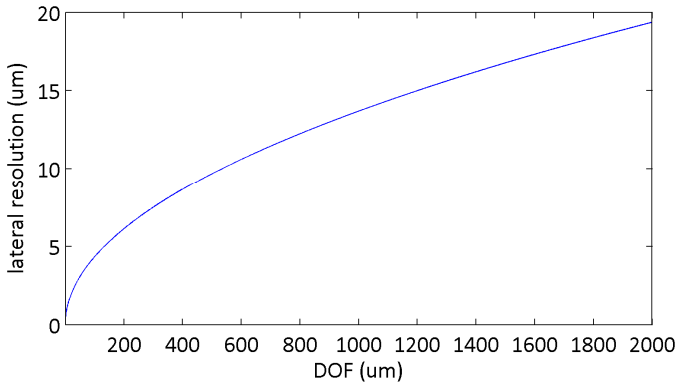

Figure 2.7 Lateral resolution versus depth of field for wavelength 850 nm.

In 1997, Schmitt et al. [32] used a dynamic focus tracking system to address the problem.

Imaging depth

The imaging depth is another important parameter for a SD-OCT system. It refers to the maximum depth that the system is capable of imaging. The imaging depth is limited by the spectral resolution of the used spectrometer. According to the Shannon-Nyquist sampling theorem, the sampling rate of the spectrometer has to be twice the highest frequency occurring in the spectral interferogram to avoid aliasing. The maximum imaging depth can be expressed as [8]:

$$z_{max} = \frac{\lambda_0^2}{4n\Delta\lambda} \tag{2.16}$$

where $\Delta\lambda$ is the spectral resolution of the used spectrometer. And n is the refractive index of sample tissue.

2.2.5 Signal to noise ratio and sensitivity

Normally, there are three noise sources in SD-OCT including shot noise, read noise and relative intensity noise (RIN):

$$\sigma_{\square}^{\square} = \sigma_{\square\square\square\square}^{\square} + \sigma_{\square\square\square\square}^{\square} + \sigma_{\square\square\square}^{\square} \tag{2.17}$$

The read noise contains Johnson noise, 1/f noise and quantisation noise. The Johnson noise is thermal and in relation to the absolute temperature of the spectrometer sensor. The variance of the Johnson noise can be expressed as [12, 16]:

$$\mathring{u}_{\square}^{\square} = 4KT\frac{\square}{\square} \tag{2.18}$$

where K is the Boltzmann constant, T is the absolute temperature, B is the electronic detection bandwidth and R is the resistance of the detection electronics.

The power spectral density of 1/f noise is inversely proportional to the frequency. Due to the high data acquisition speed of SD-OCT, the 1/f noise can be neglected. The quantisation noise depends on the bit depth of used analogue to digital converter (ADC) in the spectrometer. It can be reduced by increasing the bit depth of ADC. The quantisation noise has been proven to be much lower than the Johnson noise. Hence it can be also neglected.

The shot noise originates from the discrete nature of the photocurrent. The variance of shot noise can be expressed as [13, 16]:

$$\sigma_{\square\square\square\square}^{\square} = \frac{\square\square_{\square}^{\square}}{\square\square_{\square}\square}\frac{\square_{\square}}{\square}\left(\kappa_{\square}R_{\square} + \kappa_{\square}R_{\square}\right) \tag{2.19}$$

where ɖ is the detector quantum efficiency, q_e is the charge of electron, h is the Planck constant, $з_0$ is the centre frequency of the light source, P_0 is the average power of the light source, N is the total number of used pixels in the line camera and t is the integration time of the spectrometer. R_s and R_r are the reflectivity of the reference reflector and sample tissue respectively. $ɔ_s$ and $ɔ_r$ are the coupling coefficient of the beam splitter including optical losses.

After Fourier transforming the detected interference signal, the peak value can be expressed as [13, 16]:

$$S^{2} = \left(\frac{\eta_{det} q}{h\nu}\right)^{2} \frac{\eta_{s}}{2} \kappa_{0}^{2} R_{0} \kappa_{r}^{2} R_{r} \tag{2.20}$$

Hence, in a shot noise limited situation, the SNR can be expressed as:

$$SNR = \frac{i^{2}}{\sigma_{shot}^{2}} = \frac{\eta_{det} q}{h\nu} \cdot \frac{\eta_{s} \kappa_{0}^{2} R_{0} \kappa_{r}^{2} R_{r}}{(\kappa_{0}^{2} R_{0} + \kappa_{r}^{2} R_{r})} \tag{2.21}$$

In practical experiment, $R_s << R_r$. Hence the SNR could be simplified as:

$$SNR = \frac{i^{2}}{\sigma_{shot}^{2}} = \frac{\eta_{det} q}{h\nu} \cdot \kappa_{0}^{2} R_{0} \tag{2.22}$$

The sensitivity of the SD-OCT system is defined as the minimum reflectivity to make the SNR equal to 1.

$$Sensitivity = 10 \log_{10} \left(\frac{1}{R_{0,min}}\right) = 10 \log_{10} \left(\frac{h\nu}{\eta_{det} q} \kappa_{0}^{2}\right) \tag{2.23}$$

2.3 OCT components

2.3.1 Light sources

SLD

At present, the most commonly used light source in OCT is the SLD. Normally, a SLD has a broadband spectral distribution in the region of 10-70 nm in spectral FWHM and a centre wavelength ranging from 675 to 1550 nm [15]. In 2004, Ko et al. [33] demonstrated a high resolution OCT system by coupling two SLDs together. Its spectral FWHM was 155 nm and it led to an axial resolution of 3 εm. SLD is now the dominating light source in OCT since it is suitable for both TD- and SD- techniques.

Ti:Sapphire laser

A femtosecond Titanium-sapphire laser based OCT system has demonstrated to exhibit a near Gaussian spectral distribution with a spectral FWHM of 176 nm [34]. The axial resolution achieved using this source is around 1 εm. Afterwards, the spectral FWHM of Ti:sapphire laser increased to 260 nm that result in an ultra-high axial resolution in sub-micrometre [35].

Thermal light

Thermal light has been used in many full-field OCT systems. Due to its broadband nature, it usually generates an axial resolution less than 2 µm. In addition, the thermal light source can be used to reject the cross-talk phenomenon in full-field configuration.

2.3.2 Detector

Most line cameras used in the SD-OCT system in the past have been equipped with charge coupled device image sensors (CCD). CCD produces an excellent image quality, but it has physical limitations at high operation speeds. Recent progress in CMOS technology has resulted in CMOS sensors with superior speed performance and excellent sensitivity, noise and homogeneity characteristics. In particular, CMOS line scan sensors have fill factors of 100%, thus Potsaid et al. have demonstrated ultrahigh speed FD-OCT imaging at >300,000 axial scans per second [36]. Povazay et al. and Grulkowski et al. have analysed the performance of corresponding imaging modalities in ophthalmology [37, 38].

2.4 OCT modalities

2.4.1 Full field OCT

Full-field OCT (FF-OCT) is a modification of TD-OCT. It was first implemented on a commercial microscope body using an infrared light emitting diode (LED) [39]. In a FF-OCT system, a 2D detector array is used to replace the single pixel photodiode in a standard TD-OCT setup. The 2D detector array grabs an enface image in single exposure time. Hence, no lateral scan is required in FFT-OCT measurement. Multiple depth profiles are generated in a single depth scan that moves either the reference mirror or sample tissue axially. Therefore, it improves the acquisition speed of TD-OCT dramatically. An ultrafast FF-OCT with acquisition speed of 10 µs per pixel has been demonstrated [40].

A thermal light source is widely used in FF-OCT techniques because it can reject crosstalk in parallel acquisition systems, and the broadband nature of thermal light improves the axial resolution. A thermal light FF-OCT with sub-micrometre scale axial resolution [41] has been reported.

2.4.2 Polarisation sensitive OCT

A light wave in standard OCT configuration is treated as scalar. Hence the birefringence within a sample is not considered or measured. The first polarisation-sensitive reflectometer for birefringence characterisation was reported by Hee et al. [42] in 1992. It was later extended for 2D imaging of the birefringence within a biological sample [43]. In a polarisation sensitive OCT (PS-OCT) system, a polariser and a polarising beam splitter are placed after the source and at the exit of the interferometer respectively. Analysis of PS-OCT images is complicated and has been reviewed by de Boer et al. [44].

PS-OCT is attractive for medical applications such as retinal pigment epithelium segmentation [45]; however, it requires two expensive spectrometers. In 2009, Zhao and Izatt demonstrated a PS-OCT system using only one spectrometer [46].

2.4.3 Doppler OCT

The Doppler OCT, first reported by Chen et al. in 1997 [47], makes it possible to determine fluid flow velocity vertical to the probe beam by looking at the Doppler frequency shift. The Doppler frequency shift is introduced by the backscattered light from a moving particle in the fluid and obtained by the phase change between sequential A-scans. The measurement of a Doppler OCT is performed on a standard OCT system, either in TD or SD. In the TD technique, the Doppler frequency shift is obtained by analysis of the spectrum of the measured fringe signal using the short-time Fast Fourier Transform (FFT). In the SD technique, the Doppler frequency shift is obtained by analysis of the spectral interferogram using FFT. The velocity resolution of a Doppler OCT depends on the measurement angle and data acquisition speed. The dominating application is the monitoring of the blood flow within the skin.

2.4.4 Spectroscopic OCT

Spectroscopic and wavelength-dependent OCT has been demonstrated for performing cross-sectional tomographic and spectroscopic imaging [48]. It can also enhance image contrast, providing additional information relating to tissue pathology.

The system setup is similar to a standard TD-OCT system. The spectral information is obtained by applying wavelet transformation on the full measured depth interferogram pattern. The spectroscopic OCT requires broad bandwidth light source so that more absorption features could lie in this spectral region. However, there is a resolution contradiction between high depth resolution requiring broad wavelength spectra and high spectral resolution requiring narrow wavelength spectra.

2.5 Applications

2.5.1 Medical applications

The main field of OCT application is in ophthalmology, and OCT has now been selected as the clinical standard in ophthalmic diagnostics. Furthermore, OCT has been applied in other important biomedical fields such as cardiology, dermatology and gastroenterology.

A. Ophthalmology application

The human eye is an optical instrument with a high precision, high transmission and low scattering in the visible region. These properties match the potential of OCT [12]. Moreover, due to its non-invasive property, OCT does not require physical contact with the patientsô eyes. It compensates for the disadvantages of other ophthalmic diagnostic techniques such as fluorescein angiography and ultrasound which would cause discomfort to the patient.

The first commercial OCT system for retinal imaging [49] was developed by Carl Zeiss Meditec, and this has now become the most significant diagnostic tool for retinal diseases and glaucoma [50-53]. The high resolution retinal OCT image enables

different retinal layers to be distinguished, such as the retinal nerve fibre layer (RNFL), outer nuclear layers (ONL), outer plexiform layers (OPL), external limiting membrane (ELM), retinal pigment epithelium (RPE), photoreceptor layers and choriocapillaris [54] as shown in Fig. 2.8. Moreover, current commercial OCT systems could even quantify the thickness of RNFL over a wide retinal area in highly precise and reproducible measurements [45-59]. As the thickness of RNFL is a sensitive indicator of glaucomatous damage, RFNL thickness quantification allows identification of focal defects in earlier stages of glaucoma [59, 60].

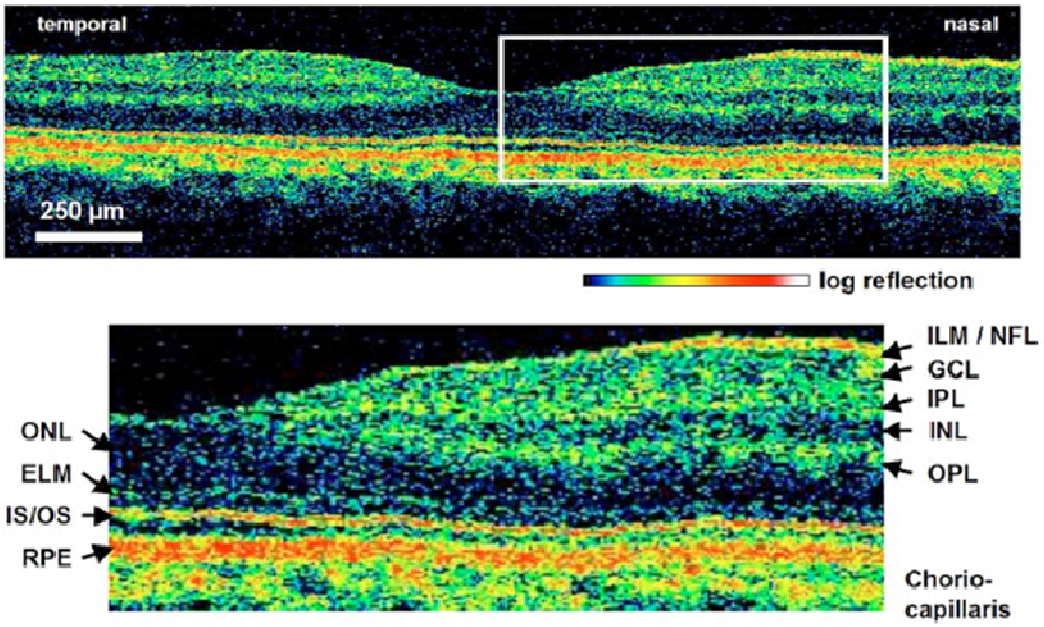

Figure 2.8 OCT cross-sectional image of a human retinal structure with a high axial resolution of 3µm. ILM—inner limiting membrane, NFL—nerve fiber layer, GCL—ganglion cell layer, IPL—inner plexiform layer, INL—inner nuclear layer, OPL—outer plexiform layer, ONL—outer nuclear layer, ELM—external limiting membrane, RPE-retinal pigment epithelium. Figure reprinted from: A.M. Zysk, F.T. Nguyen, A.L. Oldenburg, D.L. Marks, S.A. Boppart, "Optical coherence tomography: a review of clinical development from bench to bedside," J. Biomed. Opt. 12, 05143 (2007). Copyright @ 2007 SPIE.

B. Cardiology

The development of functional OCT modalities, rotational catheter-based probes and improvements in acquisition speed extend OCT in the diagnosis of cardiovascular

diseases that cause millions of deaths every year [61, 62]. Compared with intravascular ultrasound imaging (IV-US), the current standard of intracoronary imaging [63], OCT provides sufficient resolution for visualising and performing reliable characterisation of plaque lesions.

The ideal clinical OCT application in the cardiology field is to visualise vulnerable plaques in the coronary or carotid arteries and evaluate their potential for progression or rupture. This evaluation would ideally be performed after these suspicious areas have been localised regionally by another method, such as computed tomography (CT), ultrasound and fluoroscopy.

The first OCT application in the cardiology field is assessment of the integrity of the vasculature in the coronary artery. Then the OCT modalities, spectroscopic OCT and PS-OCT is applied for cellular and molecular analysis [64-82]. OCT has been demonstrated as an in vivo tool for quantification of activated macrophage content and identification of plaque type contained in a lesion [78, 81]. OCT has also been successfully used in the characterisation and visualisation of cardiac disease including percutaneous coronary intervention and stent implantations [64, 67-69, 73, 75, 79, 80].

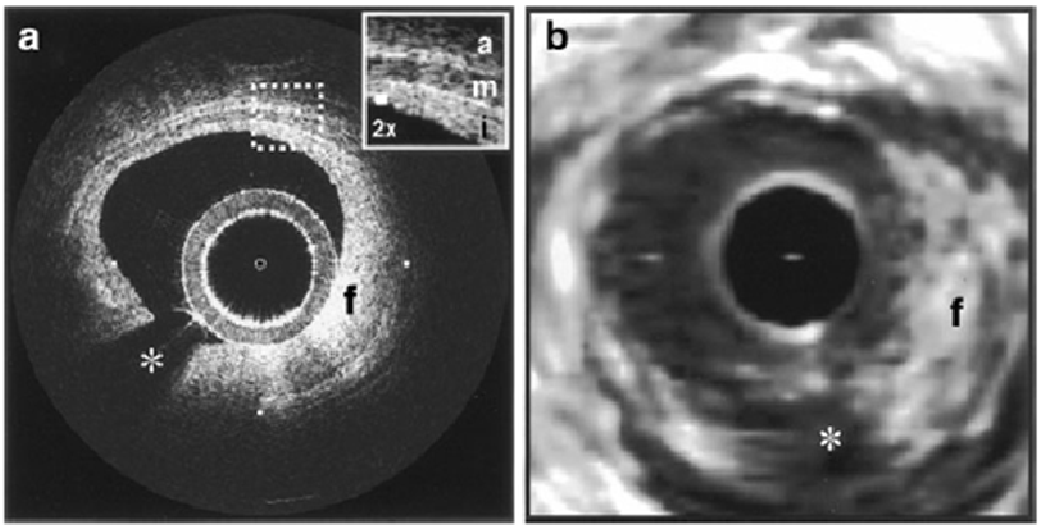

Figure 2.9 (a) Intravascular OCT image. (b) 30MHz IVUS image at the same location. With the high axial resolution, OCT could show the structural detail of vessel walls. i Intima with intimal hyperplasia, m media, a adventitia, f fibrous plaque. Reprinted from: I.K. Jang, B.E. Bouma, D.H. Kang, S.J. Park, S.W. Park, K.B. Seung, K.B. Choi, M. Shishkov, K. Schlendorf, E. Pomerantsev, S.L. Houser, H.T. Aretz. G.J. Tearney, "visualization of coronary atherosclerotic plaques in patients using optical coherence tomography: comparison with intravascular ultrasound." J. Am. Coll. Cardiol. 39: 604-609 (2002). Copyright @ 2002 Elsevier.

C. Dermatology

OCT has been investigated for dermatology in the early stages of its development since the skin is the most easily accessible part of the human body. It is capable of examining skin abnormalities that are difficult to assess by visual inspection. OCT has been studied in psoriasis [83], eczema [84] and non-melanoma skin cancer (NMSC) [85], including keratinocyte carcinomas and other uncommon skin cancers.

OCT could image the structure of the upper layer of human skin, as shown in Fig. 2.11 (a). The boundary between the stratum corneum and the living part of the epidermis is normally clearly visible. Also, an OCT image can differentiate the epidermis from the dermis [86, 87]. However, OCT cannot resolve single cell, the disease diagnosis must rely on a change in skin morphology [86, 88]. The main limitation of OCT for dermatology is its penetration depth, hence evaluation of OCT technology is continuing as it develops further.

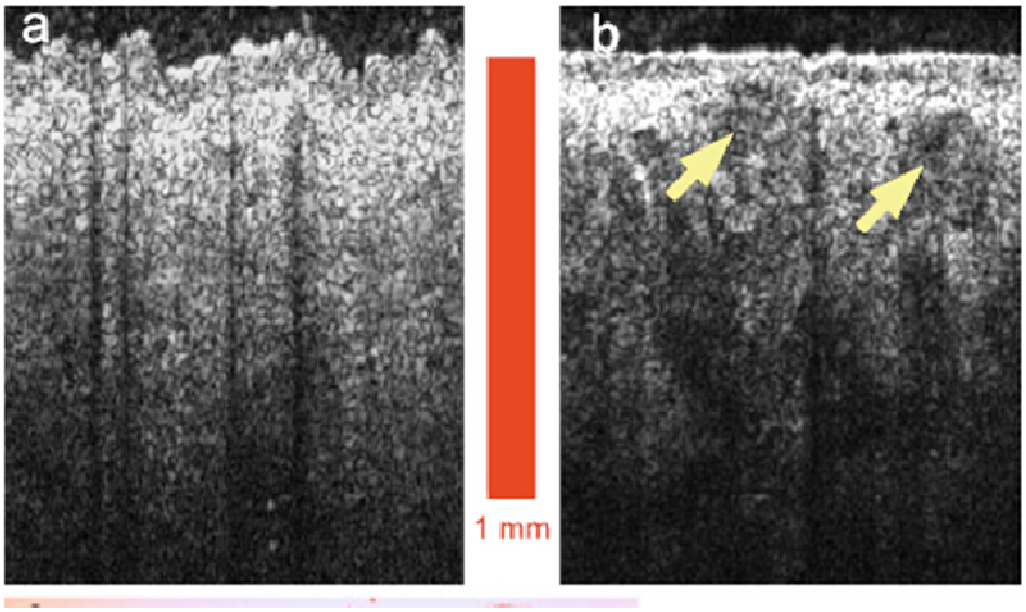

Figure 2.10 OCT images of normal skin (a) and basal cell carcinoma (b) show a clear structural difference. The basaloid carcinoma cell islands, the main features in the corresponding histological image. Figure reprinted from: S. Marschall, B. Sander, M. Mogensen, T.M. Jorgensen, P.E. Andersen, "Optical coherence tomography – current technology and application in clinical and biomedical research," Anal. Bioanal. Chem. 400: 2699-2720 (2011). Copyright @ 2011 Springer-Verlag.

2.5.2 Non-biomedical applications

A. Fibre structure

In the early 1980s, the wavelength tuning interferometric technique was used to determine precisely the outer diameter of optical fibre [89]. Similarity, the diameter of dielectric spheres was determined using the same technique [90]. In 2003, the spectral domain approach replaced the wavelength tuning method to measure the fibre diameter [91]. All three studies measured the interferogram between the front and back surfaces of the fibre or dielectric spheres without using a reference mirror. The subsequent investigation for determination of both fibre diameter and coating thickness were performed on a dual path interferometer setup by introducing the reference mirror [92]. In 2005, the core diameter of fibres with a single hole and three holes were determined [93]. Finally, the future goal of the SD-OCT in fibre

manufacturing is to evaluate the microstructure in real-time during the fibre-draw process.

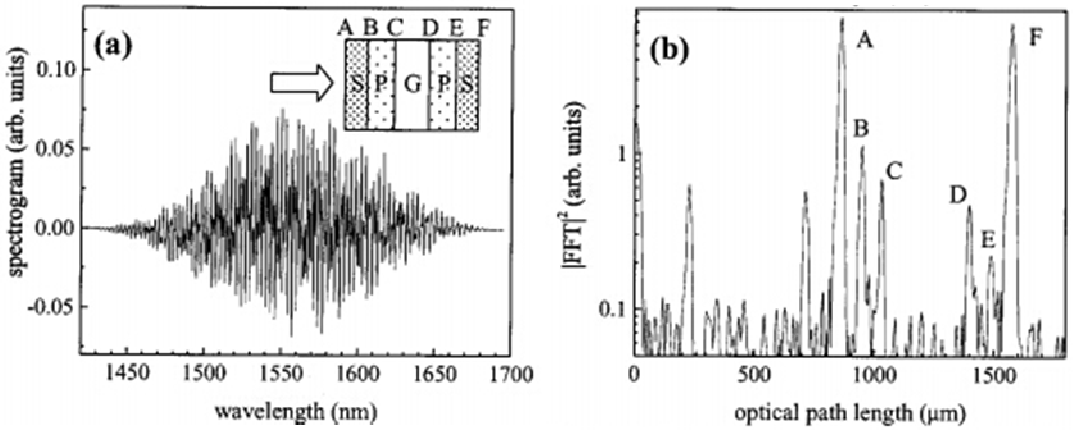

Figure 2.11(a) Spectral interferogram of a standard dual-coated communication fibre multiplied by the Hanning window and (b) Its Fourier Transformed depth profile. The inset of plot (a) shows various layers and interfaces in the fibre cross sectional map. S, P, and G refer to secondary coating, primary coating, and glass, respectively. Figure reprinted from: J. Jasapara, and S. Wielandy, "Characterisation of coated optical fibres by Fourier-domain optical coherence tomography," Opt. Lett. 30: 1018-1020 (2005). Copyright @ 2005 Optical Society of America.

B. Pharmaceutical industry

The potential of SD-OCT as a reliable and practical tool for the analysis of pharmaceutical tablet coatings was first demonstrated in 2010 [94]. Then, SD-OCT was used to analyse the thickness of tablet coating in the range of 10-70 εm [95] and it was considered a complementary tool to TPI for non-destructive evaluation of tablet coatings [96]. However, all the above mentioned studies were performed off-line. Recently, an on-line SD-OCT sensor was presented as a novel tool for monitoring the pharmaceutical film-coating process [97, 98]. Furthermore, the FF-OCT was used for evaluation of coating thickness of small-sized pellet with diameter less than 1 mm [99].

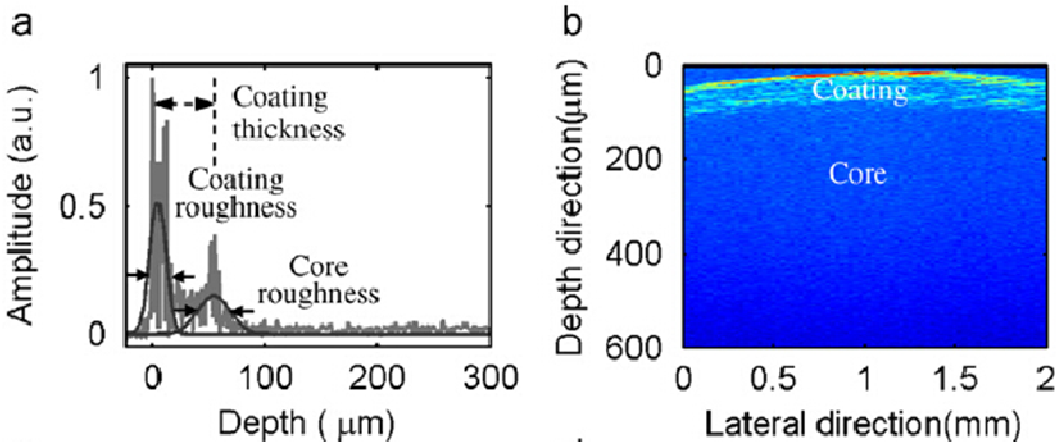

Figure 2.12 (a) Depth profile of a polymer tablet coating (b) cross-sectional image of the same tablet coating. Figure reprinted from: S. Zhong, Y.C. Shen, L. Ho, R.K. May, J.A. Zeitler, M. Evans, P.F. Taday, M. Pepper, T. Rades, K.C. Gordon, R. Muller, P. Kleinebudde, "Non-destructive quantification of pharmaceutical tablet coatings using terahertz pulsed imaging and optical coherence tomography," Opt. Laser Eng. 49: 361-365 (2011). Copyright @ 2010 Elsevier.

References:

1. A.F. Fercher, E. Roth, ñOphthalmic laser interferometry,ò Proc SPIE **658**: 48ï 51 (1986).
2. A.F. Fercher, K. Mengedoht, W. Werner, ñEye-length measurement by interferometry with partially coherent light,ò Opt. Lett. **13**: 186ï 188 (1988).
3. A.F. Fercher, ñOphthalmic Interferometry,ò In: von Bally G, Khanna S, editors. Optics in Medicine, Biology and Environmental Research. Selected Contributions to the First International Conference on Optics Within Life Sciences (OWLS I), Garmisch-Partenkirchen, Germany, 12ï 16 August 1990 (ICO-15 SAT). Amsterdam, London, New York, Tokyo: Elsevier; 1993. pp. 221ï 228.
4. D. Huang, E. Swanson, C.P. Lin, J.S. Schuman, W.G. Stinson, W. Chang, M.R. Hee, T. Flotte, K. Gregory, C.A. Puliafito, J.G. Fujimoto, ñOptical coherence tomography,ò Science **254**: 1178ï 1181 (1991).
5. A.F. Fercher, C.K. Hitzenberger, W. Drexler, G. Kamp, H. Sattmann, ñIn vivo optical coherence tomography,ò Am. J. Ophthal. **116**: 113ï 114 (1993).
6. E.A. Swanson, J.A. Izatt, M.R. Hee, D. Huang, C.P. Lin, J.S. Schuman, C.A. Puliafito, J.G. Fujimoto, ñIn vivo retinal imaging by optical coherence tomography,ò Opt. Lett. **18**: 1864ï 1866 (1993).
7. A.F. Fercher, C.K. Hitzenberger, G. Kamp, S.Y. El-Zaiat, ñMeasurement of intraocular distances by backscattering spectral interferometry,ò Opt. Commun. **117**: 43ï 48 (1995).
8. G. Häusler and M.W. Lindner, ñCoherence radar and spectral radar ð New tools for dermatological diagnosis,ò J. Biomed. Opt. **3**: 21-31 (1998).
9. W.H. Steel, ñInterferometry,ò Cambridge: Cambridge University Press; (1983).
10. L.M. Smith, C. Dobson, ñAbsolute displacement measurements using modulation of the spectrum of white light in a Michelson interferometer,ò Appl. Opt. **28**: 3339ï 3342 (1989).
11. A.F. Fercher, C. Hitzenberger, M. Juchem, ñMeasurement of intraocular optical distances using partially coherent laser light,ò J. Mod. Opt. **38**: 1327ï 1333 (1991).
12. J. deBoer, B. Cense, B.H. Park, M.C. Pierce, G.J. Tearney, B.E. Bouma, ñImproved signal-to-noise ratio in spectral-domain compared with time-domain optical coherence tomography,ò Opt. Lett. **28**: 2067ï 2069 (2003).

13. M.A. Choma, M.V. Sarunic, C. Yang, J.A. Izatt, ñSensitivity advantage of swept source and Fourier domain optical coherence tomography,ò Opt. Express **11**: 2183ï 2189 (2003).
14. M. Wojtkowski, A. Kowalczyk, R. Leitgeb, A.F. Fercher, ñFull range complex spectral optical coherence tomography technique in eye imaging,ò Opt. Lett. **27**: 1415ï 1417 (2002).
15. A.F. Fercher, W. Drexler, C.K. Hitzenberger, T. Lasser, ñOptical coherence tomography ï principle and application,ò Rep. Prog. Phys. **66**: 239-303 (2003).
16. M. Wojtkowski, ñHigh speed optical coherence tomography: basics and applications,ò Appl. Opt. **49**: 30-61 (2010).
17. A.F. Fercher, ñOptical coherence tomography ï development, principles, applications,ò Z. Med. Phys. **20**: 251-276 (2010).
18. K.G. Larkin, ñEfficient nonlinear algorithm for envelop detection in white light interferometry,ò J. Opt. Soc Am. A **13**: 832-843 (1996).
19. E. Beaurepaire, A.C. Boccara, M. Lebec, L. Blanchot, H. Saint-Jalmes, ñFull field coherence microscopy,ò Opt. Lett. **23**: 244-246 (1998).
20. R.A. Leitgeb, C.K. Hitzenberger, A.F. Fercher, T. Bajraszewski, ñPhase-shifting algorithm to achieve high-speed by frequency-domain optical coherence tomography,ò Opt. Lett. **28**: 2201-2203 (2003).
21. Z.H. Ma, R.K. Wang, F. Zhang, J.Q. Yao, ñSpectral optical coherence tomography using two-phase shifting method,ò Chin. Phys. Lett. **22**: 1909-1912 (2005).
22. Y. Yasuno, S. Makita, T. Endo, G. Aoki, H. Sumimura, M. Itoh, T. Yatagai, ñOne-shot-phase-shifting Fourier domain optical coherence tomography by reference wavefront tilting,ò Opt. Express **12**: 6184-6191 (2004).
23. Z.P. Chen, J. Zhang, J.S. Nelson, ñRemoval of a mirror image and enhancement of the signal-to-noise ratio in Fourier-domain optical coherence tomography using an electro-optic phase modulator,ò Opt. Lett. **30**: 147-149 (2005).
24. M. Wojtkowski, A. Kowalczyk, R. Leitgeb, A.F. Fercher, ñFull range complex spectral optical coherence tomography technique in eye imaging,ò Opt. Lett. **27**: 1415- 1417 (2002).

25. E. Gotzinger, A. Kowalczyk, R. Leitgeb R, C.K. Hitzenberger, ñHigh speed full range complex spectral domain optical coherence tomography,ò Opt. Express **13**: 583-594 (2005).
26. M.V. Sarunic, B.E. Applegate, J.A. Izatt, ñReal-time quadrature projection complex conjugate resolved Fourier domain optical coherence tomography,ò Opt. Lett. **14**: 1487-1496 (2006).
27. A.H. Bachmann, R. Leitgeb, and T. Lasser. ñHeterodyne Fourier domain optical coherence tomography for full range probing with high axial resolution,ò Opt. Express **14**: 1487-1496 (2006).
28. Y. Yasuno, S. Makita, T. Endo, G. Aoki, M. Itoh, T. Yatagai, ñSimultaneous B-M-mode scanning method for real-time full-range Fourier domain optical coherence tomography,ò Appl. Opt. **45**: 1861-1865 (2006).
29. B. Baumann, M. Pircher, E. Gotzinger, C.K. Hitzenberger, ñFull range complex spectral domain optical coherence tomography without additional phase shifter,ò Opt. Express **15**: 13375-13387 (2007).
30. B. Hofer, B. Povazay, B. Hermann, A. Unterhuber, G. Matz, W. Drexler, ñDispersion encoded full range frequency domain optical coherence tomography,ò Opt. Express **17**: 7-24 (2009).
31. S. Witte, M. Baclayon, E.J.G. Peterman, R.F.G. Toonen, H.D. Mansvelder, M.L. Groot, ñSingle-shot two-dimensional full-range optical coherence tomography achieved by dispersion control,ò Opt. Express **17**: 11335-11349 (2009).
32. J.M. Schmitt, S.L. Lee, K.M. Yung, ñAn optical coherence microscope with enhanced resolving power in thick tissue,ò Opt. Comm. **142**: 203-207 (1997).
33. T.H. Ko, D.C. Adler, J.G. Fujimoto, D. Mamedov, V. Prokhorov, V. Shidlovski, S. Yakubovich, ñUltrahigh resolution optical coherence tomography using a broadband superluminescent diode light source,ò Opt. Express **12**: 2112-2119 (2004).
34. A. Unterhuber, B. Povazay, B. Hermann, H. Sattmann, W. Drexler, V. Yakovlev, G. Tempea, C. Schubert, E.M. Anger, P.K. Ahnelt, M. Stur, J.E. Morgan, A. Cowey, G. Jung, T. Le, A. Stingl, ñCompact, low-cost Ti: Al_2O_3 laser for in vivo ultrahigh-resolution optical coherence tomography,ò Opt. Lett. **28**: 905-907 (2003).

35. A. Unterhuber, B. Povazay, K. Bizheva, B. Hermann, H. Sattmann, A. Stingl, T. Le, M. Seefeld, R. Menzel, M. Preusser, H. Budka, C. Schubert, H. Reitsamer, P.K. Ahnelt, J.E. Morgan, A. Cowey, W. Drexler, ñAdvances in broad bandwidth light sources for ultrahigh resolution optical coherence tomography,ò Phys. Med. Biol. **49**: 1235-1246 (2004).
36. B. Potsaid, I. Gorczynska, V.J. Srinivasan, Y. Chen, J. Jiang, A. Cable, J.G. Fujimoto, ñUltrahigh speed Spectral/Fourier domain OCT ophthalmic imaging at 70,000 to 312,500 axial scans per second,ò Opt. Express **16**: 15149ï 69 (2008).
37. B. Povazay, B. Hofer, C. Torti, B. Hermann, A.R. Tumlinson, M. Esmaeelpour, C.A. Egan, A.C. Bird, W. Drexler, ñImpact of enhanced resolution, speed and penetration on three-dimensional retinal optical coherence tomography,ò Opt. Express **17**: 4134ï 50 (2009).
38. I. Grulkowski, M. Gora, M. Szkulmowski, I. Gorczynska, D. Szlag, S. Marcos, A. Kowalczyk, M. Wojtkowski, ñAnterior segment imaging with Spectral OCT system using a high-speed CMOS camera,ò Opt. Express **17**: 4842ï 4858 (2009).
39. E. Beaurepaire, A.C. Boccara, M. Lebec, L. Blanchot, H. Sanit-Jalmes, ñFull-field optical coherence microscopy,ò Opt. Lett. **23**: 244-246 (1998).
40. A. Dubois, A.C. Boccara, ñFull-Field optical coherence tomography,ò In: Drexler W, Fujimoto JG, editors. Optical Coherence Tomography. Berlin, Heidelberg: Springer; 2008. pp. 565ï 91.
41. A. Dubois, G. Moneron, K. Grieve, A.C. Boccara. ñThree-dimensional celluar-level imaging using full-field optical coherence tomography,ò Phys. Med. Bio. **49**: 1227-1234 (2004).
42. M.R. Hee, D. Huang, E.A. Swanson, J.G. Fujimoto, ñPolarization-sensitive low-coherence reflectometer for birefringence characterization and ranging,ò J. Opt. Soc. Am. **9**: 903-908 (1992).
43. J.F. deBoer, T.E. Milner, M.J.C. vanGemert, J.S. Nelson, ñTwo-dimensional birefringence imaging in biological tissue by polarization-sensitive optical coherence tomography,ò Opt. Lett. **22**: 934-936 (1997).
44. J.F. de Boer, S.M. Srinivas, J.S. Nelson, T.E. Milner, M.G. Ducros, 2002 Handbook of Optical Coherence Tomography Ed. B E Bouma and G J Tearney (New York: Dekker) pp 237ï 74

45. E. Götzinger, M. Pircher, W. Geitzenauer, C. Ahlers, B. Baumann, S. Michels, U. Schmidt-Erfurth, C.K. Hitzenberger, ñRetinal pigment epithelium segmentation by polarization sensitive optical coherence tomography,ò Opt Express **16**: 16410ï 16422 (2008).
46. M. Zhao, J.A. Izatt, ñSingle-camera sequential-scan-based polarization sensitive SD-OCT for retinal imaging,ò Opt. Lett. **34**:205ï 207 (2009).
47. Z.P. Chen, T.E. Milner, D. Dave, J.S. Nelson, ñOptical Doppler tomographic imaging of fluid flow velocity in highly scattering media,ò Opt. Lett. **22**: 64-66 (1997).
48. U. Morgner, W. Drexler, F.X. Kartner, X.D. Li, C. Pitris, E.P. Ippen, J.G. Fujimoto, ñSpectroscopic optical coherence tomography,ò Opt. Lett. **25**: 111-113 (2000).
49. L. Alexander and W. Choate, ñOptical coherence tomography: rewriting the standard of care in diagnosis, management and interventional assessment,ò Rev. Optometry **141**: 1CEï 8CE (2004).
50. R.A. Costa, M. Skaf, L.A.S. Melo, D. Calucci, J.A. Cardillo, J.C. Castro, D. Huang, and M. Wojtkowski, ñRetinal assessment using optical coherence tomography,ò Prog. Retin Eye Res. **25**: 325ï 353 (2006).
51. M. R. Dogra, A. Gupta, and V. Gupta, Atlas of optical coherence tomography of macular diseases, Taylor & Francis, New York, 2004.
52. M. R. Hee, C. A. Puliafito, C. Wong, J. S. Duker, E. Reichel, B. Rutledge, J. S. Schuman, E. A. Swanson, and J. G. Fujimoto, ñQuantitative assessment of macular edema with optical coherence tomography,ò Arch. Ophthalmol. **113**: 1019ï 1029 (1995).
53. J. S. Schuman, C. A. Puliafito, and J. G. Fujimoto, Optical coherence tomography of ocular diseases, Slack, Inc., Thorofare, NJ ,2004.
54. A.M. Zysk, F.T. Nguyen, A.L. Oldenburg, D.L. Marks, S.A. Boppart, ñOptical coherence tomography: a review of clinical development from bench to bedside,ò J. Bio. Opt. 12: 051403 (2011).
55. E. Z. Blumenthal, J. M. Williams, R. N. Weinreb, C. A. Girkin, C. C. Berry, and L. M. Zangwill, ñReproducibility of nerve fibre layer thickness measurements by use of optical coherence tomography,ò Ophthalmology **107**: 2278ï 2282 (2000).

56. D. L. Budenz, R. T. Chang, X. Huang, R. W. Knighton, and J. M. Tielsch, ñReproducibility of retinal nerve fibre thickness measurements using the Stratus OCT in normal and glaucomatous eyes,ò Invest. Ophthalmol. Visual Sci. **46:** 2440ï 2443 (2005).
57. P. Carpineto, M. Ciancaglini, E. Zuppardi, G. Falconio, E. Doronzo, and L. Mastropasqua, ñReliability of nerve fibre layer thickness measurements using optical coherence tomography in normal and glaucomatous eyes,ò Ophthalmology **110** : 190ï 195 (2003).
58. L. A. Paunescu, J. S. Schuman, L. L. Price, P. C. Stark, S. Beaton, H. Ishikawa, G. Wollstein, and J. G. Fujimoto, ñReproducibility of nerve fibre thickness, macular thickness, and optic nerve head measurements using Stratus OCT,ò Invest. Ophthalmol. Visual Sci. **45**: 1716ï 1724 (2004).
59. G. Wollstein, J. S. Schuman, L. L. Price, A. Aydin, P. C. Stark, E. Hertzmark, E. Lai, H. Ishikawa, C. Mattox, J. G. Fujimoto, and L. A. Paunescu, ñOptical coherence tomography longitudinal evaluation of retinal nerve fibre layer thickness in glaucoma,ò Arch. Ophthalmol. **123**: 464ï 470 (2005).
60. C. A. Sánchez-Galeana, C. Bowd, L. M. Zangwill, P. A. Sample, and R. N. Weinreb, ñShort-wavelength automated perimetry results are correlated with optical coherence tomography retinal nerve fibre layer thickness measurements in glaucomatous eyes,ò Ophthalmology **111**: 1866ï 1872 (2004).
61. S. Marschall, B. Sander, M. Mogensen, T.M. Jorgensen, P.E. Andersen, "Optical coherence tomography - current technology and applications in clinical and biomedical research," Anal. Bioanal. Chem. **400**: 2699-2720 (2011).
62. World Health Organization (2010) Fact sheet no. 317: cardiovascular diseases. WHO, Geneva. http://www.who.int/mediacentre/factsheets/fs317/en/, accessed 19 Nov 2010
63. I. K. Jang, B. E. Bouma, D. H. Kang, S. J. Park, S. W. Park, K. B. Seung, K. B. Choi, M. Shishkov, K. Schlendorf, E. Pomerantsev, S. L. Houser, H. T. Aretz, and G. J. Tearney, ñVisualization of coronary atherosclerotic plaques in patients using optical coherence tomography: comparison with intravascular ultrasound,ò J. Am. Coll. Cardiol. **39**: 604ï 609 (2002).
64. B. E. Bouma and G. J. Tearney, ñClinical imaging with optical coherence tomography,ò Acad. Radiol. **9**: 942ï 953 (2002).

65. B. E. Bouma, G. J. Tearney, H. Yabushita, M. Shishkov, C. R. Kauffman, D. DeJoseph Gauthier, B. D. MacNeill, S. L. Houser, H. T. Aretz, E. F. Halpern, and I. K. Jang, ñEvaluation of intracoronary stenting by intravascular optical coherence tomography,ò Heart **89**: 317ï 320 (2003).
66. M. E. Brezinski, G. J. Tearney, B. E. Bouma, J. A. Izatt, M. R. Hee, E. A. Swanson, J. F. Southern, and J. G. Fujimoto, ñOptical coherence tomography for optical biopsy: Properties and demonstration of vascular pathology,ò Circulation **93**: 1206ï 1213 (1996).
67. M. E. Brezinski, G. J. Tearney, B. E. Bouma, S. A. Boppart, M. R. Hee, E. A. Swanson, J. F. Southern, and J. G. Fujimoto, ñImaging of coronary artery microstructure _in vitro_ with optical coherence tomography,ò Am. J. Cardiol. **77**: 92ï 93 (1996).
68. M. E. Brezinski, G. J. Tearney, N. J. Weissman, S. A. Boppart, B. E. Bouma, M. R. Hee, A. E. Weyman, E. A. Swanson, J. F. Southern, and J. G. Fujimoto, ñAssessing atherosclerotic plaque morphology: comparison of optical coherence tomography and high frequency intravascular ultrasound,ò Heart **77**: 397ï 403 (1997).
69. A. H. Chau, R. C. Chan, M. Shishkov, B. MacNeill, N. Iftimia, G. J. Tearney, R. D. Kamm, B. E. Bouma, and M. R. Kaazempur-Mofrad, ñMechanical analysis of atherosclerotic plaques based on optical coherence tomography,ò Ann. Biomed. Eng. **32**: 1494ï 1503 (2004).
70. J. G. Fujimoto, S. A. Boppart, G. J. Tearney, B. E. Bouma, C. Pitris, and M. E. Brezinski, ñHigh resolution in vivo intra-arterial imaging with optical coherence tomography,ò Heart **82**: 128ï 133 (1999).
71. M. Gupta, A. M. Rollins, J. A. Izatt, and I. R. Efimov, ñImaging of the atrioventricular node using optical coherence tomography,ò J. Cardiovasc. Electrophysiol. **13**: 95 (2002).
72. I. K. Jang, G. Tearney, and B. Bouma, ñVisualization of tissue prolapse between coronary stent struts by optical coherence tomography: comparison with intravascular ultrasound,ò Circulation **104**: 2754 (2001).
73. I. K. Jang, B. E. Bouma, D. H. Kang, S. J. Park, S. W. Park, K. B. Seung, K. B. Choi, M. Shishkov, K. Schlendorf, E. Pomerantsev, S. L. Houser, H. T. Aretz, and G. J. Tearney, ñVisualization of coronary atherosclerotic plaques in patients using

optical coherence tomography: comparison with intravascular ultrasound,ò J. Am. Coll. Cardiol. **39**: 604ï 609 (2002).

74. I. K. Jang, G. J. Tearney, B. MacNeill, M. Takano, F. Moselewski, N. Iftima, M. Shishkov, S. Houser, H. T. Aretz, E. F. Halpern, and B. E. Bouma, ñIn vivo characterization of coronary atherosclerotic plaque by use of optical coherence tomography,ò Circulation **111:** 1551ï 1555 (2005).
75. B. D. MacNeill, I. K. Jang, B. E. Bouma, N. Iftimia, M. Takano, H. Yabushita, M. Shishkov, C. R. Kauffman, S. L. Houser, H. T. Aretz, D. DeJoseph, E. F. Halpern, and G. J. Tearney, ñFocal and multi-focal plaque macrophage distributions in patients with acute and stable presentations of coronary artery disease,ò J. Am. Coll. Cardiol. **44**: 972ï 979 (2004).
76. G. J. Tearney, M. E. Brezinski, S. A. Boppart, B. E. Bouma, N. Weissman, J. F. Southern, E. A. Swanson, and J. G. Fujimoto, ñCatheter-based optical imaging of a human coronary artery,ò Circulation **94**: 3013 (1996).
77. G. J. Tearney, M. E. Brezinski, B. E. Bouma, S. A. Boppart, C. Pitris, J. F. Southern, and J. G. Fujimoto, ñIn vivo endoscopic optical biopsy with optical coherence tomography,ò Science **276**: 2037ï 2039 (1997).
78. G. J. Tearney and B. E. Bouma, Method and apparatus for determination of atherosclerotic plaque type by measurement of tissue optical properties, U.S. Patent Application 20030028100 (2003).
79. G. J. Tearney, H. Yabushita, S. L. Houser, H. T. Aretz, I. K. Jang, K. H. Schlendorf, C. R. Kauffman, M. Shishkov, E. F. Halpern, and B. E. Bouma, ñQuantification of macrophage content in atherosclerotic plaques by optical coherence tomography,ò Circulation **107**: 113ï 119 (2003).
80. H. Yabushita, B. E. Bouma, S. L. Houser, H. T. Aretz, I. K. Jang, K. H. Schlendorf, C. R. Kauffman, M. Shishkov, D. H. Kang, E. F. Halpern, and G. J. Tearney, ñCharacterization of human atherosclerosis by optical coherence tomography,ò Circulation **106**: 1640ï 1645 (2002).
81. T. M. Yelbuz, M. A. Choma, L. Thrane, M. L. Kirby, and J. A. Izatt, ñOptical coherence tomography: a new high-resolution imaging technology to study cardiac development in chick embryos,ò Circulation **106**: 2771ï 2774 (2002).

82. W. Luo, D. L. Marks, T. S. Ralston, and S. A. Boppart, ñThree dimensional optical coherence tomography of the embryonic murine cardiovascular system,ò J. Biomed. Opt. **11**: 021014 (2006).
83. R. Steiner, K. Kunzi-Rapp, K. Scharffetter-Kochanek, ñOptical coherence tomography: clinical applications in dermatology,ò Med. Laser Appl. **18**: 249ï 259 (2003).
84. M. Mogensen, G.B.E. Jemec, L. Thrane, T.M. Jørgensen, P.E. Andersen, ñOCT imaging of skin cancer and other dermatological diseases,ò J. Biophotonics **2**: 442ï 451 (2009).
85. M. Mogensen, B.M. Nürnberg, J.L. Forman, J.B. Thomsen, L. Thrane, G.B.E. Jemec, ñIn vivo thickness measurement of basal cell carcinoma and actinic keratosis with optical coherence tomography and 20-MHz ultrasound,ò Br. J. Dermatol. **160**:1026ï 1033 (2009).
86. M. Mogensen, H.A. Morsy, L. Thrane, G.B.E. Jemec, ñMorphology and epidermal thickness of normal skin imaged by optical coherence tomography,ò Dermatology **217**:14ï 20 (2008).
87. A. Alex, B. Povaġay, B. Hofer, S. Popov, C. Glittenberg, S. Binder, W. Drexler, ñMultispectral in vivo three-dimensional optical coherence tomography of human skin,ò J. Biomed. Opt. **15**: 026025 (2010).
88. J. Welzel, ñOptical coherence tomography in dermatology: a review,ò Skin Res. Technol. **7**:1-9 (2001).
89. A. Ashkin, J.M. Dziedzic, R.H. Stolen, ñOuter diameter measurement of low birefringence of optical fibres by a new resonant backscatter technique,ò Appl. Opt. **20**: 2299-2303 (1981)
90. A. Ashkin, J. M. Dziedzic, ñObservation of optical resonances of dielectric spheres by light-scattering,ò Appl. Opt. **20**: 1803-1814 (1981).
91. J. Jasapara, E. Monberg, F. DiMarcello, J.W. Nicholson, ñAccurate noncontact optical fibre diameter measurement with spectral interferometry,ò Opt. Lett. **28**: 601-603 (2003)
92. J. Jasapara, E. Monberg, F. DiMarcello, J.W. Nicholson, ñCharacterization of coated optical fibres by Fourier-domain optical coherence tomography,ò Opt. Lett. **30**: 1018-1020 (2005).

93. J.C. Jasapara, ñNon-invasive characterization of microstructured optical fibres using Fourier domain optical coherence tomography,ò Opt. Express **13**: 1228-1233 (2005).
94. J.M. Mauritz, R.S. Morrisbv, R.S. Hutton, C.H. Legge, C.F. Kaminski, "Imaging pharmaceutical tablets with optical coherence tomography," J. Phar. Sci. **99**: 385-391 (2010).
95. D.M. Koller, G. Hannesschlager, M. Leitner, J.G. Khinast, "Non-destructive analysis of tablet coatings with optical coherence tomography," Eur. J. Pharm. Sci. **44**:142-148 (2011).
96. S.C. Zhong, Y.C. Shen, L. Ho, R.K. May, J.A. Zeitler, M. Evans, P.F. Taday, M. Pepper, T. Rades, K.C. Gordon, R. Muller, P. Kleinebudde, "Non-destructive quantification of pharmaceutical tablet coatings using terahertz pulsed imaging and optical coherence tomography," Opt. Laser Eng. **49**: 361-365 (2011).
97. D. Markl, G. Hannesschlager, S. Sacher, M. Leitner, J.G. Khinast, ñOptical coherence tomography as a novel tool for in-line monitoring of a pharmaceutical film-coating process,ò Eur. J. Pharm. Sic. **55**: 58-67 (2014).
98. D. Markl, G. Hannesschlager, A Buchsbaum, S. Sacher, J.G. Khinast, M. Leitner, ñIn-line quality control of moving objects by means of spectral-domain OCT,ò Opt. Laser Eng. **59**: 1-10 (2014).
99. C. Li, J.A. Zeitler, Y. Dong, Y.C. Shen, "Non-destructive evaluation of polymer coating structures on pharmaceutical pellets using full-field optical coherence tomography," J. Pharm. Sci. **106**, 161-166 (2013).

Chapter 3 Implementation of free space SD-OCT configurations

3.1 Introduction

Normally, a SD-OCT system utilises a line camera based spectrometer to record the spectral interferogram between reference mirror and sample tissue. In a single exposure, the line camera takes one spectrum containing the axial structural information of a single lateral pixel on the sample. To generate the cross-sectional image, lateral scan is conducted by moving either the probe beam/sample beam or the sample tissue. Although the line camera based SD-OCT system can achieve a scanning rate of 310k A-scans/s [1], the motion artefacts between different lateral pixels can still exist. Therefore, a single-shot SD-OCT [2-6] based on a 2D array camera has been developed. In a single-shot SD-OCT system, multiple spectral interferograms are taken in a single exposure to generate the cross-sectional image. Hence, it is free of motion artefacts and further improves the imaging speed.

In my work, both types of SD-OCT setups were built for different applications. In this chapter, the setup of these SD-OCT systems and their performance are explained in detail.

3.2 Single point SD-OCT

3.2.1 Experiment setup

The schematic diagram of the built SD-OCT setup is shown in Fig. 3.1. The light source used in the single point SD-OCT system was a low coherence SLD (EXALOS) centred at 844 nm with a spectral FWHM of 132 nm. The power of the SLD was 5 mW. The collimated light beam was split into two arms by a 50:50 beam splitter. In the sample arm, the sample beam was focused onto the sample objectôs surface by an

OCT scanning lens (Thorlabs, f=37.5). In the reference arm, the collimated light passes through a dispersion compensator and is then reflected by the reference mirror. Alternatively, to avoid dispersion due to the imbalanced instruments between reference and sample arm, two identical lenses could be used to focus the reference beam and sample beam onto the reference mirror and sample tissue respectively. Then, the back reflected/scattered light from the reference mirror and sample tissue recombined at the exit of the beam splitter and then were delivered to the spectrometer using a multimode fibre.

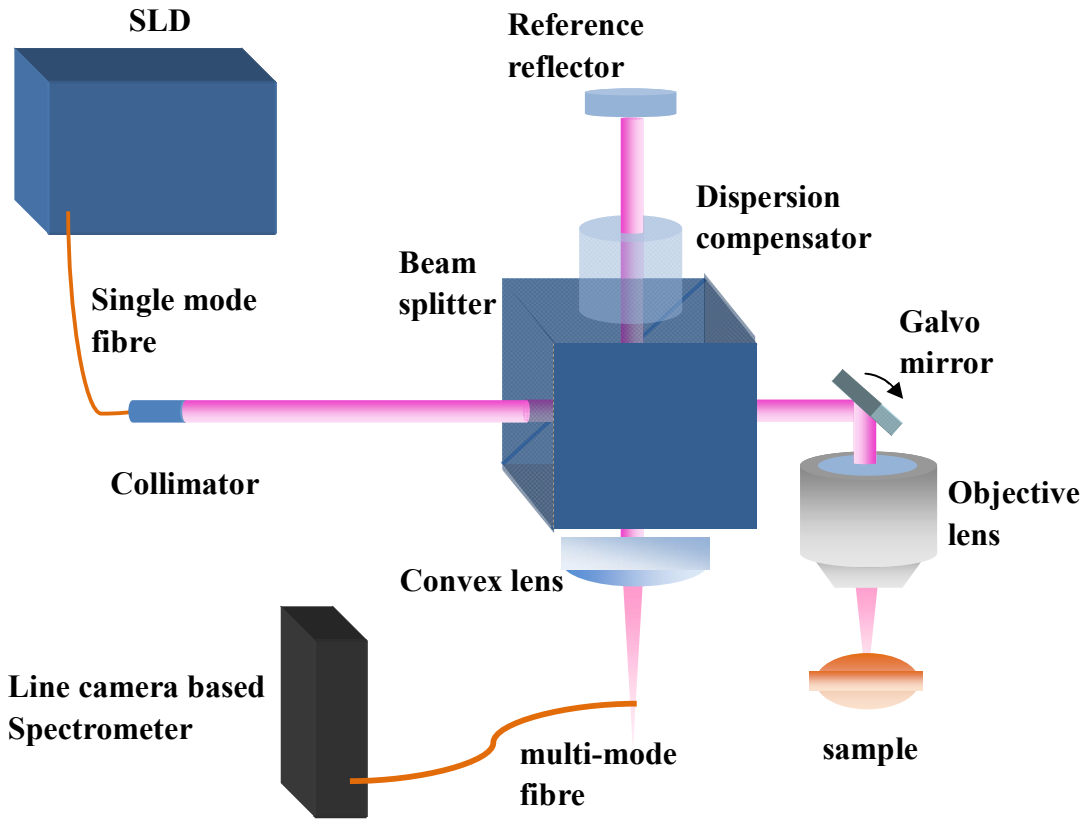

Figure 3.1 Schematic diagram of a conventional SD-OCT system. The lateral scan is performed by a galvo mirror.

3.2.2 Performance

A. Axial resolution

As mentioned in chapter 2, the axial resolution is theoretically determined by the spectral FWHM and centre wavelength of the light source. In this case, the spectral FWHM and centre wavelength of the light source is 132 nm and 844 nm respectively.

Hence, the axial resolution is 2.3 μm by means of Eq. (2.13). In practice, the axial resolution is determined by the FWHM of the main peak in the depth profile. Fig. 3.2 (a) shows one of the depth profiles on a 150 μm glass slide that was obtained using two identical lens pairs. Fig. 3.2 (b) shows one of the depth profile obtained using the objective lens and compensator. If the refractive index of the glass slide is assumed to be as 1.5, the measured axial resolution is about 2.5 μm and 5.5 μm respectively.

The dispersion results in a wavelength dependent light velocity in a medium, hence the imbalance optics between the reference and sample arms leads to a wavelength dependent OPD difference. By considering the imbalance dispersion, the spectral interferogram can be expressed as [6]:

$$I(k) = S_R + S_S + 2\sqrt{S_R S_S}\cos(\Delta\varphi + \varphi(k)) \tag{3.1}$$

The imbalance frequency dependent phase $\varphi(k)$ broaden the Fourier transformed peak. Therefore, the imbalance optics between the reference and sample arm make the axial resolution worse.

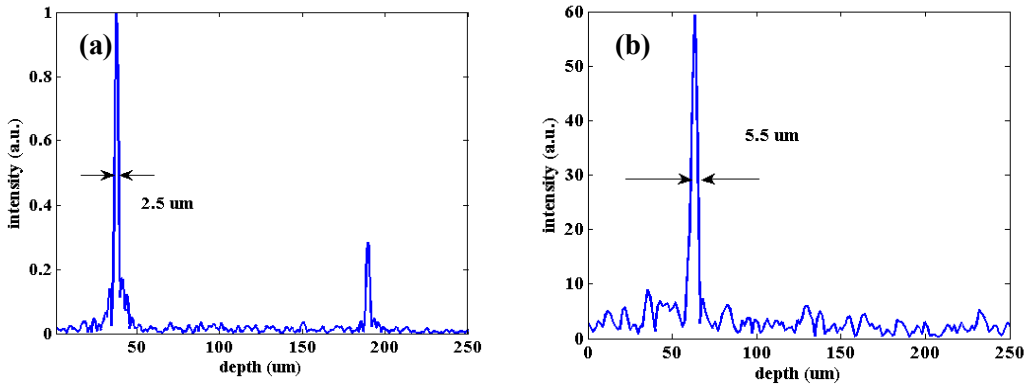

Figure 3.2 Surface peak of glass slide in depth profiles (a) obtianed by two identical lens pairs, and (b) obtained by an objective lens and a compensator. The axial resolution measured by the FWHM of the main peak are (a) 2.5 μm, (b) 5.5 μm.

B. imaging depth

Recalling the Eq. (2.16) in chapter 2, the maximum imaging depth of a SD-OCT system is determined by the spectral resolution of the used spectrometer and the centre wavelength of the light source. In the pharmaceutical application discussed in

chapter 4, two fibre spectrometers were used in the conventional SD-OCT system. The first spectrometer has 3648 pixels and its measurement range is from 550 nm to 1028 nm (Mightex). The spectral resolution provided by the manufacturer is 0.5 nm, hence its imaging depth is 361 um in air according to Eq. (2.16). The second spectrometer has 2048 pixels and its measurement range is from 780 nm to 950 nm (Ocean Optics). Its spectral resolution is about 0.12 nm; therefore, the maximum imaging depth achieved using this spectrometer is about 1.8 mm in air.

C. Lateral resolution

The highest lateral resolution of the system is theoretically defined by the FWHM of the beam waist. If the sample is not on the focus plane, the lateral resolution should be the FWHM of the diameter of the light spot on the sample. In order to characterise the lateral resolution, the cut edge of a transparent tape was measured. The tape was moved laterally by a translation stage with a step size of 2 ε m. Fig 3.3 shows the peak intensity of the tape surface plane. The lateral resolution measured by the width of the raising edge was about 16 ε m.

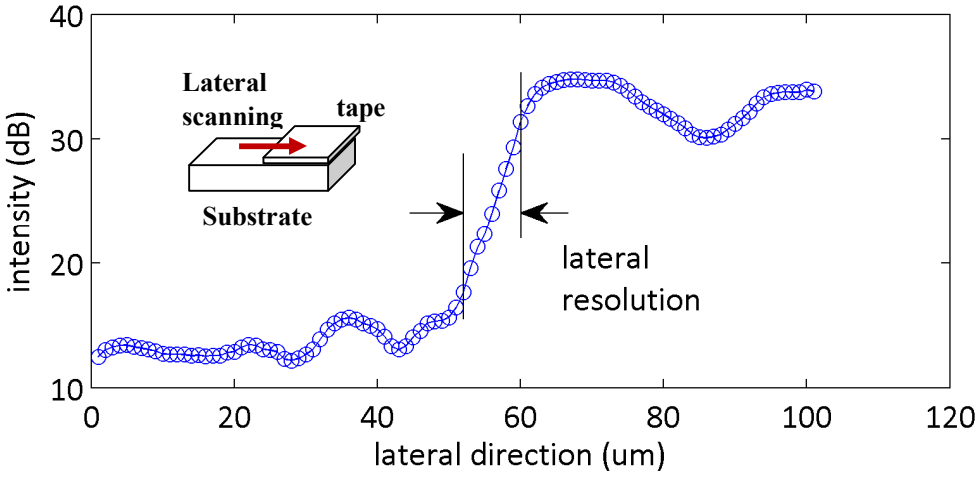

Figure 3.3 Depth profile intensity of the tape surface plane. The lateral resolution defined by the width of the raising edge is about 16 µm. The inset shows a schematic diagram of the measured tape.

D. Lateral axis correction

The lateral axis can be obtained easily if the lateral scan is performed by a translation stage because the step size is constant. However, if the lateral scan is performed by rotating the glove mirror, the lateral axis requires additional calibration. As the user manual specifies, a galvo mirror (Thorlabs) rotates 1^{o} if the driven voltage is 1 volt. The rotation range of the galvo mirror is from -10^{o} to 10^{o}. Assuming the probe beam locates at the centre of the objective lens when the driven voltage is 0 volt, then the lateral position of the probe beam on the sample that is corresponds with the scanning angle could be expressed as:

$$L = d \cdot \tan(\theta) \tag{3.2}$$

where d is the working distance between the galvo mirror and the objective lens, and ɗ is the rotation angle. Fig. 3.4 demonstrates the lateral scanning performance.

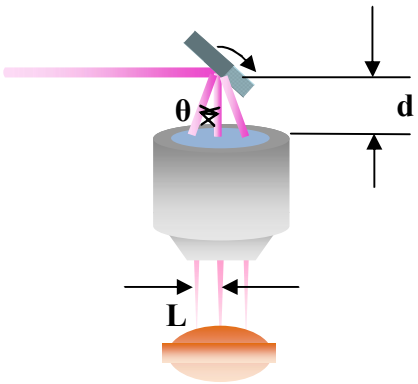

Figure 3.4 Lateral scanning performed by a galvo mirror.

3.2.3 Testing cross-sectional images

A. Human finger

The sample beam was focused on a fingertip by the objective lens and swept by the galvo mirror. Fig. 3.5 shows the cross-sectional image of the fingertip, consisting of 300 A-scans, with an image size of 0.5×3 mm^2. As well the epidermis and dermis, one of the sweat glands can be seen in the cross-sectional image.

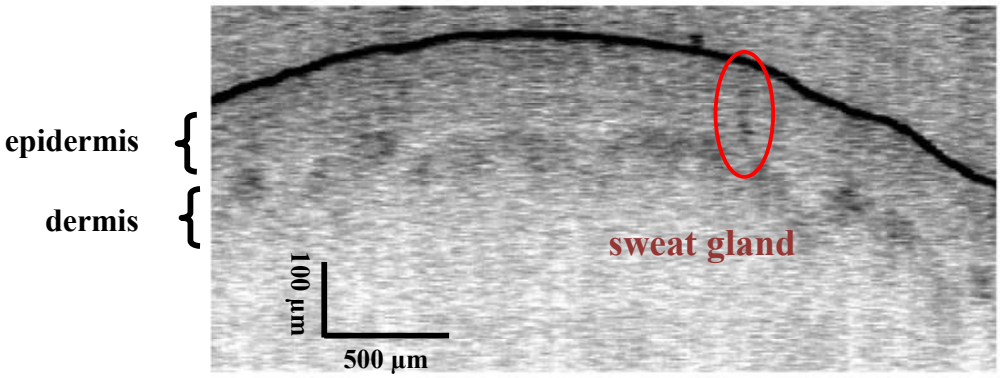

Figure 3.5 Cross-sectional image of a fingertip measured by the conventional SD-OCT system. The red ellipse indicates the sweat gland.

B. Human cornea

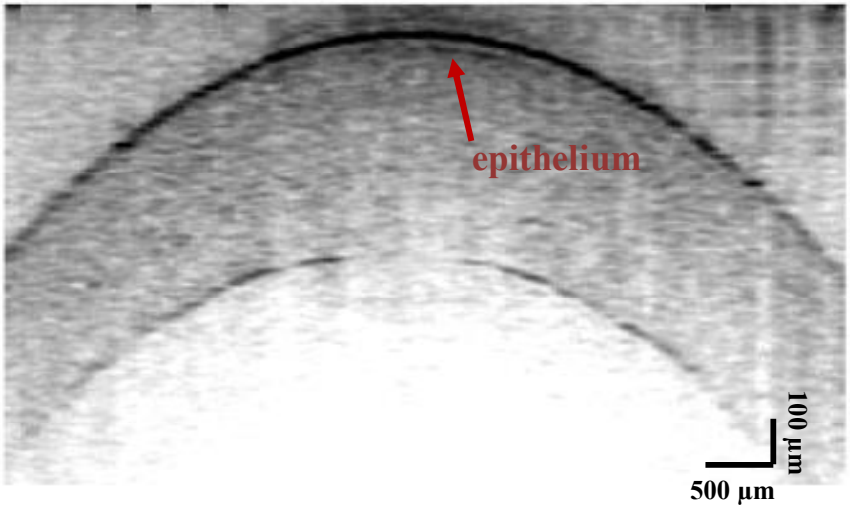

Figure 3.6 Cross-sectional image of a human cornea measured by the conventional SD-OCT system. The red arrow indicates the epithelium layer in the cornea.

For imaging the donor cornea, lateral scan was performed by moving the sample tissue via a translation stage. Fig. 3.6 shows the cross-sectional image of the cornea. The image consists of 300 A-scans, with an image size of 1×6 mm^2. In the centre of the image, the epithelium can be seen.

3.3 Single shot SD-OCT

3.3.1 System setup

Fig. 3.7 shows the experiment setup of the single-shot SD-OCT system. The light source is the same SLD as that used for the single-point configuration. The collimated light beam was focused in a line field by a cylinder lens (f=50mm). After going through a 45:55 beam splitter and a pair of achromatic doublet lenses (f=40mm), the line fields were relay focused onto the sample object surface and the reference mirror. The backscattered and back-reflected light from the sample and reference reflector are recombined at the exit of the beam splitter and then collected by a convex lens (f=50mm). Finally the recombined light was delivered to a spectrometer. The spectrometer uses a 2D CMOS camera (Andor) contains 2560×2160 pixels and a spectrograph (Andor) provides 0.1 nm spectral resolution.

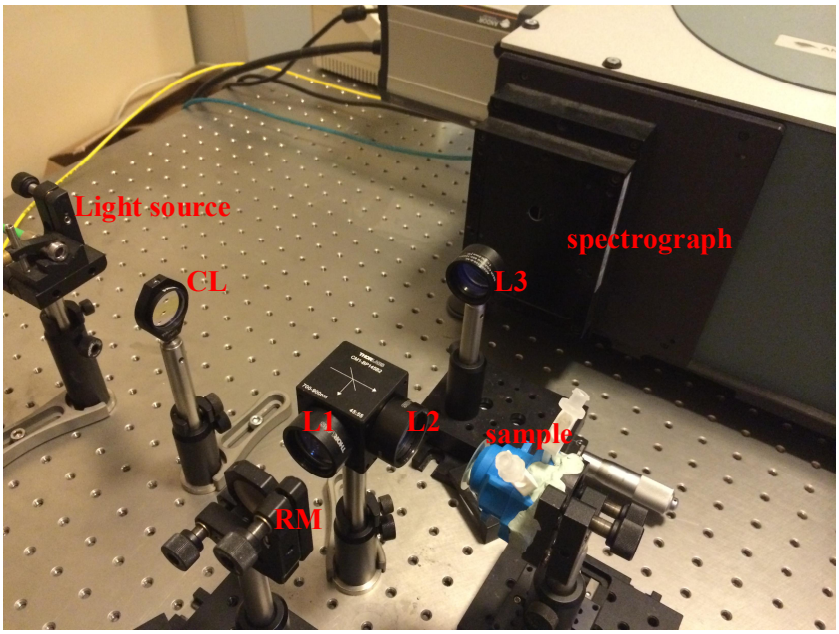

Figure 3.7 Photograph of the single-shot OCT system. L1, L2 and L3: achromatic doublet lenses; CL: cylinder lens; RM: reference mirror.

3.3.2 Performance

A. Axial resolution

The theoretical axial resolution determined by the spectral FWHM of the light source is 2.3 εm which should be the same as the single-point SD-OCT system. However, the spectrometer used in the single-shot SD-OCT system only covers the spectrum in the range from 778 nm to 860 nm which is narrower than the bandwidth of the light source. This leads to a degradation of axial resolution. Therefore, as shown in Fig. 3.8 the actual axial resolution determined by the FWHM of the main peak in the 650 μm glass slide depth profile is about 5 εm.

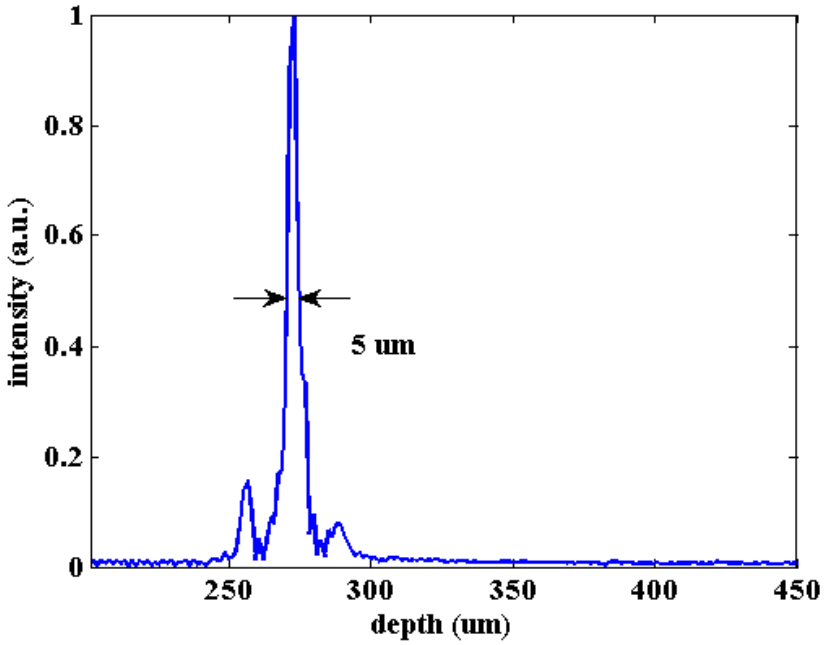

Figure 3.8 Depth profile of 650 μm glass slide obtained by the single-shot OCT system. The axial resolution determined by the FWHM of the main peak is about 5 μm.

B. Imaging depth

Since the spectral resolution provided by the spectrograph is 0.1 nm and the centre wavelength of the light source is 844 nm. The maximum imaging depth of the system determined by Eq. (2.16) is about 1.8 mm in air.

C. Lateral image width

The diameter of the collimated beam is 2.1 mm and the length of the line field on the sample is 1.7 mm. Hence, the imaging width was 1.7 mm, which is the same as the length of the line field. The pixel size of the used 2D CMOS sensor array is 6.5 εm. Since there is a magnification of 1.2 between the real sample object and the camera grabbed image, the lateral step size on the sample is 5.2εm.

3.3.3 Testing cross-sectional image

The onion epidermis was imaged by the built single shot SD-OCT system. Fig. 3.9 (a) shows its cross-sectional image. The cross-sectional image consists of 300 A-scans and the image size 0.7×1.5 mm^2.

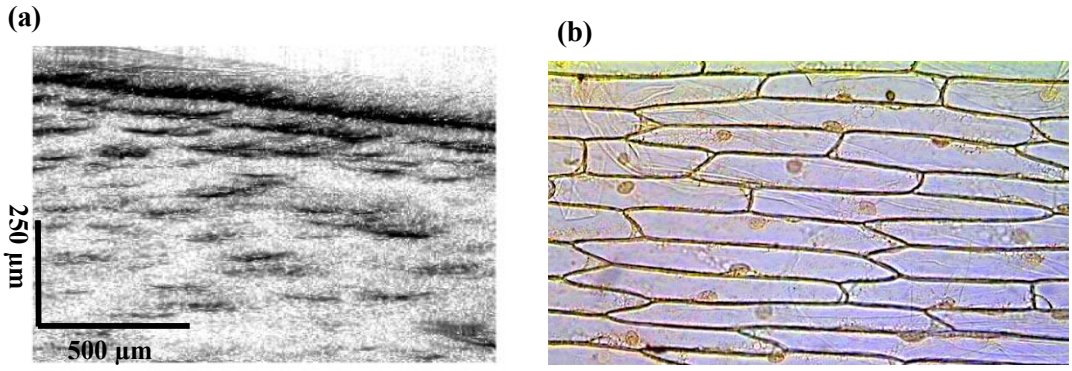

Figure 3.9 (a) Cross-sectional image of onion cell measured by single-shot SD-OCT system. (b) Onion cell obtained by microscopy [7]

3.4 Summary

In summary, two free space SD-OCT configurations were developed for pharmaceutical and medical applications.

Firstly, the single-point SD-OCT system was implemented using a line camera based spectrometer. The axial and lateral resolution achieved by the single-point SD-OCT system was 2.6 µm and 16 µm respectively. It measured a whole spectrum in a single exposure. To generate cross-sectional image, a mechanical lateral scan process was

required by either sweeping the sample beam or moving the sample object. Measurements on the tip of thumb and a donor cornea confirmed that the developed single-point SD-OCT system is capable of imaging the inner structures of a sample.

Secondly, the single-shot SD-OCT system was implemented by using a 2D camera based spectrograph which allowed the whole B-scan map to be measured in a single-shot fashion. Compared with the single point configuration, single-shot SD-OCT utilised a parallel data acquisition scheme thus is able to grab multiple A-scan spectra in a single exposure. Hence the cross-sectional image generated by the single-shot configuration does not require any mechanical scanning process. An onion epidermis was used as an example to demonstrate its capability for imaging the inner structure of a sample. The achieved axial and lateral resolution of the single shot SD-OCT system are 5 μm and 5.2 μm respectively.

References:

1. B. Potsaid, I. Gorczynska, V. J. Srinivasan, Y. Chen, J. Jiang, A. Cable, and J. G. Fujimoto, ñUltrahigh speed spectral /Fourier-domain OCT ophthalmic imaging at 70,000 to 312,500 A-scans/s,ò Opt. Express **16**: 15149ï 15169 (2008).
2. B. Grajciar, M. Pircher, A.F. Fercher, R.A. Leitgeb, ñParallel Fourier domain optical coherence tomography for in vivo measurement of the human eye,ò Opt. Express **13**:1131-1137 (2005).
3. Y. Zhang, J.T. Rha, R.S. Jonnal, D.T. Miller, ñAdaptive optics parallel spectral domain optical coherence tomography for imaging the living retina,ò Opt. Express **13**: 4792-4811 (2005).
4. Y. Nakamura, S. Makita, M. Yamanari, M. Itoh, T. Yatagai, Y. Yasuno, ñHigh-speed three-dimensional human retinal imaging by line-field spectral domain optical coherence tomography,ò Opt. Express **15**: 7103-7116 (2007).
5. Z. Yaqoob, W. Choi. S. Oh, N. Lue, Y. Park, C. Fang-Yen, R.R. Dasari, K. Badizadegan, M.S. Feld, ñImproved phase sensitivity in spectral domain phase microscopy using line-field illumination and self phase-referencing,ò Opt. Express **17**:10681-10687 (2009).
6. S. Witte, M. Baclayon, E.J.G. Peterman, R.F.G. Toonen, H.D. Mansvelder, M.L. Groot, ñSingle-shot two-dimensional full-range optical coherence tomography achieved by dispersion control,ò Opt. Express **17**: 11335-11349 (2009).
7. URL: https://mohtadialkhaliq.wordpress.com/2011/02/05/observing-onion-cells/

Chapter 4 SD-OCT for pharmaceutical application

4.1 Introduction

In modern manufacturing processes of solid pharmaceutical dosage forms, coating is a widely used unit operation. Pharmaceutical coating has a wide range of functions such as masking bitter taste and unacceptable odour, improving aesthetic appearance, increasing stability and separating incompatible substances [1]. Moreover, in the past decades pharmaceutical coating has increasingly been used to control the release profile of active pharmaceutical ingredients (API) to achieve desirable API absorption profiles in the human body [2]. As the quality of the functional coating has a direct impact on the therapeutic efficiency, there is a critical need for analytical techniques to non-destructively assess the coating quality of pharmaceutical dosage forms.

Traditionally the quality of pharmaceutical coating has been evaluated by empirical knowledge and calculations relating to weight gain with respect to the amount of coating solution applied. Hence only the average coating thickness of a batch of pharmaceutical tablets or pellets can be obtained [3]. Previously TPI proved to be a powerful method for the non-destructive evaluation of coatings on large pharmaceutical tablets [4-7]. Since most pharmaceutical excipients used in film coating are either transparent or semi-transparent in the terahertz frequency range [4], TPI can be used to quantify thick pharmaceutical coatings in the range of 40 ï 140 µm and beyond [8]. Recently, we and other groups have demonstrated that SD-OCT provides an alternative way for imaging and characterizing the thickness of pharmaceutical tablets coating [8-11]. SD-OCT usually uses near infrared light, which has much shorter wavelength as compared with terahertz radiation, thus OCT has intrinsically higher spatial resolution than the terahertz imaging method. Consequently tablet coatings with a layer thickness range of 10 ï 60 ε m can be measured quantitatively [8]. In this work, we demonstrated that the developed free space SD-OCT systems are powerful process analytical tools for characterising the tablet coating structure

over a wide thickness range.

Very recently we further demonstrated that coating structures of small pharmaceutical pellets with a diameter smaller than 1 mm could be easily imaged by using a time domain FF-OCT system [12]. However, although the FF-OCT uses a parallel data acquisition scheme, it requires a mechanical depth scanning process to generate depth profiles. Therefore it takes about one minute to record a full set of OCT data and is hence not suitable for on-line application. Unlike FF-OCT, SD-OCT takes a single depth profile in sub-microsecond scale, which requires no depth scanning. It can acquire several thousands of A-scans in one second, and is capable for both off-line and on-line application.

In this work, firstly, the off-line measurements of small size pellet coating structure were performed on free space SD-OCT systems. The galvo mirror in the free space system was replaced by a translation stage for mechanical lateral scanning in order to collect more back scattered photons. Two film coated pellets with diameter less than 1 mm were measured. The first one has two coating layers and their thicknesses evaluated from the mean depth profile are 38 µm and 50 µm respectively. The second pellet exhibited a single film coating layer and its coating thickness was determined to be 90 µm. Then online measurements of pellet coating structure were performed using a compact and portable fibre based SD-OCT system. The flexible sonsor head can be easily integarted into a pharmaceutical coater. Using the developed fiber-based SD-OCT system, we were the first group to image the multiple pellet coating layers and to quantify their thicknesses. However, a degradation of axial and lateral resolution was found when the small pellets are moving at high speed. We believe that this problem could be easily solved by using a high speed spectrometer.

4.2 Material

4.2.1 Coated tablet

The tablet cores were biconvex (3 mm in height, 8 mm in diameter and an average weight of 252 mg), and contained 10% w/w diprophyllin (API), 84.5% w/w lactose monohydrate (Flowlac), 5% w/w vinylpyrrolidoneï vinyl acetate copolymer (Kollidon VA 64) and 0.5% w/w magnesium stearate. The coating formulation used was as

follows: 50% w/w polyvinyl acetate (Kollicoat SR 30 D), 6% w/w polyvinyl alcoholï polyethyleneglycol graft copolymer (Kollicoat IR), 0.075% w/w polyoxyethylene (20) sorbitan monooleate (Polysorbat 80), 0.3% w/w glycerolmonostearate, 0.75% w/w triethylcitrate and 42.87% w/w deionised water.

The tablets were coated by ABFC25, Bohle Film Coater (L.B. Bohle, Ennigerloh, Germany). The coating pan dimensions are 546 mm in diameter and 630 mm in length. The coating process was carried out in the same manner as for the lab batch with similar coating parameters (slight changes were necessary to accommodate the increased batch size). Five of the two-way spray nozzles (type 970/7-1 S75) were used (Düsen-Schlick GmbH, Untersiemau, Germany) to spray coat the tablets. Random selection of ten tablets was carried out after the following amounts of sustained-release polymer were applied: 1.8, 3.6, 5.5, 7.3, 9.1, 10.9, 12.7, 14.5 and 18.2 mg/cm^2. All sampled tablets were stored and measured under the same ambient conditions. Fig. 4.1 shows a photograph of a film coated tablet.

4.2.2 Coated pellet

The off-line measurement samples used in the presented work were pellets with two different diameters. The first two layers coated pellet is approximately spherical with an outer diameter of about 850 εm. The core is a microcrystalline cellulose (MCC) sphere (Celphere MCC seed core CP-507, Asahi Kasei Corp., Tokyo, Japan). The inner coating layer is a drug-loaded layer containing 10% API and 90% hydroxypropyl methylcellulose (HPMC). The outer coating formulation contains a combination of ethyl cellulose and hydroxypropyl cellulose. The second pellet is with an diameter of 350 µm. The core and the coating layer are the same as the core and inner coating of the 850 µm pellet. Fig. 4.1 also shows a photograph of a film coated pellet.

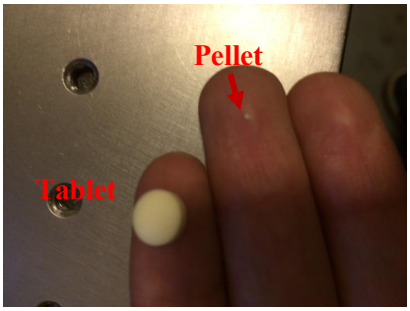

Figure 4.1 Photograph of film coated tablet and pellet.

4.3 Experiment results on pharmaceutical tablets

4.3.1 Cross-sectional image of coated tablet

Data acquisition

All coated tablets were imaged by the single-point SD-OCT system. First of all, a background spectrum was recorded when the tablet samples were not placed in the sample arm in order to remove the coherent noise contributed by the reflection of other optical components, such as multimode fibre, in the system. Then the sample beam was swept by the galvo scanning mirror to perform a lateral scan over a range of 5 mm. The spectrometer grabbed the spectral interferogram on 500 lateral pixels for each tablet and the distance interval between adjacent lateral pixels was calibrated as 10 μm. At each lateral pixel, two interferograms were grabbed with a phase difference of ´ introduced using a PZT actuator to shift the reference mirror in a distance of $\partial_0/4$, where ∂_0 is the centre wavelength of the light source. The DC, autocorrelation terms and the coherent noise were removed in their differential interferogram [13]. The acquisition rate of the system is 120 A-scans per second, hence the data acquisition time for each tablet was 8s. This rate was limited by the output rate of the DAQ card that is used as a controller of the galvo mirror.

Phase shift method

The background spectrum was firstly subtracted from all the measured interferograms to remove the coherent noise. The differential interferogram between the two measured interferograms at each lateral pixel were then interpolated from wavelength

domain to wavenumber domain. After that, FT was applied to the interpolated differential interferograms to obtain the complex depth profile. Finally, the magnitude response of the complex depth profiles was generated to display the cross-sectional image. Fig. 4.2 (a) shows two original spectral interferogram measured at the same lateral pixel with a phase difference of ´/2. The inset shows their differential interferogram. Fig. 4.2 (b) shows the cross-sectional image of the tablet coated by 5.5 mg/cm^2 polymer film without using the phase shift method. The DC components and the coherent noise were removed. However, the autocorrelation noise still remained in the image. Fig 4.2 (c) shows the cross-sectional image of the same tablet generated by the phase shift method. It shows that the autocorrelation noise was further removed. Fig 4.2 (d) and Fig. 4.2 (e) show one of their depth profiles. It is obvious that the phase shift method provides a better imaging quality.

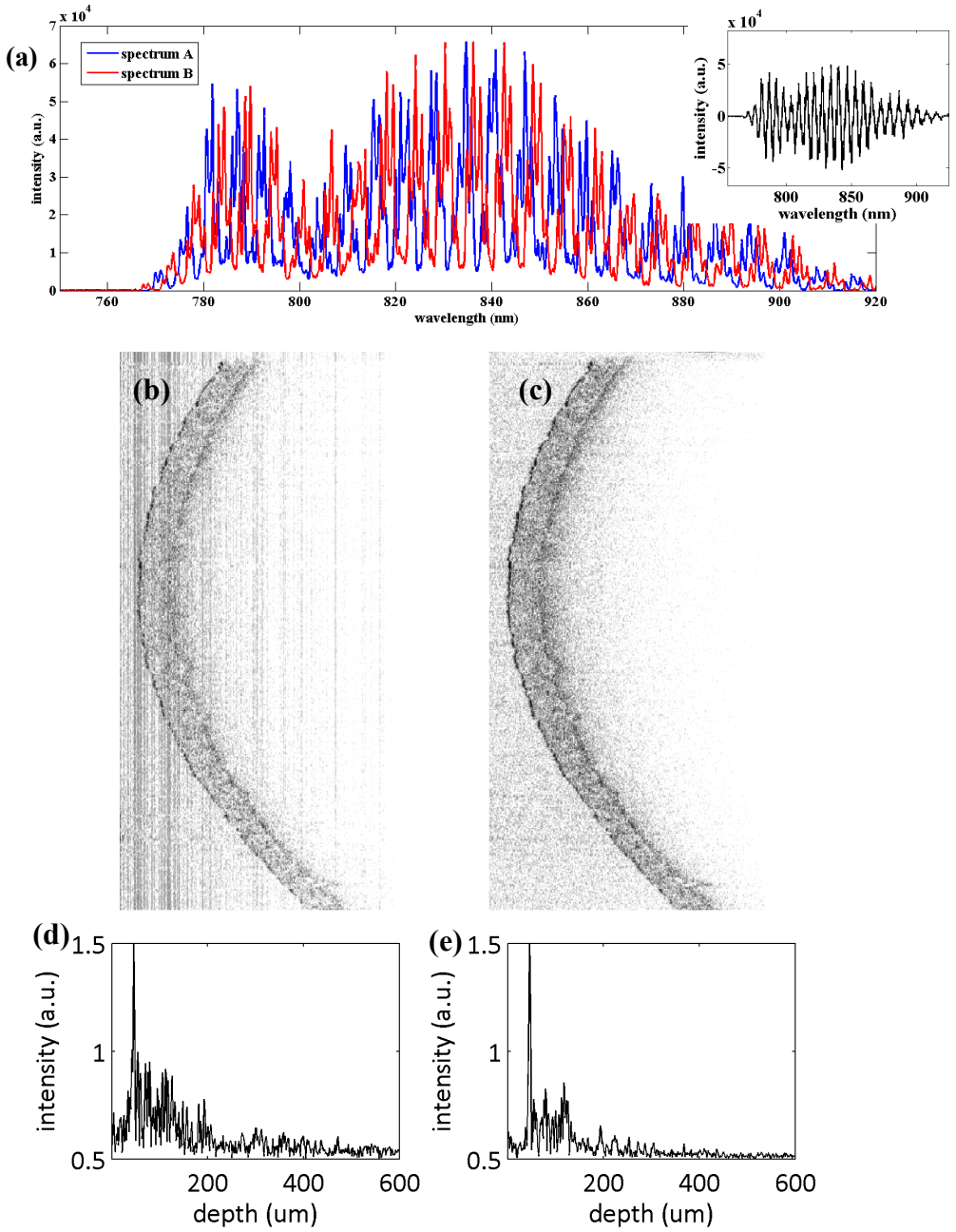

Figure 4.2 (a) Two spectral interferograms at the same lateral pixel with a phase shift of π/2. The inset is the differential spectrum of the two original spectral interferogram. (b) Cross-sectional image obtained using one set of the original spectral interferogram, and (e) one of its depth profiles. (c) Cross-sectional image obtained using the differential interferogram, and (f) one of its depth profiles.

Effect of spectral resolution

The spectral resolution is one of the most important characteristics of a spectrometer. It specifies the maximum number of spectral peaks that the spectrometer can resolve. Assume the response of the over sampled pixels within the spectral resolution range is a constant A:

$$R(k) = \begin{cases} A & \left(k \le \frac{\Delta k}{2}\right) \\ 0 & \left(k > \frac{\Delta k}{2}\right) \end{cases} \tag{4.1}$$

where ŭk = 2´ ŭə/ə^2 is the spectral resolution in wavenumber. The observed signal detected by the spectrometer is the spectral interferogram convoluted with the detection response function R(k) [14]:

$$I_D(k) = I(k) \otimes R(k) \tag{4.2}$$

Hence, in SD-OCT, the spectrometer detected signal is the actual interferogram convoluted with a rectangular function [15, 16]. Due to the convolution property, the Fourier transformed signal in the time/depth domain will be multiplied by a sinc function.

$$\mathcal{F}\{I_D(k)\} \propto \mathcal{F}\{I(k)\} \cdot \mathcal{F}\left\{\frac{\Delta k}{2} \cdot \frac{2}{\Delta k}\right\} = \Delta k \cdot \mathcal{F}\{I(k)\} \cdot \mathrm{sinc}\left(\frac{\Delta k}{2} z\right) \tag{4.3}$$

Therefore, the magnitude response of depth profile is attenuated by the sinc function. Fig. 4.3 shows two sets of glass surface peaks obtained by axial moving the glass slide. Plot (a) and (b) were obtained using the spectra measured by the spectrometers with spectral resolutions of 0.5 nm and 0.12 nm respectively. It is found that the signal peak generated by 0.5 nm spectral resolution spectrometer reduces by about 20 dB at 1 mm and the SNR at 1 mm is less than 2dB. However, for the 0.12 nm spectral resolution spectrometer, the signal peak reduces by only 2 dB at 1 mm and the SNR at the same location is larger than 25 dB.

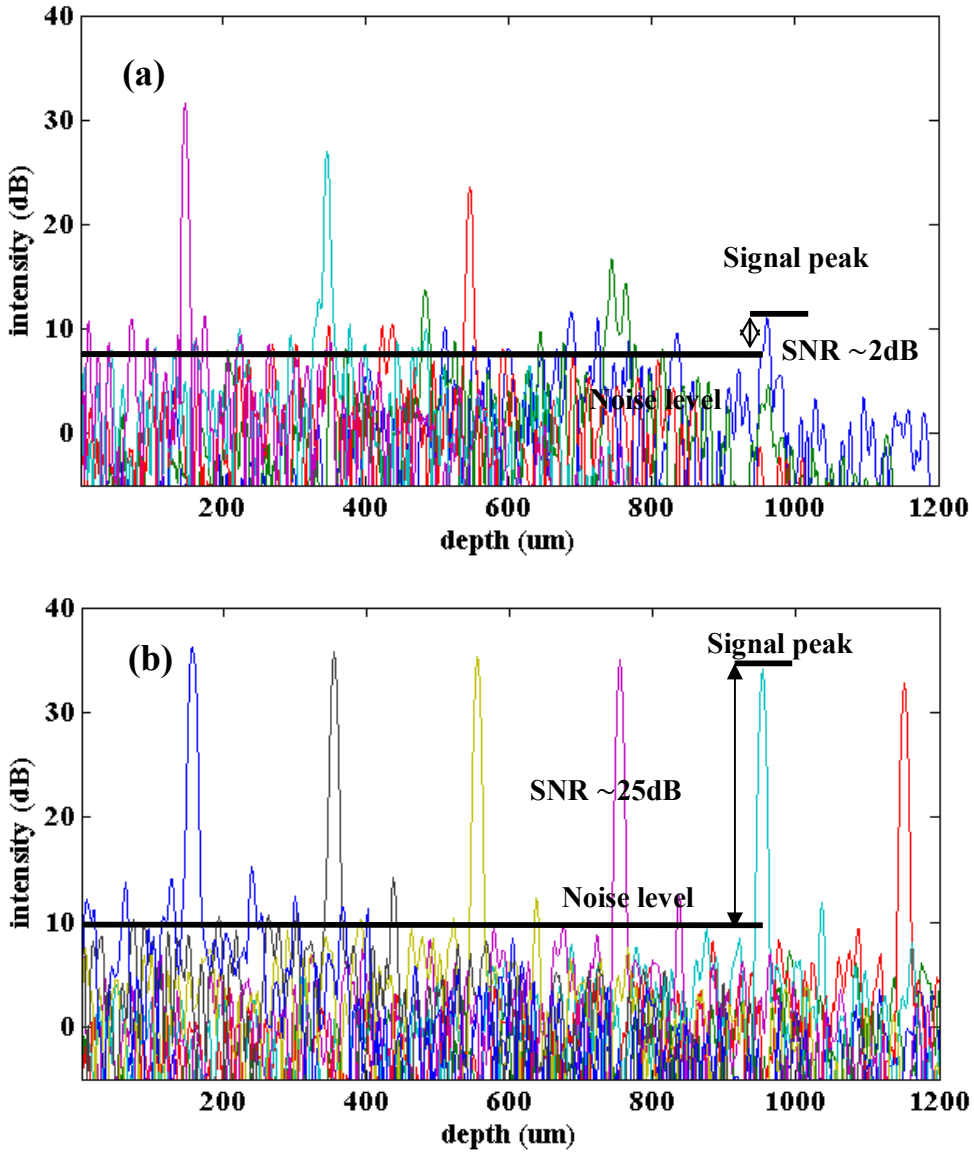

Figure 4.3 Decayed signal peaks along with the increasing OPD between reference mirror and glass surface generated by spectrometers with (a) 0.5 nm spectral resolution and (b) 0.12 nm spectral resolution. The SNR reduces to (a) 2 dB and (b) 25 dB at 1 mm respectively.

Fig. 4.4 (a) and (b) show the cross-sectional images of tablet coated with 18.18 mg/cm^2 polymer measured by the two spectrometers respectively. In both cross-sectional images, the surface is clearly visible. However, the coating/core interface is much easier to distinguish in Fig 4.4 (b) compared to Fig 4.4 (a).

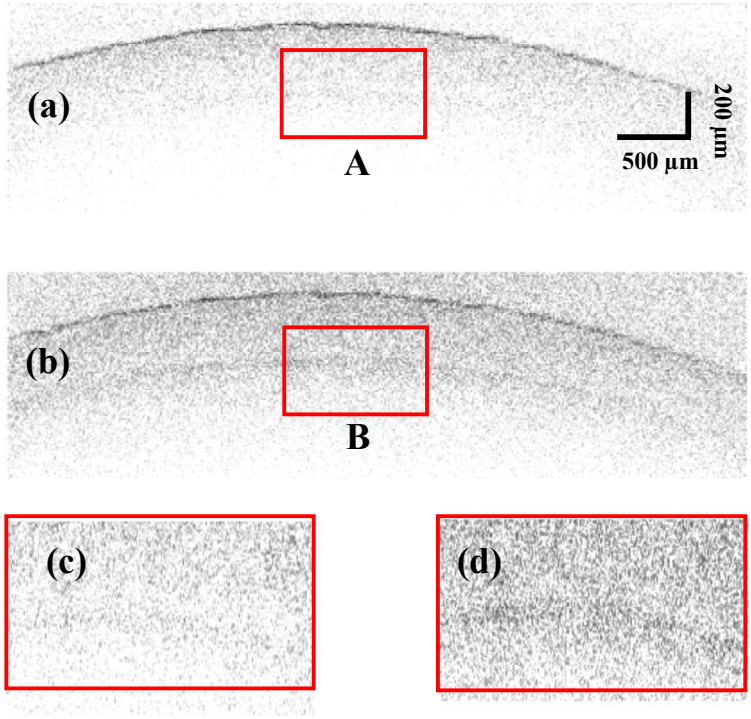

Figure 4.4 Cross-sectional images of coated tablet measured by (a) 0.5 nm spectral resolution spectrometer and (b) 0.12 nm spectral resolution spectrometer. (c) The enlarged window A and (d) the enlarged window B.

Effect of reduced bit depth of ADC

The spectrometer in the SD-OCT system uses an analogue to digital converter (ADC) to digitalise the measured analogue signal. The bit depth of used ADC limits the readout speed of the spectrometer which in turn impacts the imaging speed. Meanwhile, the measurement data file size also grows with increasing bit depth of used ADC. Hence, the reduction of ADC bit depth is significant for real-time and online applications. However, digitalisation of the analogue signal will introduce a quantisation noise, which has the potential to contaminate the OCT image. In this section, the effect of reducing the bit depth of ADC on the quality of the OCT image is discussed.

Assume the maximum measured voltage is V_{max} and quantised by an N-level uniform quantiser (N bits ADC). The level step is:

$$\Delta = \frac{V_{max}}{2^N} \tag{4.4}$$

The error e between the actual measurement value and the quantised value is in the range of ï qp/2 to qp/2. With the assumption that any value of the error appears in the same probability p(e)=1/qp, the variance of the quantisation error could be derived by:

$$\sigma_q^2 = \int_{-\Delta/2}^{\Delta/2} e^2 p(e)\,de = \frac{1}{\Delta}\int_{-\Delta/2}^{\Delta/2} e^2\,de = \frac{1}{\Delta}\cdot\frac{1}{3}e^3\Big|_{-\Delta/2}^{\Delta/2} = \frac{\Delta^2}{12} \tag{4.5}$$

In order to study the effect of reduced ADC bit depth, the raw data that was acquired at a resolution of 14 bits were re-quantised to 12, 10, 8, 6 bits respectively by:

$$I_q(k) = \text{floor}\left(\frac{I(k)}{2^{14-N}} + 0.5\right) \tag{4.6}$$

The re-quantised spectral interferograms were than processed as previously described to generate the respective depth profiles and cross-sectional images. Fig. 4.5 shows the resulting depth profiles generated by 14, 12, 10, 8, and 6 bits depth of ADC. The amplitude of the normalised signal almost remains constant for all bit depths. The noise level almost stays the same for 14 bits to 10 bits. When the bit depth reduced to 8 bits, the noise level increased less than 1dB. When the bit depth reduced to 6 bits, the noise level increased more than 5 dB.

Fig. 4.6 shows the cross-sectional images of the tablet coating generated by 14 to 6 bits depth of ADC quantised spectral interferograms. The windowed area of each image is enlarged and shown on the right hand side. It is found that the coating/core interface is clearly visible for 14, 12, 10 and 8 bits ADC. For a 6 bits ADC, we lost some coating/core interface features.

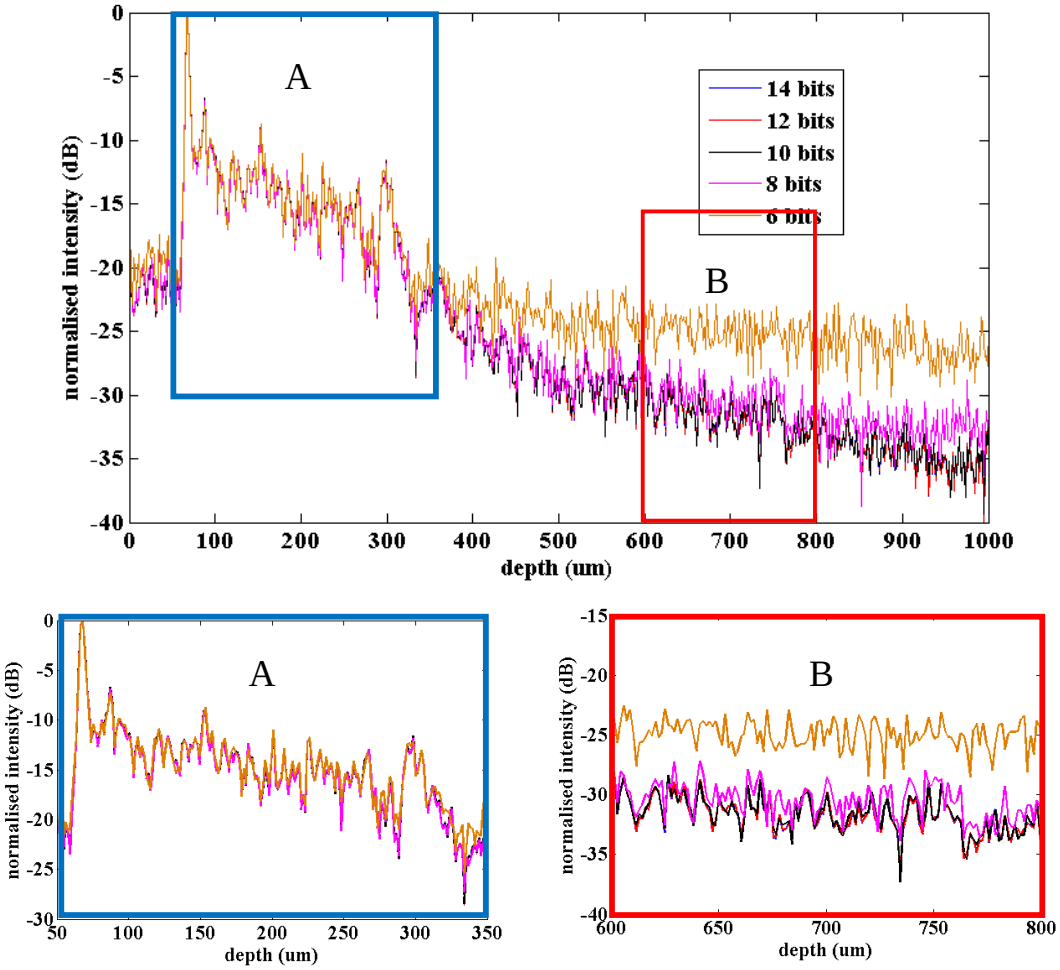

Figure 4.5 Depth profiles of coated tablets generated by 14, 12, 10, 8, and 6 bits depth of ADC quantised spectral interferogram.

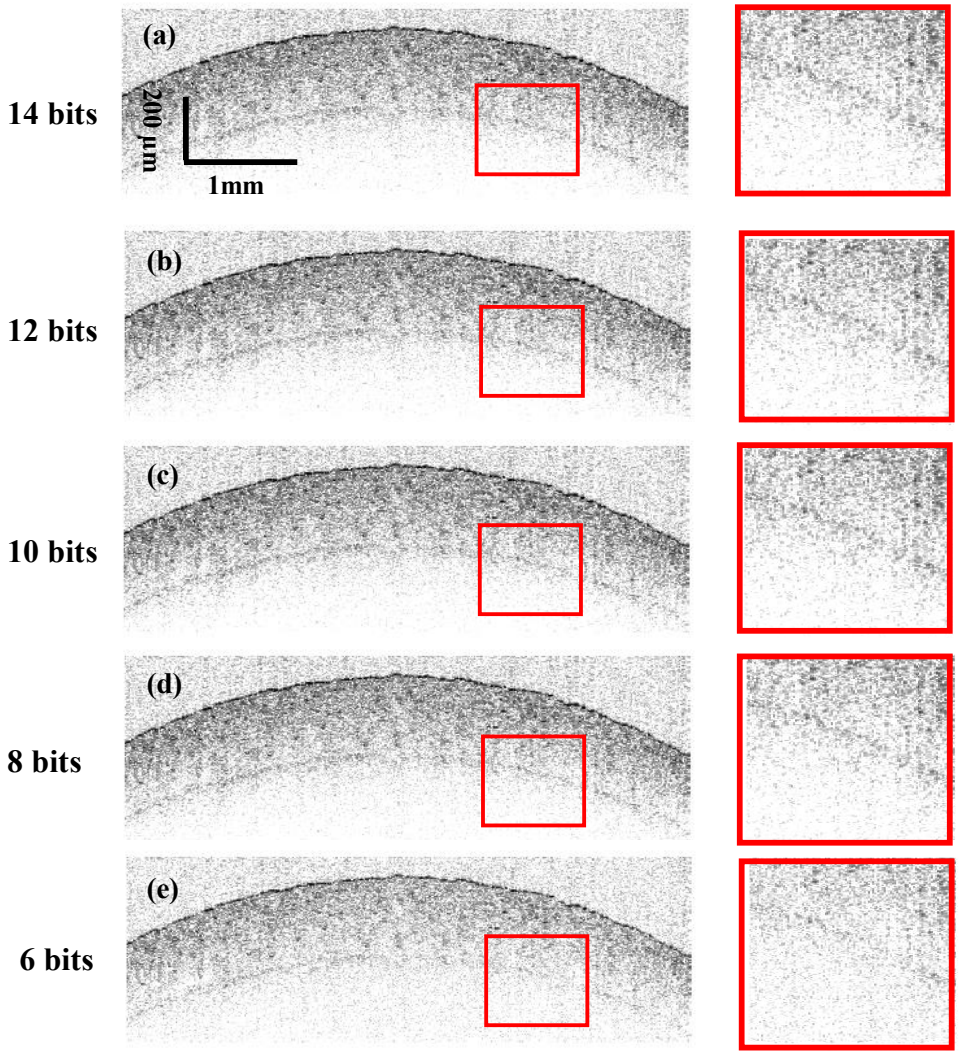

Figure 4.6 Cross-sectional images of the tablet coating generated by (a) 14, (b) 12, (c) 10, (d) 8, (e) 6 bits depth of ADC quantised spectral interferograms. The windowed area of each image were enlarged and shown on the right hand side.

Cross-sectional images of all coated tablets

Fig. 4.7 shows the cross-sectional images of all imaged tablets. Each of the cross-sectional images contains 500×487 pixels, corresponding to an image size of 5×0.6 mm^2. The lateral pixel size is 10 μm and the axial pixel size is 1.48 μm when assume the refractive index of the film coating is 1.5 [8]. In order to achieve a better image quality, each depth profile was divided by its mean value. All the computing work was performed by Matlab R2013a, taking 4s for one cross-sectional image (hardware specification: Intel i5 Quad Core CPU at 3.4GHz, 8GB memory).

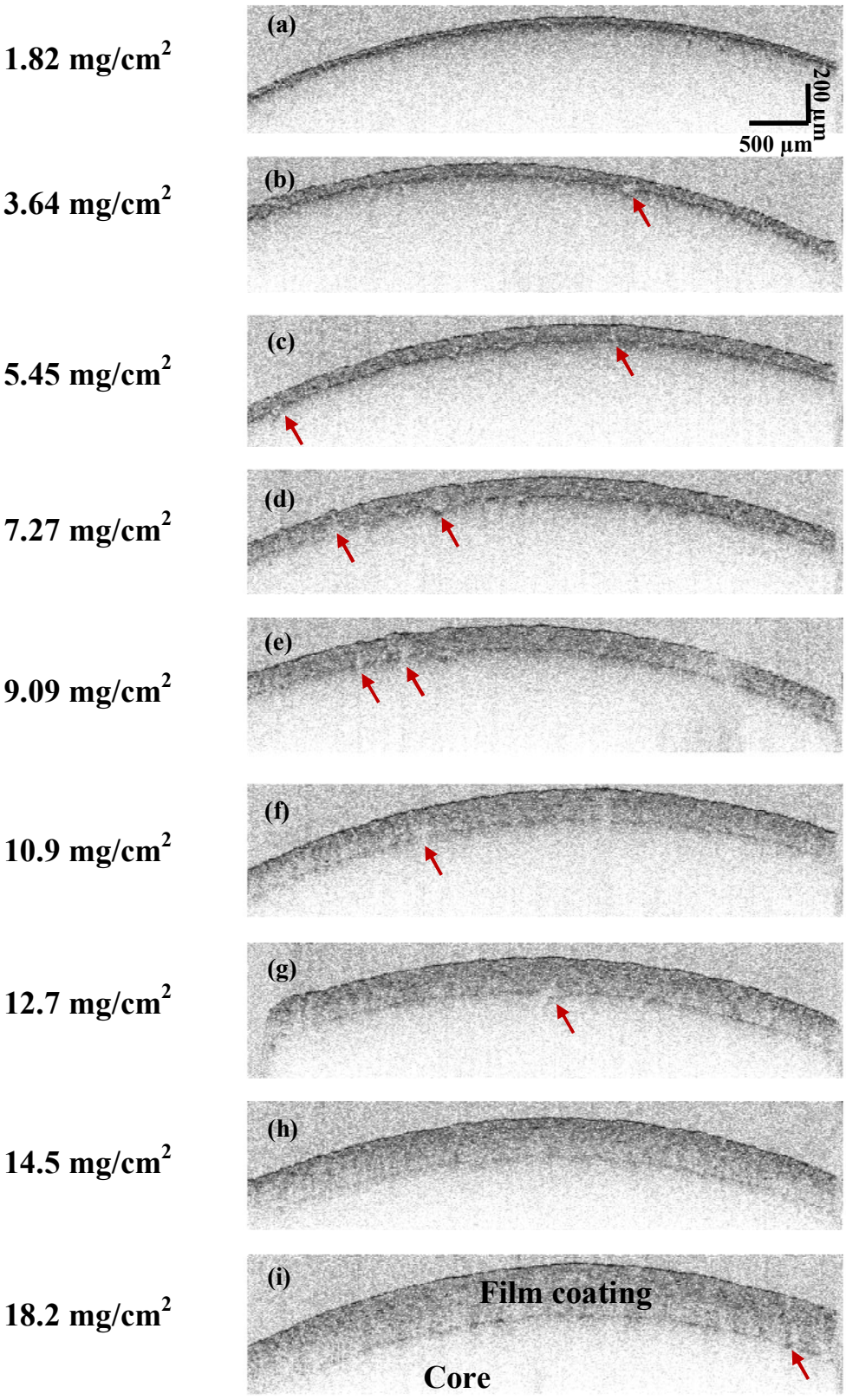

Figure 4.7 Cross-sectional images of tablets coated in different amount of polymer. The image size of each cross-sectional image is 5×0.6 mm^2. The red arrows indicate the air bubble in side the coating layer.

From top to bottom in Fig. 4.7, the amount of polymer applied in the coating process increases from 1.82 mg/cm^2 to 18.2 mg/cm^2. The coating/core interfaces can be clearly distinguished in all the cross-sectional images, the thickness of the coating layer increasing with the increased weight gain. In addition, some defects indicated by the red arrows could be seen in the images. These defects are caused by the inclusions of air during the coating process [10].

Coating thickness evaluation

Many particle-like features and air bubble defects can be seen in all the cross-sectional images of the tablet coating layers. Therefore, the position of coating/core peak may not be precisely determined using a single OCT depth profile. In order to determine the coating thickness in a robust and automatic way, the mean depth profile averaged over 50 neighbouring depth profiles was used to calculate the mean coating thickness [12]. Due to the surface curvature of the tablet sample, all the surface peaks in depth profiles were shifted to the same position. Fig 4.8(a) shows 5 randomly selected OCT depth profiles of the tablet coated in polymer film with a weight gain of 5.45 mg/cm^2. Indeed, there are many particle-like features originating from particles inside the coating layer. Fig 4.8 (b) shows the mean depth profile of the central 50 depth profiles. The coating/core interface at about 120 μm can easily be identified in the mean profile.

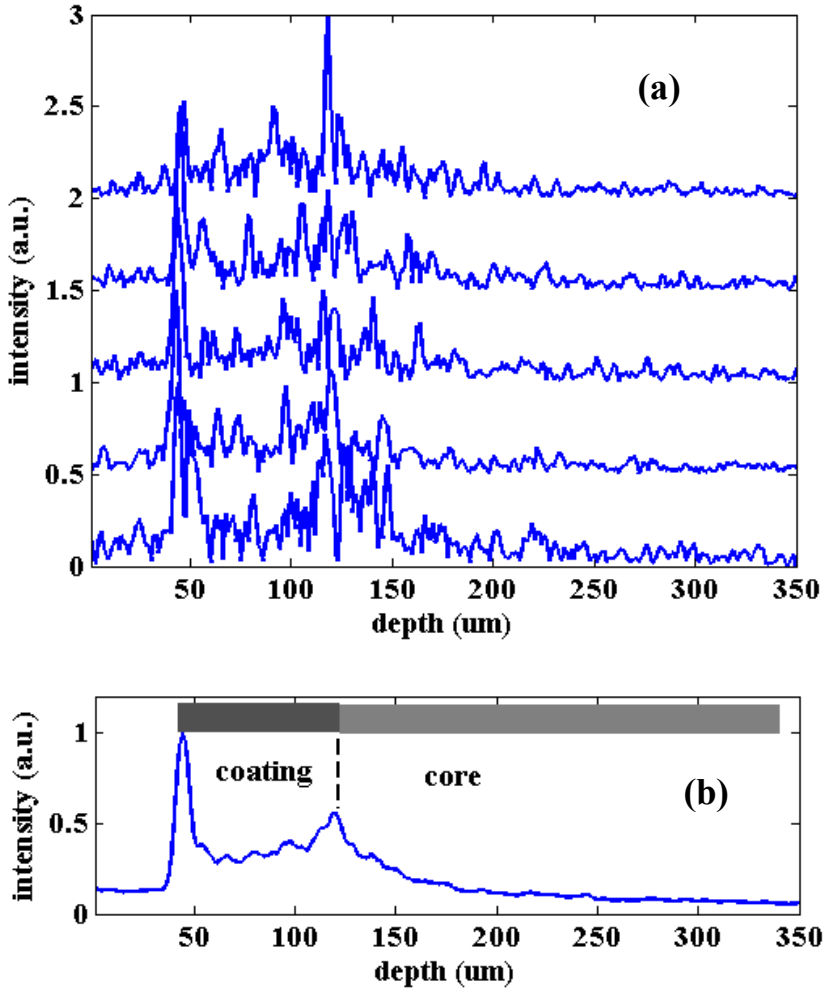

Figure 4.8 (a) Five randomly selected individual depth profiles (b) Mean depth profile of the central 50 depth profiles. The surface peak and coating/core interface can be found in the mean depth profile. The coating thickness is defined by the distance between the two peaks.

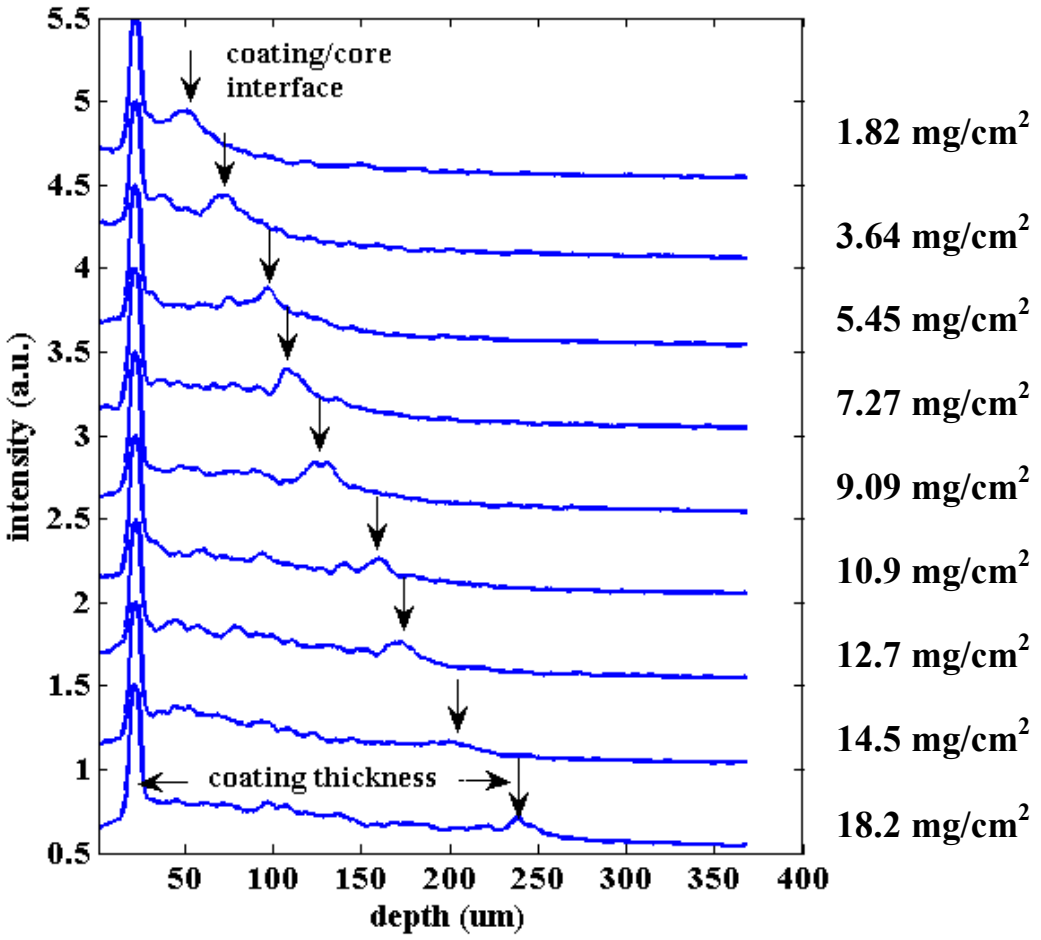

Figure 4.9 Mean depth profiles of all imaged tablets.

Fig. 4.9 shows the mean depth profiles of all the 9 measured tablets generated by averaging the central 50 neighbouring depth profiles. For all tablets, the refractive index of coating layer is assumed as 1.5 [8]. The first peaks of the selected mean depth profiles are the surface peaks, while the other peaks denoting coating/core interfaces are clearly shown. The distance between the two peaks is defined as the coating thickness. As there were 500 depth profiles in each cross-sectional image, 10 mean depth profiles were obtained by averaging every 50 neighbouring depth profiles. Then six of them were selected to compute the coating thickness. The determined thickness was in the range from 30 µm to 220 µm as shown in Fig. 4.10. It can be seen that the thickness of the coating increases almost linearly with the increasing amount of polymer applied in the coating process.

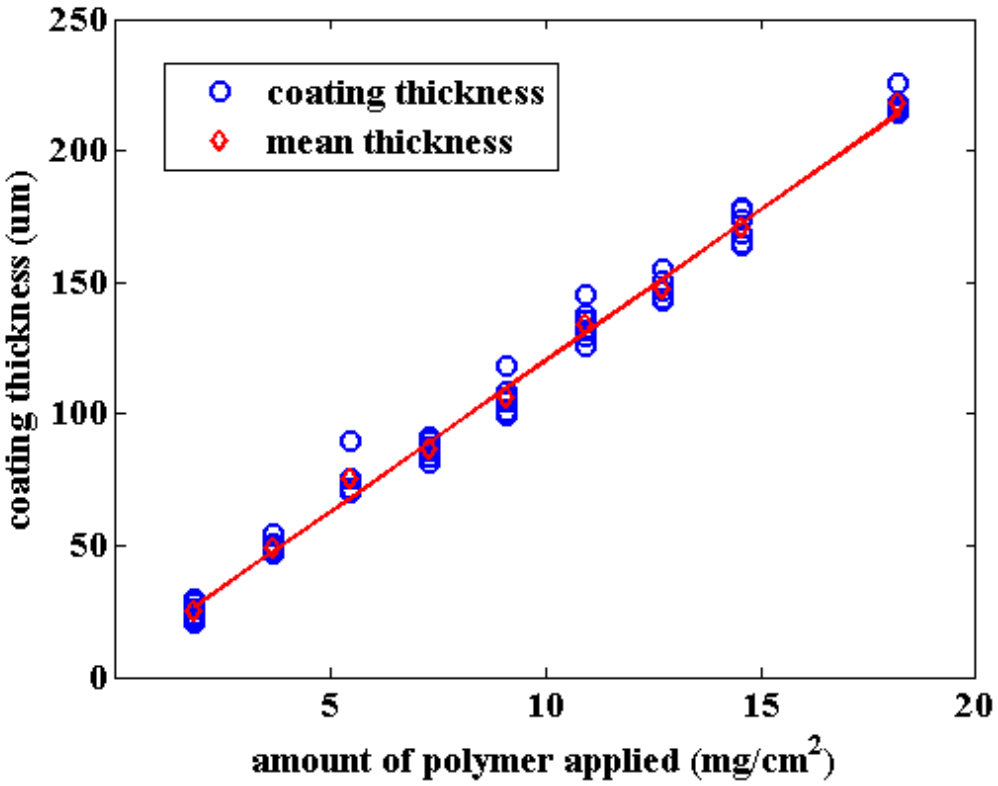

Figure 4.10 Evaluated coating thickness from the mean depth profiles in the range from 30 µm to 220 µm.

4.3.2 Volumetric maps of coated tablets

Data acquisition

The tablets coated with a weight gain of 5.45 mg/cm^2 and 9.09 mg/cm^2 were imaged by the single-shot SD-OCT system to generate their volumetric maps. In the measurement, the single-shot SD-OCT system measured one B-scan, consisting of 200 A-scans in a single exposure. The tablets were continuously moved by a motorised stage to grab the volumetric data. The exposure time was set as 5 ms and the velocity of the stage was set at 2 mm/s. In total, 400 B-scans were grabbed for each of the imaged tablets in 2 s. The scanning area was 1×4 mm.

Data processing

All the depth profiles were generated as had been done previously. However, as the stage was moved continuously, the phase shift method was not used here. It was only

supposed that the reference signal was much bigger than the sample backscattered signal, hence the autocorrelation terms could be neglected. When all the depth profiles had been generated, the mean depth profile was generated by averaging every 5×5 neighbouring depth profiles, thereby obtaining a total of 3200 mean depth profiles for each tablet. A threshold was then used to select the surface and coating/core interface peaks. Fig. 4.11 shows the surface and coating/core interface extracted from all the mean depth profiles.

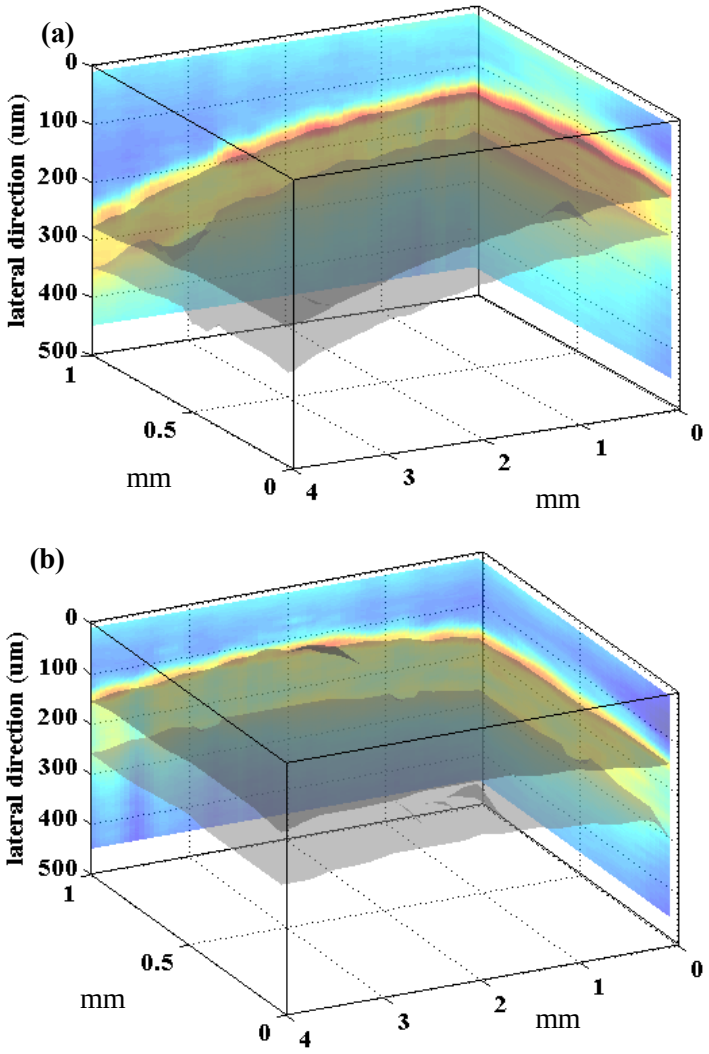

Figure 4.11 Volumetric maps of coating layer with (a) 5.45 mg/cm^2 and (b) 9.09 mg/cm^2 polymer.

Fig. 4.12 shows the distribution of the coating thickness as defined by the distance difference between the selected surface and coating/core interface peaks. Most of the

thicknesses of the tablet coated with an average of 5.45 mg/cm^2 polymer lay within the range of 66-81 µm and its mean thickness was 72 µm, while most of the thicknesses of the tablet coated by 9.09 mg/cm^2 polymer lay in the range of 100-115 µm and its mean thickness was 108 µm.

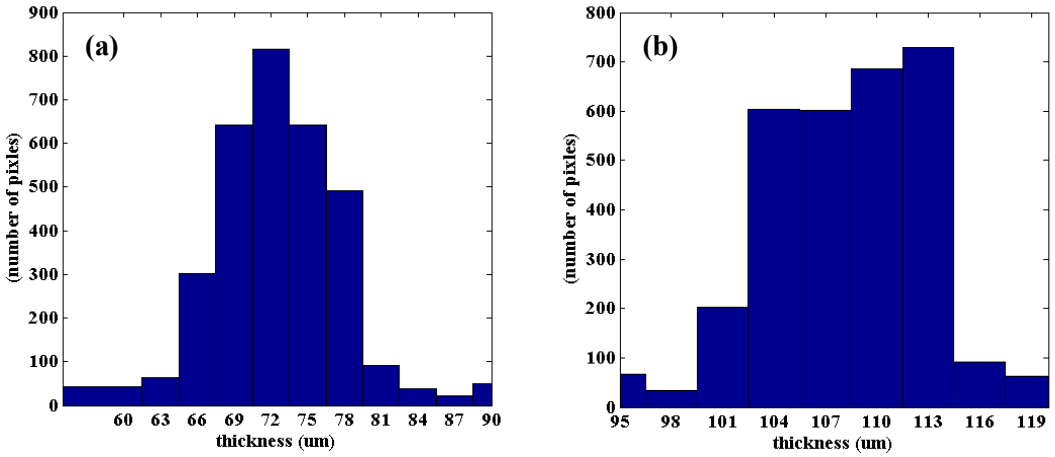

Figure 4.12 Coating thickness distribution of tablet coated with (a) 5.45 mg/cm^2 and (b) 9.09 mg/cm^2 polymer.

4.4 Experiment results of small size pellets

4.4.1 Off-line cross-sectional image of pellets

Data acquisition

Two pellets were imaged using the single-point free space SD-OCT system. The diameters of multi-layer and single-layer coated pellets were in the range of 850-1000 µm and 350-850 µm respectively. The lateral scan were performed by moving the pellets via a motorised stage. For multi-layer coated pellets, the stage moved 1 mm with a step size of 5 µm. Hence, in total 200 lateral pixels were scanned. For the single-layer coated pellet, the stage moved 500 µm with a step size of 2 µm.

Data processing

Fig. 4.13 (a) shows a cross-sectional image of a pellet with a diameter of 850 µm. Two coating layers ware distinguishable. The red dashed lines indicate the respective interfaces. The outer coating layer is quite clean because the coating is fairly uniform. The inner coating layer has many particle-like features which might originate from the API particles and air bubbles. Fig. 4.13 (b) shows the mean depth profile of the 10 neighbouring depth profiles at the centre of the cross-sectional image. Due to the curvature of the pellet, the surface sharp falls when it is far away from the centre pixel. Hence only 10 depth profiles were selected to ensure the surface fall less than 0.5 µm by assuming the pellet is a perfect sphere. The mean thickness of the outer and inner coating layers determined using this the mean depth profile is 38 µm and 50 µm respectively.

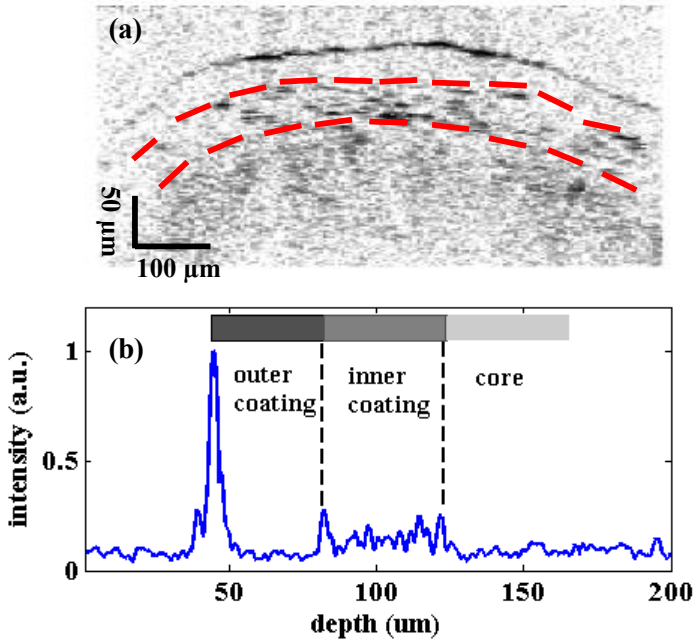

Figure 4.13 (a) Cross-sectional image of an 850 µm diameter wide pellet with two coating layers. The image area is 750×250 µm^2. (b) Mean depth profile of centre 10 depth profiles locate in the centre of the image.

Fig. 4.14 (a) shows a the cross-sectional image of a pellet with an diameter in the range of 350-850 µm. In this sample, only one coating layer can be resolved. The red

dashed line indicates the coating/core interface. Fig. 4.14 (b) shows the mean depth profile of 20 neighbouring depth profiles in the centre of the image. These 20 selected depth profiles also ensure the surface falls less than 0.5 µm. There are multiple peaks in the depth profile corresponding to the particle-like features in the cross-sectional image. These features can be either API particles or air bubbles.

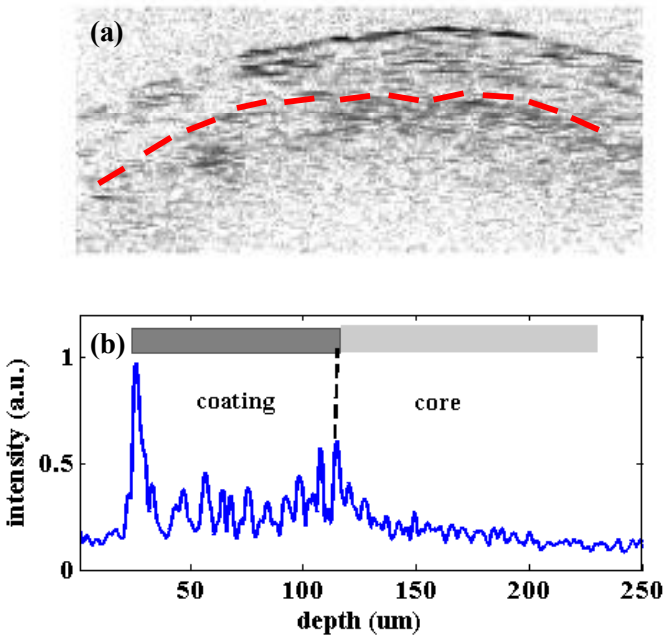

Figure 4.14 (a) Cross-sectional image of 350-850 µm pellet with a single coating layer. The image area is 500×250 µm^2. (b) Mean depth profile of centre 20 depth profiles locate in the centre of the image.

4.4.2 On-line measurement of pellet coating

Cross-sectional images

The online pellets measurement was performed in a fibre based SD-OCT system, which has the advantage of compactness and portability. The fibre based SD-OCT system had a flexible sensor head that can be easily integrated into a pharmaceutical coater. The light source used in the system was centred at 840 nm and has a spectral full width at half maximum (FWHM) of 50 nm, resulting an axial resolution of 6.2 µm in air. The spectrometer grabs about 400 spectra per second. Fig. 4.15 shows the photograph of the fibre based SD-OCT system.

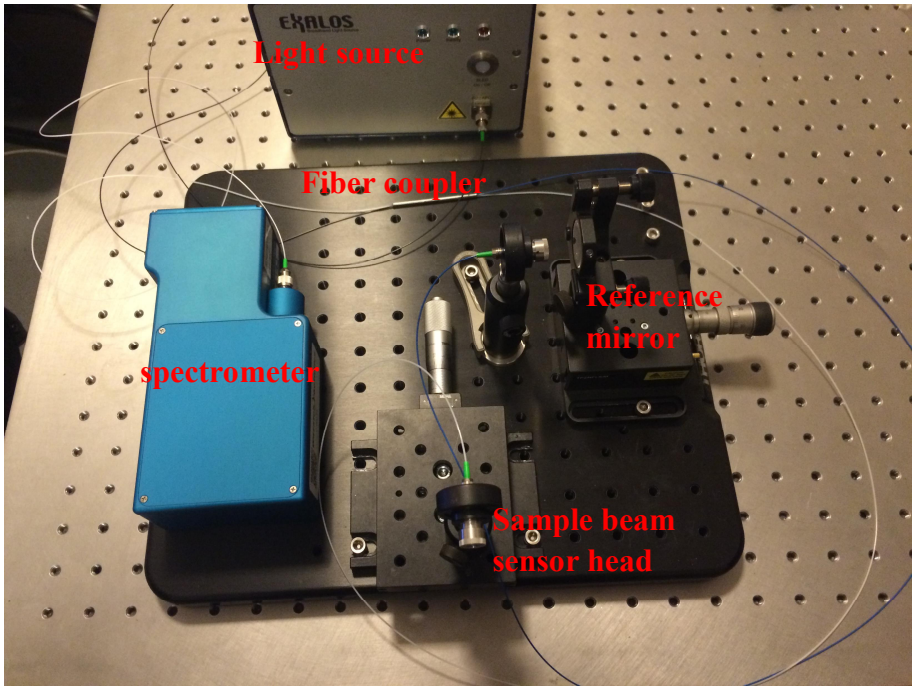

Figure 4.15 Photograph of fibre based SD-OCT systems.

In the measurement, the movement speed of the translation stage was changed from 1mm/s to 20 mm/s to simulate the speed of moving particles inside a coater. Fig. 4.16 shows cross-sectional images of all the imaged 14 pellets at different speeds. Each of the imaged pellets has 3 coating layers, and all 3 coating layers can be distinguished in all the images.

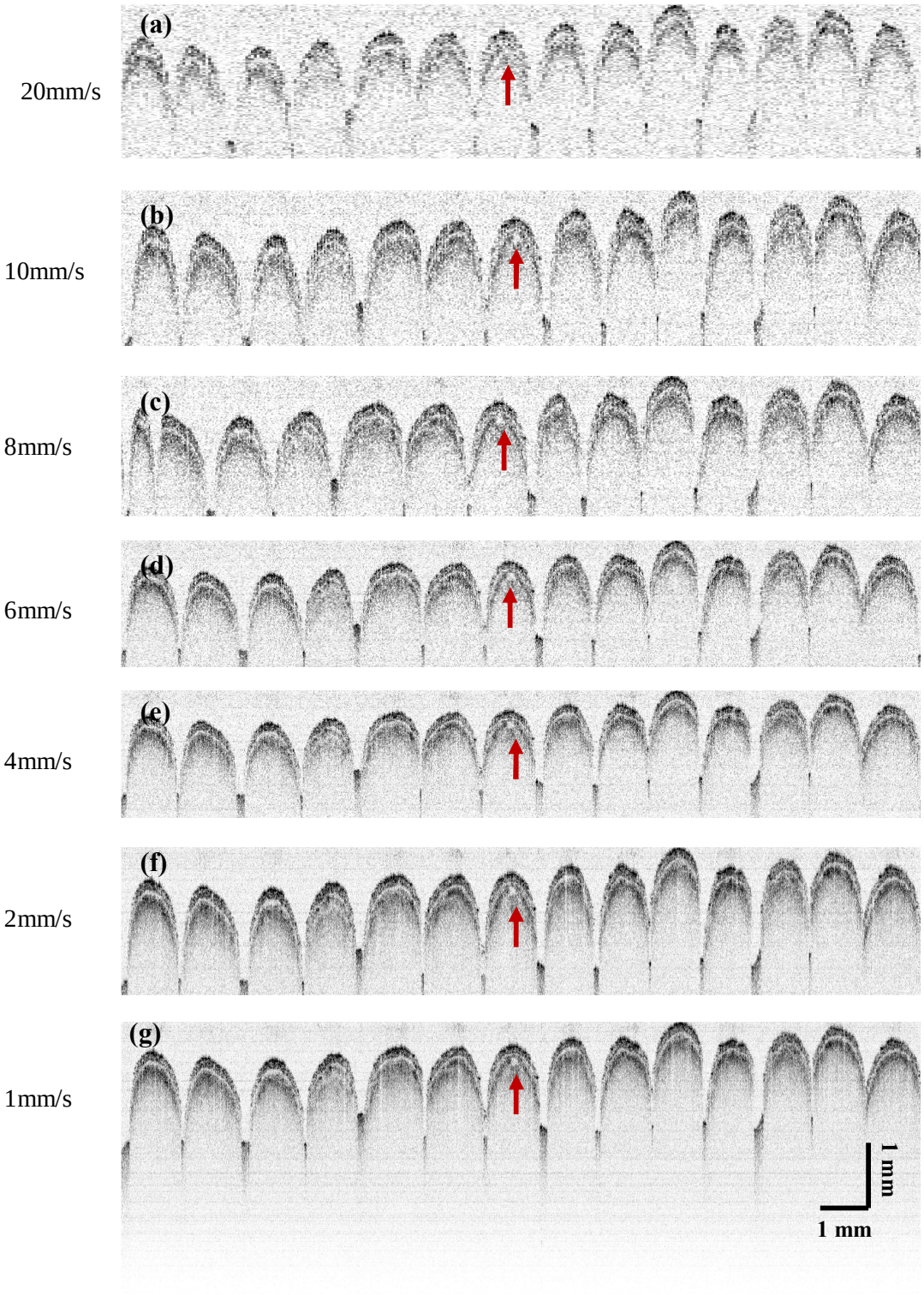

Figure 4.16 Cross-sectional images of all 14 pellets at with (a) 20 mm/s, (b) 10 mm/s, (c) 8 mm/s, (d) 6 mm/s, (e) 4 mm/s, (f) 2 mm/s, and (g) 1 mm/s moving speed respectively.

Evaluation of coating thickness

Fig. 4.17 shows the mean profile of the centre 20 individual profiles of the first pellet moving with 1 mm/s. In order to evaluate the thickness of each coating layer, the boundary between the adjacent two layers was defined as the half way of each raising/falling edge in the mean depth profile. The first layer is 50.3 µm. The second layer is 45.8 µm and the third layer is 66.5 µm.

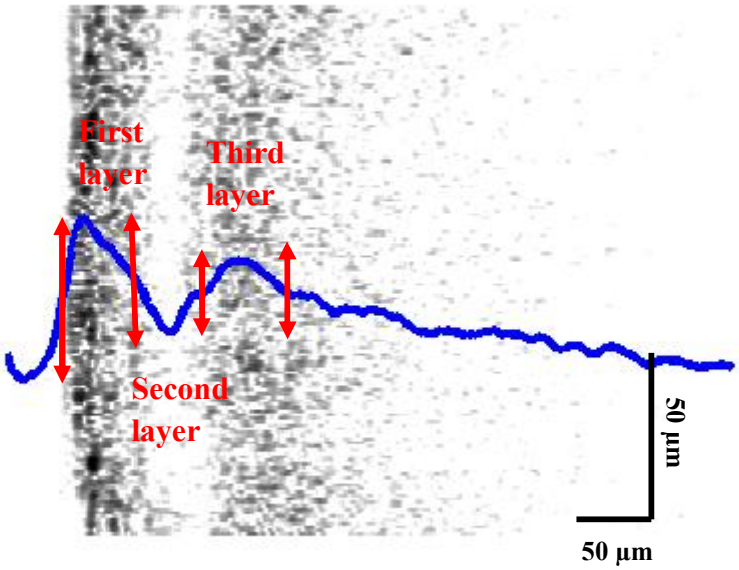

Figure 4.17 Mean profile of the centre 20 depth profiles of the first pellet of moving with 1 mm/s.

Degradation of axial and lateral resolution

Theoretically, axial resolution depends on the centre wavelength and bandwidth of the used light source. However, a single exposure of the spectrometer collects all the scattering from the moving area before the next exposure in the case of imaging a non-stationary object. Due to the curvature of the pellet surface, there is axial resolution degradation as shown in Fig. 4.18. If the distance between the imaged lateral pixel and the centre is L, the degradation can be expressed as:

$$\delta l = \sqrt{r^2 - L^2} - \sqrt{r^2 - (L + \delta x)^2} \quad (4.7)$$

where r is the diameter of the pellet, and ŭx is the lateral moving distance between adjacent exposures. Fig. 4.19 shows the degradation of axial resolution in relation to the position of the imaged lateral pixels when the moving speed is 5 mm/s.

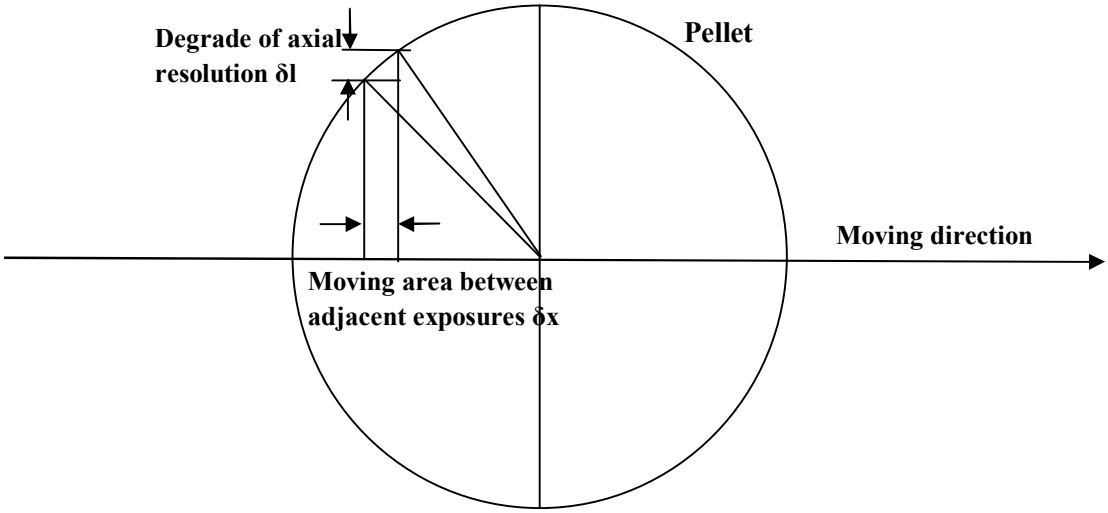

Figure 4.0.18 Schematic diagram of degradation of axial and lateral resolution.

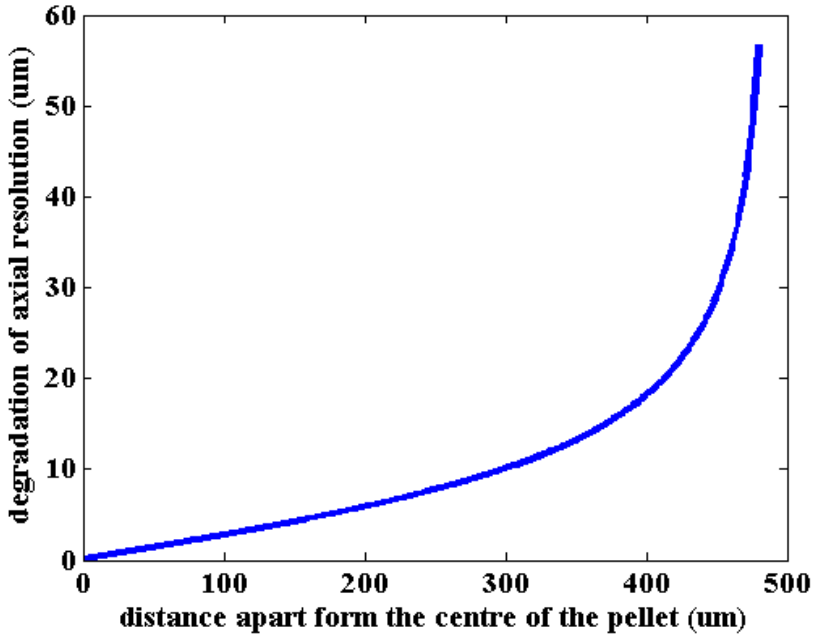

Figure 4.19 Degradation of axial resolution.

The axial resolution is degraded to 12 µm when the lateral pixel is located at 200 µm away from the centre. Hence the three coating layers are clearly visible in the centre area of the imaged pellet. But at the side of pellet, the coating layers are indistinct. The lateral resolution is degraded by ŭx which is bigger than 13 µm in this case. Due to the degradation of axial and lateral resolution, the air bubble indicated in Fig. 4.16 could not be identified if the moving speed increases to 20 mm/s. Hence, in order to image and evaluate the coating thickness of thin layer structure in the real-world coating processing unit, a spectrometer with high data acquisition speed will be required.

4.5 Summary

In this chapter, I demonstarted that the developed SD-OCT is an excellent PAT tool for the characterisation of the coating sturcture of pharmaceutical tablets and pellets.

The off-line measurements of tablet and pellet coating structures were performed using both single-point and single-shot SD-OCT systems. Firstly a batch of large size tablets with a single coating layer were imaged by using a single-point SD-OCT system. The resulting cross-sectional image for each tablet consists of 500 A-scan depth profiles, with an actual image size of 5×0.6 mm^2. We found that the coating layer of each tablet could be clearly distinguished in their cross-sectional images. The mean thickness determined was in the range of 30 µm to 220 µm. Secondly two of these tablets were measured using a single-shot SD-OCT system. Each single-shot measurement consists of 3200 mean A-scan depth profiles. The mean coating thickness were determined as 72 µm and 107 µm that are in good agreement with those obtained with the single-point SD-OCT configuration.

Off-line measurement of small size pellet samples were also performed by using single-point configuration. Unlike in the measurement on large tablets where a galvo mirror was used for lateral scanning, a translation stage was used to scan the pellet samples. This configuration is advantageous in that the small pellet sample is always at the centre of the lens thus scattered light could be collected more efficiently. Pellets of two different diameters were measured. It was found that the pellet of ~ 350 µm diameter only had one coating layer with a coating thickness of~ 90 µm. In contrast,

the pellet with a diameter of 850 µm exhibited two coating layers with thickness of 38 µm and 50 µm respectively.

In order to increase the data acuisition speed for on-line measurement, I studied the effect of reduced bit depth of the ADC on the measurement quality. It was found that the image quality is almost unchanged even when the bit depth of the ADC was reduced from 14 bits to 10 bits. By reducing the bit depth from 14 to 10 bits the data acquisition time could be reduced. A new customised spectrometer has been ordered which will allow a much high measurement speed of 40,000 spectra per second, ideal for online applications.

The on-line measurements of pellet coating were performed using a fibre based SD-OCT configration. Compared with the above-mentioned free space configurations, the fibre based configuration is advantagous due to its compactness and portability. The flexible sonsor head can be easily integarted into a pharmaceutical coator. Using the developed fibre-based SD-OCT system, it was demonstarted for the first time that the layer thicknesses of all three coating layers of a moving pellet can be quatified. However, a degradation of axial and lateral resolution was found when the small pellets were moving at high speed. This problem can be easily solved by using a high speed spectrometer.

References:

1. G.C. Cole, Introduction and overview of pharmaceutical coating, in: G. Cole, J. Hogan, A. Michael (Eds.), Pharmaceutical Coating Technology, Taylor & Francis Ltd, Philadelphia, 1995, pp. 1ï 5.
2. G.M. Jantzen, J.R. Robinson, Sustained and controlled-release drug delivery systems, In: G.S. Banker, C.T. Rhodes (Eds.), Modern pharmaceutics, Marcel Dekker, New York, 2002, pp. 501ï 528.
3. J.D. Perez-Ramos, W.P. Findlay, G. Peck, K.R. Morris, "Quantitative analysis of film coating in a pan coater based on in-line sensor measurements," AAPS PharmSciTech **6:** 127ï 136 (2005).
4. Y.C. Shen, P.F. Taday, "Development and application of terahertz pulsed imaging for non-destructive inspection of pharmaceutical tablet," IEEE J. Sel. Top. Quant. Electron. **14:** 407-415 (2008).
5. Y.C. Shen, "Terahertz pulsed spectroscopy and imaging for pharmaceutical applications: A review," Int. J. Pharm., **417**: 48-60 (2011).
6. Y.C. Shen and B.B. Jin, Terahertz applications in pharmaceutical industry and science, in: D. Saeedkia (Eds.), Handbook of Terahertz Technology for Imaging, Sensing and Communications, Woodhead Publishing Ltd, Cambridge, 2013,pp. 579-614.
7. J.A. Zeitler, Y.C. Shen, C. Baker, P.F. Taday, M. Pepper, T. Rades, "Analysis of coating structures and interfaces in solid oral dosage forms by three dimensional terahertz pulsed imaging," J. Pharm. Sci. **96**: 330ï 340 (2007).
8. S.C. Zhong, Y.C. Shen, L. Ho, R.K. May, J.A. Zeitler, M. Evens, P.F. Taday, M. Pepper, T. Rades, K.C. Gordon, R. Muller, P. Kleinebudde, "Non-destructive quantification of pharmaceutical tablet coatings using terahertz pulsed imaging and optical coherence tomography," Opt. Laser. Eng. **49**: 361-365 (2011).
9. S. Zhong, H. Shen, Y.C. Shen, J.A. Zeitler, M. Evans and P.T. Taday, ñNon-invasive 3D characterization using terahertz pulsed imaging and infrared optical coherence tomography,ò The 34th International Conference on Infrared, Millimetre, and Terahertz Waves (IRMMW-THz 2009), Bosan, Korea, September 21-25, (2009).

10. D.M. Koller, G. Hannesschlager, M. Leitner, J.G.Khinast, "Non-destructive analysis of tablet coatings with optical coherence tomography," Eur. J. Pharm. Sci. **44**: 142-148 (2011).
11. J.M. Mauritz, R.S. Morrisbv, R.S. Hutton, C.H. Legge, C.F. Kaminski, "Imaging pharmaceutical tablets with optical coherence tomography," J. Phar. Sci. **99**: 385-391 (2010).
12. C. Li, J.A. Zeitler, Y.Dong, Y.C. Shen, "Non-destructive evaluation of polymer coating structures on pharmaceutical pellets using full field optical coherence tomography," J. Pharm. Sci. (2013).
13. R.A. Leitgeb, C.K. Hitzenberger, A.F. Fercher, T. Bajraszewski, ñPhase-shifting algorithm to achieve high-speed by frequency-domain optical coherence tomography,ò Opt. Lett. **28**: 2201-2203 (2003).
14. BWTECK Inc., "Spectrometer knowledge," URL: http://bwtek.com/spectrometer-part-5-spectral-resolution/
15. R.A. Leitgeb, C.K. Hitzenberger, A.F. Fercher, "Performance of Fourier domain vs. time domain optical coherence tomography," Opt. Express **11**: 889-894 (2003).
16. Z. Yaqoob, J.Q. Wu, C.H. Yang, "Spectral domain optical coherence tomography: a better OCT imaging strategy," Bio. Techniques **39**: S6-S13 (2005).

Chapter 5 SD-OCT for medical application

5.1 Introduction

Fig. 5.1 shows a human eye structure. A human eye works like a camera. Light is firstly focused by the cornea which is the most front transparent surface of the eye. And then passes through the iris which is acts like a pupil in a camera. After that, the crystalline lens located behind the iris further focus the light. At last the light reaches retina which acts like an image sensor of a camera. The cornea contributes most of the eyeôs focusing power.

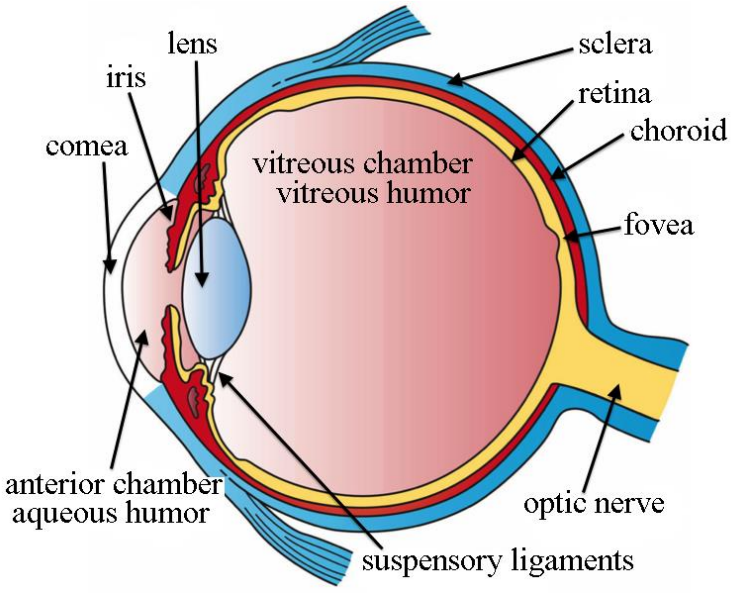

Figure 5.1 Human eye structure. (Holly Fischer, Jan 31st 2013, http://open.umich.edu/education/med/resources/second-look-series/materials)

The central corneal thickness (CCT) is an important parameter to in both diagnostic and therapeutic assessment of eye disease. It changes with the changes of intraocular pressure in the eye. Intraocular pressure is the fluid pressure in the eye that is important to evaluate the patients at risk of glaucoma. Hence, CCT can be used for

early diagnosis of glaucoma. Moreover, CCT can be used for planning keratorefractive surgical procedures [1-5]. To date, ultrasound pachymetry is the most commonly used tool for clinical evaluation of cornea thickness. However, the use of this technique is limited. Firstly, it is an invasive method as it requires its probe to come into contact with the patient's eye. Secondly, ultrasound pachymetry can measure only a single point. Finally, the resolution of the ultrasound pachymetry is several tens of micrometres. Therefore, many other high resolution and non-invasive imaging techniques including specular microscopy [6], confocal microscopy [7], scanning slit topography and OCT [8] have been studied for evaluating the CCT.

As the single-shot SD-OCT measurement acquires multiple row interferograms in parallel, it could assess corneal thickness without any motion artefacts. It has potential, therefore, to be a practical tool for real-time assessment of cornea thickness during surgical operations. It can also be used for early diagnosis of glaucoma in-vivo. In this study, an in-house single-shot SD-OCT was employed to image human and bovine cornea, and to investigate the corneal thickness dynamics in relation to three different perfusion pressures. For comparison, the corneal thickness was also measured by ultrasound pachymetry at each perfusion pressure.

5.2 Experiment

Five human and bovine corneas were prepared prior to the experiment. In brief, each cornea was mounted on the artificial chamber as shown in Fig. 5.2(a). Then the artificial chamber was then perfused with a balanced sterile saline solution. The pressure inside the chamber was firstly adjusted using a 500ml container of normal saline set at 50 cm in height relative to the mounted cornea. After an equilibrium time of 30 minutes the ultrasound measurement and OCT imaging started at the same pressure. For the human corneas, the epithelium layer was then removed with an eye sponge in order to take accurate ultrasound readings. For the bovine corneas, this was not performed as their thickness is well beyond the measurement range of the ultrasound pachymetry.

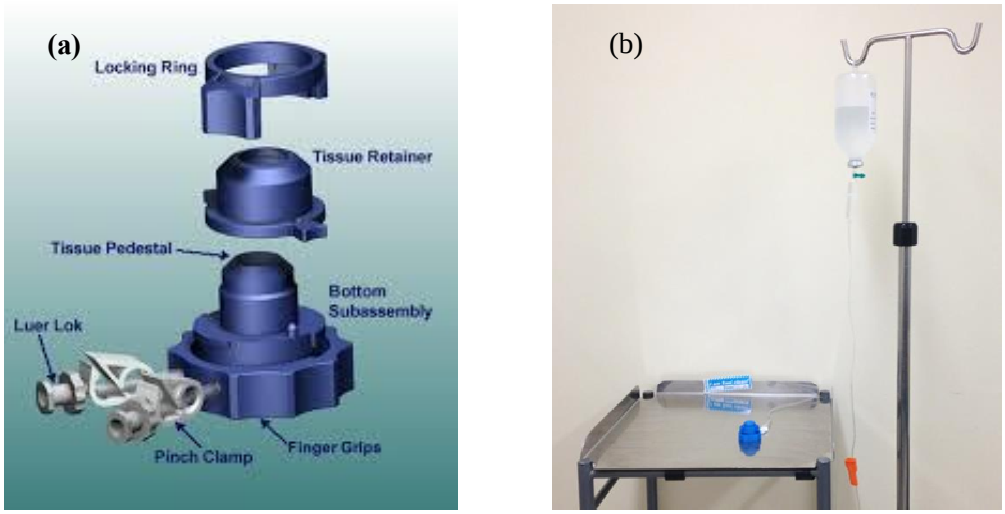

Figure 5.2 The perfused artificial anterior chamber system. (a) Artificial chamber for mounting the cornea. (Copyright © 2009 - Barron Precision Instruments, http://www.bpic.com/Instructions/aac-instr.htm) (b) The IV stand for adjusting the height of the solution container and perfused pressure.

Thirty minutes after mounting the sample, the thickness of the cornea was measured 8 times using ultrasound pachymetry (human cornea: SP 100, Tomey, Nagoya, Japan; bovine cornea: DGH55 Pachymeter, The DGH Technology, Exton, PA, USA) and then 15 OCT measurements were taken at intervals of 1 minute. A second set of ultrasound readings was taken subsequently at the same pressure. As soon as the perfusion pressure was raised to 100 cm of solution column pressure, another 15 OCT images were recorded at an intervals of 1 minute followed by the third set of ultrasound readings. The perfusion pressure was then increased from 100 cm to 150 cm of solution column pressure, and another 15 OCT images were recorded at 1 minute intervals each, followed by the fourth set of ultrasound readings. Fig. 5.2 (b) shows the IV stand used for adjusting the height of the solution container to adjust the perfusion pressure of the artificial chamber.

5.3 Mean corneal thickness

As described in Chapter 3, the pixel width of the used CMOS camera in the single-shot SD-OCT system is 6.5 εm. Since there was a magnification of 1.2 between the real sample and the camera grabbed imaging, the interval between adjacent lateral pixels on the real sample is 5.2 εm. In each camera exposure, the camera grabbed 500 interferograms in parallel which corresponds to around 2.5 mm width on the sample. In each OCT measurement, 50 images were taken with a frame rate of 33 fps for averaging. Hence the total time for a measurement was 1.5 s approximately. All the measurements were performed without using phase shift techniques. All the measured spectra were firstly interpolated from the wavelength domain to the wavenumber domain. Then the A-scan depth profiles were obtained by applying a FT to the interpolated spectra. Cross-sectional images were generated by multiple depth profiles.

5.3.1 Mean thickness of human cornea

Fig. 5.3 shows 9 cross-sectional images of a human cornea at 5 minutes, 10 minutes and 15 minutes under each perfusion solution pressure. The image size of each cross-sectional image is 2×1.2 mm^2 which consists of 400 A-scans. This shows that the human cornea was getting thinner and thinner with the increasing perfusion pressure.

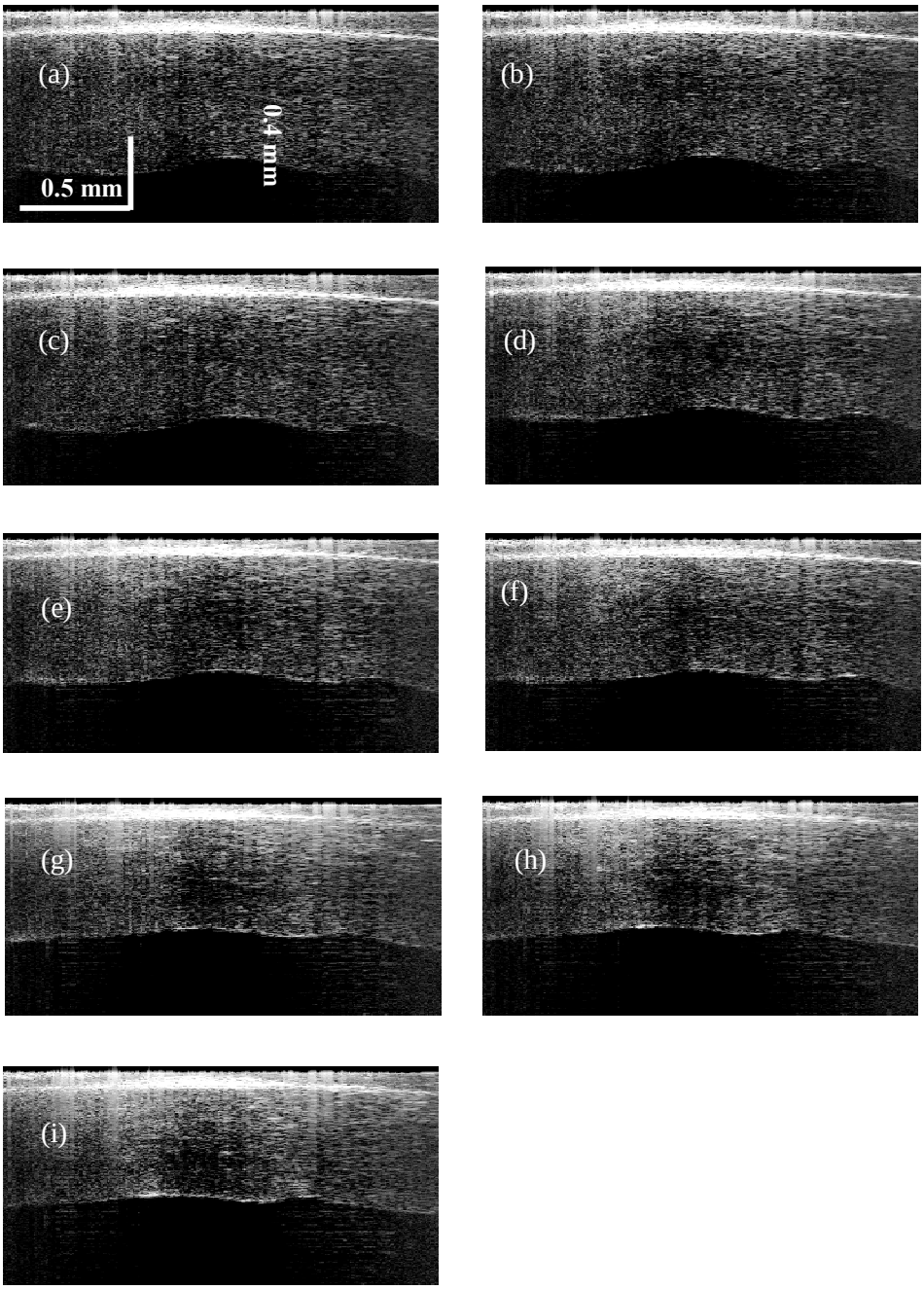

Figure 5.3Nine selected cross-sectional images of a human cornea at pressure of (a) – (c) 50 cm saline solution (d) – (f) 100 cm saline solution and (g) – (i) 150 cm saline solution. Each image contains 400 depth profiles and the size of each corneal image is 2×1.2 mm^2.

The mean thickness of each imaged human cornea was estimated by averaging 5 measurements at different locations on the cross-sectional image (centre, 50 pixels and 100 pixels left and right of the centre respectively). It is preformed manually by a single observer. Plots of the thickness measured at different time points and perfusion

pressure were produced to demonstrate the capability of the single-shot SD-OCT to image human corneas of different thicknesses. The ultrasound readings at four time points were compared with those measured by the OCT at their nearest time points.

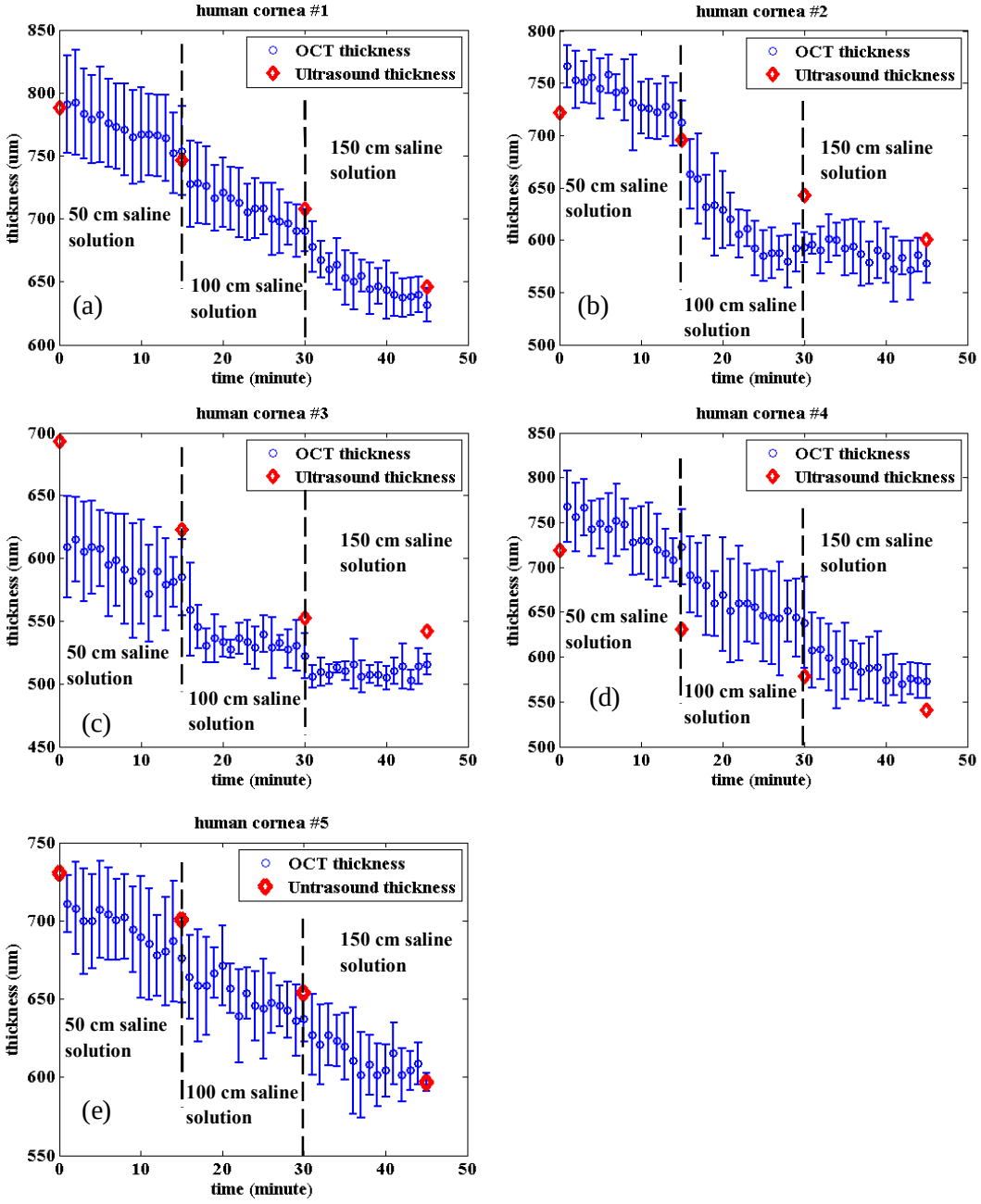

Figure 5.4 Mean corneal thickness of a human cornea at different time points and perfusion pressures. The blue circles in each plot are the mean thickness measured by the single-shot OCT and the read diamonds are the thicknesses determined by ultrasound readings. Both the thicknesses measured by the single-shot OCT and ultrasound decreased with the increasing of perfusion pressures.

Plots of mean corneal thicknesses of the 5 imaged human corneas were shown in Fig 5.4. The mean thickness tends to decrease in relation to the increasing measurement time and perfusion pressure. And finally, the mean thickness tended to stabilise. In total, the thickness of each cornea reduced by 100 ï 150 ε m.

5.3.2 Mean thickness of bovine cornea

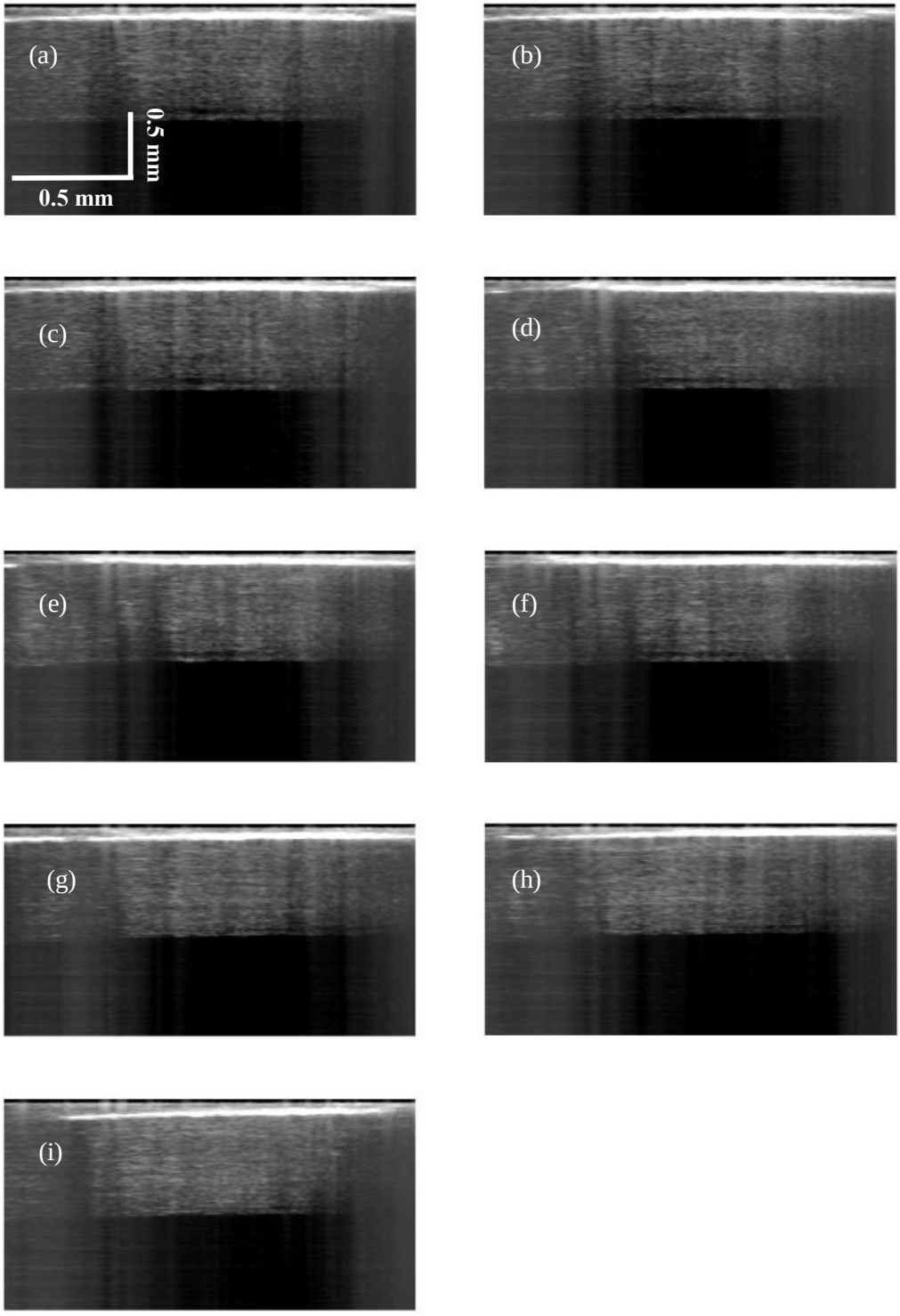

Figure 5.5 Nine cross-sectional image of a bovine cornea. at pressure of (a) – (c) 50 cm saline solution (d) – (f) 100 cm saline solution and (g) – (i) 150 cm saline solution. Each image contains 400 A-scans and the size of each corneal image is 2×2 mm^2.

Fig. 5.5 shows 9 cross-sectional images of a bovine cornea at 5 minutes, 10 minutes and 15 minutes under each perfusion solution pressure. The image size of each cross-sectional image is 2×2 mm^2 and consists of 400 A-scans, which is the same as the human corneal cross-sectional images shown in Fig. 5.3.

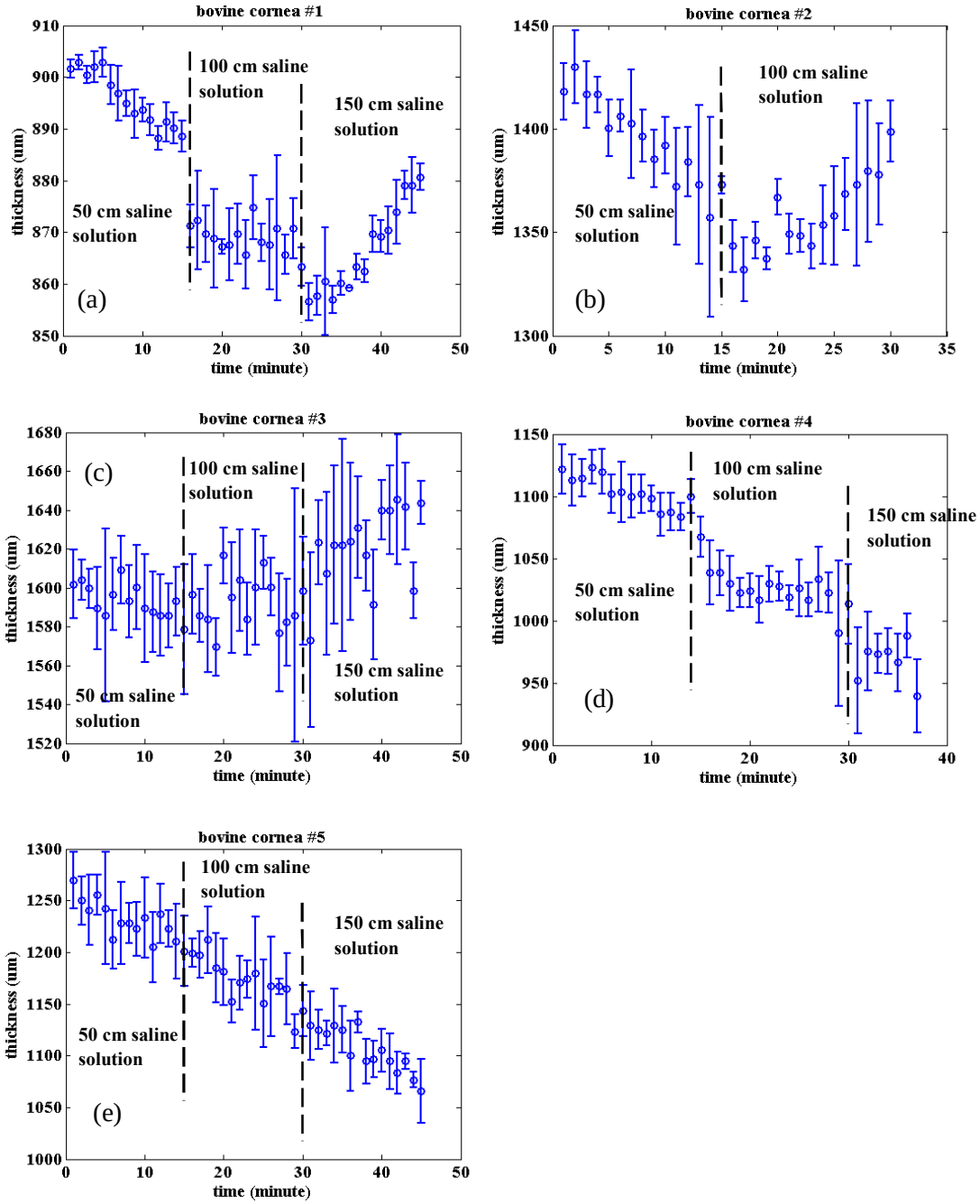

Figure 5.6 Mean corneal thickness of the 5 imaged bovine corneas at different time points and perfusion pressures. (a) – (c) Bovine samples were stored in saline solution overnight and measured in the second daytime. (d) and (e) Bovine samples were measured freshly.

The bovine samples were measured in two days. Two of five samples were measured freshly and three of them were stored in the saline solution overnight and measured in the second daytime. The overnight stored bovine corneas became too thick to measure with the ultrasound pachymetry. However, measurement was attempted and whenever there was a reading, it was recorded.

For the second cornea, the chamber leaked after the 100cm test; and for the fourth cornea, after 2 OCT measurements under 150 cm solution perfused pressure, the sample moved out of range. The first and fourth corneas ruptured during and after the tests under 150cm, respectively. The experiments on the fourth and fifth cornea tended to decrease in thickness. However, the change seemed abnormal in the other 3 corneas.

5.3.3 2-dimentional thickness dynamics map

Fig 5.7 shows one of the depth profiles at the centre of an imaged cornea. The blue one is the original depth profile; and the red one, from 500 μm to 1000 μm, is the depth profile that magnifies 5 times. Two distinct peaks, locates at the front and back surface of the imaged human cornea, are visible. The precise corneal thickness is the distance between the two peaks.

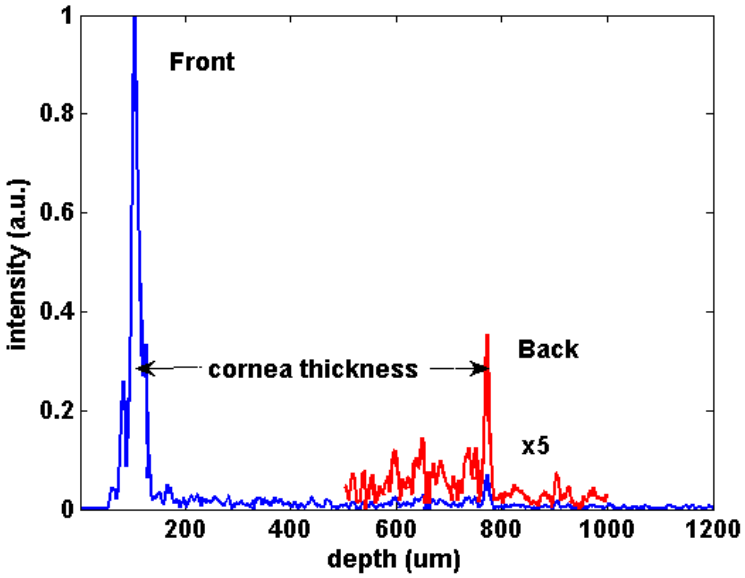

Figure 5.7 One of the SD-OCT depth profiles of human cornea. The blue peak is the front surface of human cornea and the red peak is the back surface of human cornea. The distance between the two peaks is the cornea thickness.

Unlike ultrasound pachymetry, OCT gives hundreds corneal thickness at all imaged lateral pixels. The centre 300 depth profiles of all the cross-sectional images were selected to pick up the surface peaks in order to evaluate the corneal thickness along the lateral direction. Fig. 5.8 (a) shows the positions of all 300 selected front and back surface peaks in one of the cross-sectional human cornea images. The corneal thicknesses of all lateral pixels are shown in Fig. 5.8(b). The computed corneal thicknesses at different imaging time points are shown on a thickness map in Fig. 5.9 (a); and the thickness reduction map is presented in Fig. 5.9 (b). It is shown that the corneal thickness reduced a minimum of 66 µm and a maximum of 220 µm. The single-shot SD-OCT is able to monitor the thickness reduction of all the lateral pixels, whereas the ultrasound pachymetry measures only the thickness of one pixel.

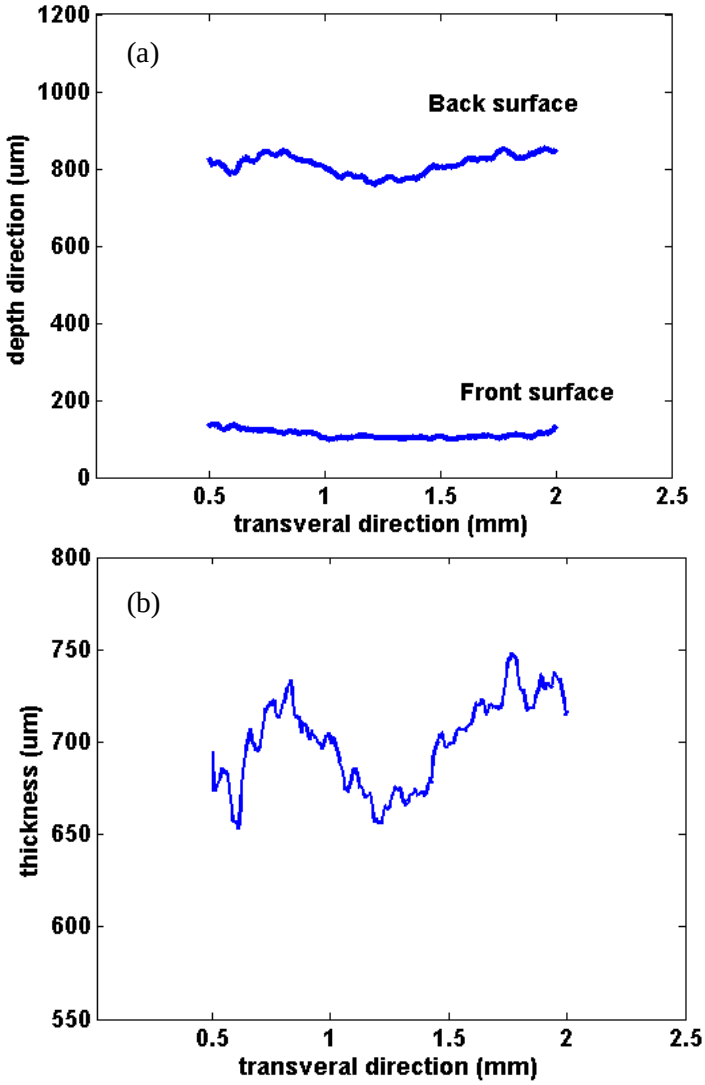

Figure 5.8 (a) Front and back surface extracted from one of the human cornea cross-sectional images. (b) Thickness distribution along transversal direction.

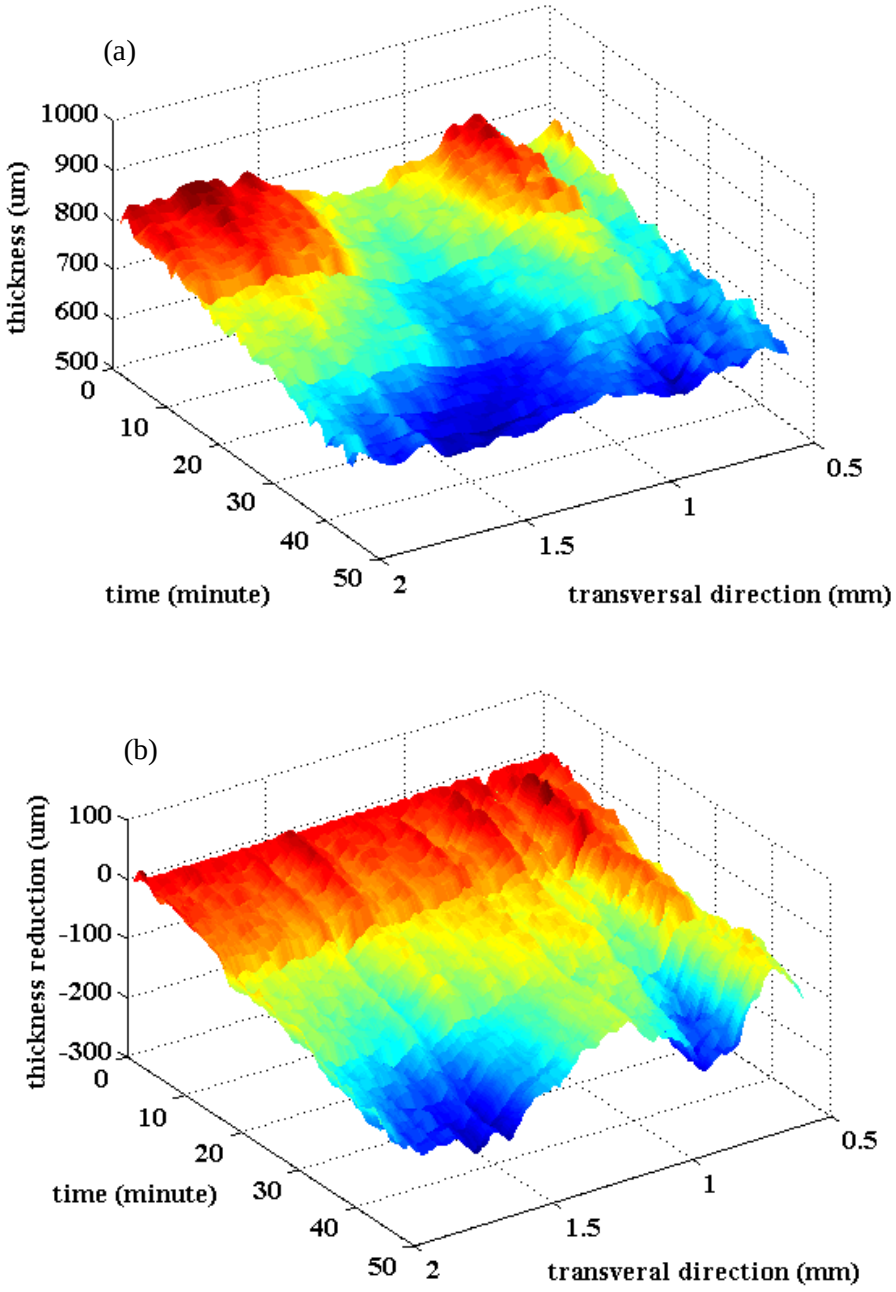

Figure 5.9(a) Thickness map in relation to the imaging time of one human cornea. (b) Thickness reduction of the human cornea relating to the imaging time.

5.4 Cornea dynamic at nanometre scale

5.4.1 Spectral domain phase microscopy

Phase information in interferometric based optical imaging allows the assessment of sub-wavelength variations or surface profiles relative to the position of a reference mirror. Over the past decades, several phase sensitive techniques including spectral domain phase microscopy (SDPM) [9] and spectral domain optical coherence phase microscopy (SD-OCPM) [10] which are based on SD-OCT have been developed to study the motion of individual biological molecules, single cell dynamics [11] and cell surface profiles [12]. In this study, the SDPM was firstly used to demonstrate the 2-D nanometre dynamics of two surfaces simultaneously.

In SDPM, the spectral interferogram due to the OPD is detected by spectrometer and the phase information is extracted from the complex depth profile which is obtained by FT of the spectral interferogram. Since the phase oscillates $2\acute{}$ rad at every shift of half centre wavelength of OPD, a phase retrieval method is required in order to exceed the limited OPD measurement range due to the $2\acute{}$ ambiguity [13]. However, for them to work correctly, phase unwrap methods require the phase to vary gradually. Instead of phase retrieval in depth domain, phase retrieval methods in spectral domain were proposed in order to increase the measurement range [14-18].

Typically, a standard SDPM employs the common path configuration [9] in order to have higher phase stability as this improves the SNR and measurement sensitivity of the SDPM. However, the common path configuration would compromise the spatial resolution by using a low NA objective lens and diminished phase changes due to sample. Therefore, the self-referencing method [12] performed on the single-shot SD-OCT was proposed in order to improve phase stability in the conventional dual path SD-OCT configuration.

5.4.2 Principles of SDPM

In SD-OCT, with the assumption that reference reflectivity is much larger than sample reflectivity ($R_r >> R_s$), the autocorrelation term which stands for the sample

mutual interference can be neglected. Therefore, after subtracting the DC term, the spectral interferogram detected by the spectrometer could be expressed as:

$$I(k) = S(k)[\sum \overline{R_s R_r} \cos(2nkd) \tag{5.1}$$

where k is the discrete wavenumber, S(k) is the spectral power density of light source and k_0 is the centre wavenumber of the light source; R_s and R_r represent the reflectivity of sample tissue and reference reflector respectively; d represents the OPD between reference mirror and sample tissue and n is the average refractive index of the sample. In this mathematical model, only a single reflector is considered. By applying the FT to the spectral interferogram and omitting the negative mirror terms, the positive A-scan complex depth signal will be obtained:

$$I(d) = (\overline{R_s R_r} \tilde{u} d - d_s) \exp(-j2k_0 n(d - d_s)) \tag{5.2}$$

where ũ denotes the convolution between light source autocorrelation and Dirac delta function ŭ. Ideally, a distinct peak value locates at d_0, namely the position of the single reflector in respect to reference reflector, should be found in the amplitude response of the complex depth signal. However, the depth signal is discretely sampled. There is a deviation between the visualised and the actual peak position. The visualised peak position and deviation is denoted as qpd and ŭd respectively. The phase information ű at the qpd can be used to evaluate the deviation ŭd.

$$\varphi(\Delta d) = -4k_0 n[\Delta d - (\Delta d + \delta d)] \tag{5.3}$$

$$\delta d = \frac{\varphi(\Delta)}{\partial\partial_0} \tag{5.4}$$

Then an exact OPD will be obtained:

$$d_s = \Delta d + \delta d \tag{5.5}$$

Meanwhile, the phase information can also be used to quantify the sub wavelength dynamics of the sample reflector:

$$\varphi(\Delta d, t_2) - \varphi(\Delta d, t_1) = 4k_0 n[\delta d(t_2) - \delta d(t_1)] \tag{5.6}$$

$$\delta d(t_2) - \delta d(t_1) = \frac{\varphi(\Delta, t_2) - \varphi(\Delta, t_1)}{\partial\partial_0} \tag{5.7}$$

5.4.3 Phase stability

In the experiment, a single-shot SD-OCT was employed to study the thickness dynamics of human cornea. Hence, it was possible to use the self-referencing method to reject the common mode noise [12]. The separate reference arm would suffer from random phase noise due to the independent mechanical and thermal fluctuations as shown in Fig. 5.10 (a). As the single-shot SD-OCT system acquires multiple spectral interferograms with the same phase fluctuations at the same time. Hence all the simultaneously grabbed A-scans have the same mechanical and thermal fluctuations. The phase noise resulting from the mechanical and thermal fluctuations will be reduced by subtracting a reference phase from one of the interferograms in the same exposure. Fig. 5.10 (b) shows the phase information after subtraction of the reference phase.

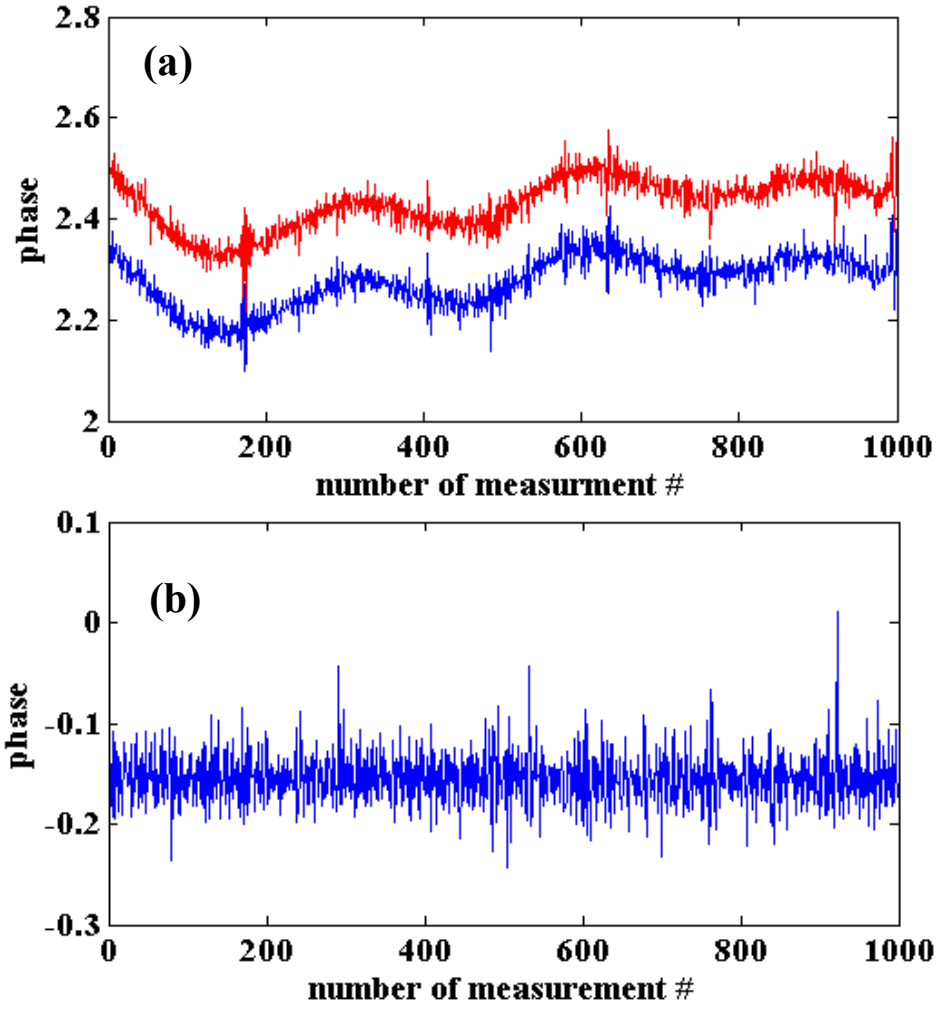

Figure 5.10 (a) Phase information extracted from two of the complex depth profiles in the same exposure. They have the same phase noise due to the same mechanical and thermal fluctuations. (b) Phase information obtained by self-referencing.

To evaluate the phase stability of the system, a stationary glass slide was placed in the sample arm. One thousand A-scans were taken in a single exposure. Applying self-referencing, the phase variance distribution is shown in Fig. 5.11. The phase stability defined as the standard deviation of the phase variance distribution is 0.025 rad. This leads to a minimum detectable OPD of 0.8 nm.

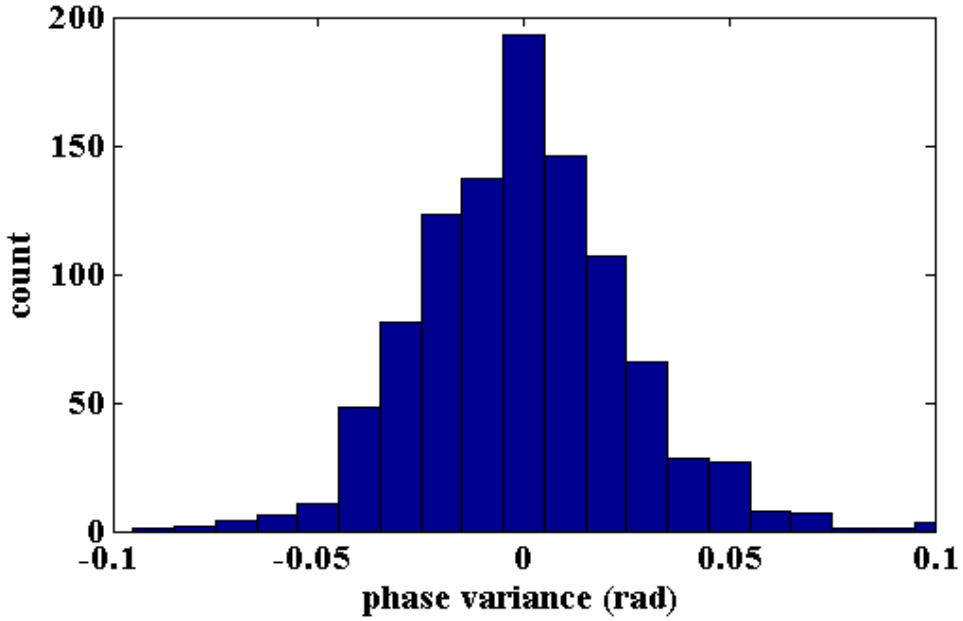

Figure 5.11Phase variance distribution.

The glass slide was then mounted on a PZT actuator to show the capability of the SDPM to monitor nanometre scale vibration. A sinusoidal waveform with a frequency of 5 Hz was generated by a function generator to drive the PZT actuator. The camera array grabbed 100 spectral interferograms in parallel and the acquisition speed was 200 fps. In the practical measurement, the system grabbed 200 frames. After performing the data interpolation, FT, phase unwrap and self-referencing, the vibration map was obtained, as shown in Fig. 5.12, which shows the glass slide vibration in a sinusoidal waveform. The measured amplitude and frequency were 291 nm and 5 Hz respectively, which conformed to the generated sinusoidal waveform.

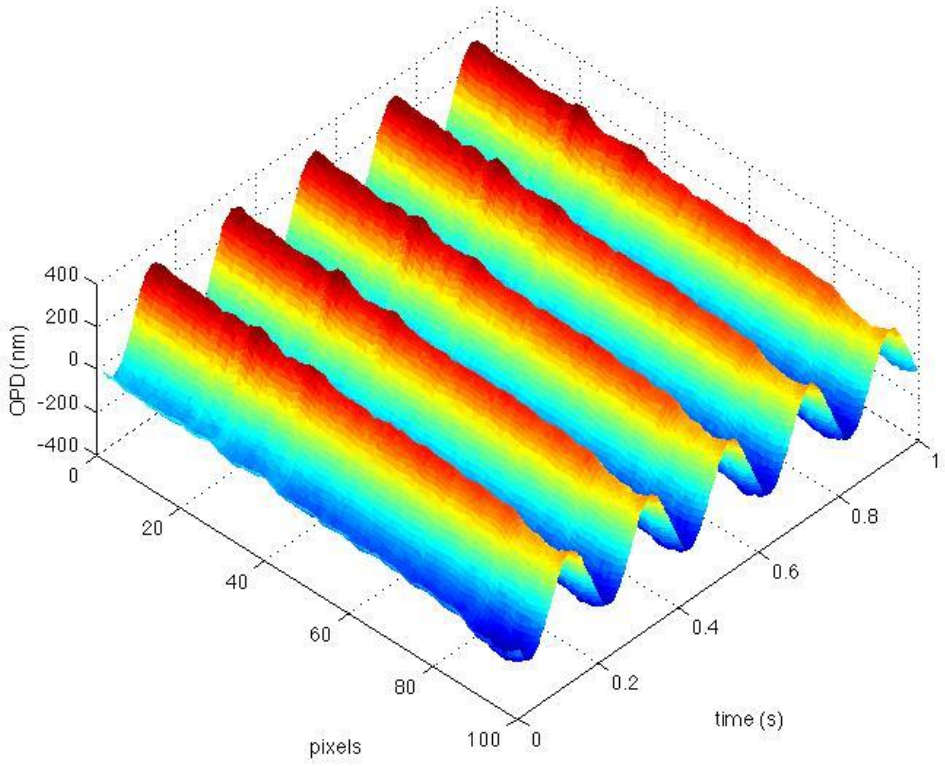

Figure 5.12 Vibration map of a glass slide. The frequency is 5Hz and the amplitude is 291 nm.

5.4.4 Monitoring the nanoscale dynamics of a human cornea

As mentioned, 50 successive spectral interferogram frames were grabbed in 1.3s. The SDPM was used to evaluate the nanoscale dynamics of the front and back surface in a short time. The time dependent phase information was extracted by taking the arguments at the front and back surface peaks in the Fourier Transformed complex A-scan depth signal. After applying self-referencing, the relative time dependent movement of the front and back surface can be calculate using Eq. (5.7). Fig. 5.13(a) shows nanoscale movement of the front and back surface at the centre of the imaged human cornea. The front surface moved forward 128 nm, and the back surface moved forward 216 nm. Hence, the thickness at this lateral pixel reduced by about 88 nm. Furthermore, the phase information of central 100 depth profiles was extracted to generate the movement map shown in Fig. 5.13 (b).

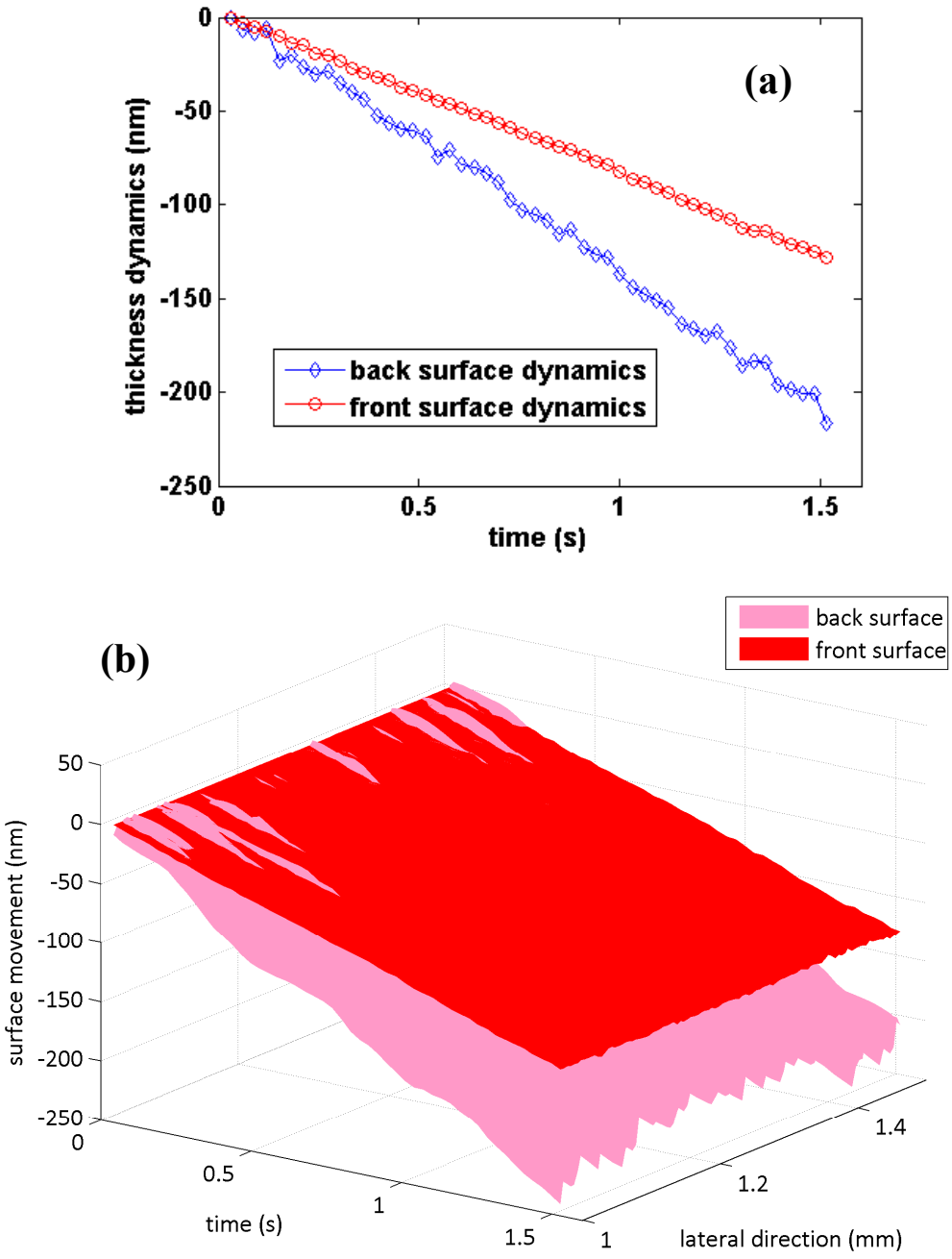

Figure 5.13 (a) Movement of front and back surfaces at the central pixel of the imaged human cornea. (b) Movement map of the front and back surface of the central 100 lateral pixels. The front surface moved forward 128 nm and the back surface moved forward 216 nm. Hence the total thickness decreased 88 nm.

5.5 Summary

In this chapter, the thickness dynamics of both the human and bovine cornea under different perfusion pressures were investigated using an in-house single-shot SD-OCT system. Initially, the mean thicknesses of human and bovine corneas were evaluated to characterise the trend of the corneal thickness in relation to measurement time under different perfusion pressures. The thickness of the human cornea tended to reduce with the increase of perfusion pressure in a range of 100-150 μm. For bovine corneas, two showed a nice trend of decreasing thickness while the other three appeared to become abnormal in thickness. The thickness map and the thickness reduction map were then generated, showing the time dependent thickness and thickness changes of all the central 300 lateral pixels of one imaged human cornea. Finally, the SDPM were used to evaluate the nanometre scale movement of the front and back surfaces and thickness changes over a short time.

References:

1. R.C. Wolfs, C.C. Klaver, J.R. Vingerling, D.E. Grobbee, A. Hofman, P.T. deJong, ñDistribution of central corneal thickness and its association with intraocular pressure: the Rotterdam Study.ò Am J Ophthalmol **123**:767ï 72 (1997).
2. L.W. Herndon, S.A. Choudhri, T. Cox, K.F. Damji, M.B. Shields, R.R. Allingham, ñCentral corneal thickness in normal, glaucomatous, and ocular hypertensive eyes.ò Arch Ophthalmol **115**:1137ï 41 (1997).
3. W.A. Argus, ñOcular hypertension and central corneal thickness.ò Ophthalmology **102**:1810ï 2 (1995).
4. F.A. Medeiros, P.A. Sample, L.N. Zangwill, C. Bowd, M. Aihara, R.N. Weinreb, ñCorneal thickness as a risk factor for visual field loss in patients with preperimetric glaucomatous optic neuropathy,ò Am J Ophthalmol **136**:805ï 13 (2003).
5. F.A. Medeiros, P.A. Sample, R.N. Weinreb, ñCorneal thickness measurements and visual function abnormalities in ocular hypertensive patients,ò Am J Ophthalmol **135**:131ï 7 (2003).
6. L.J. Módis, A. Langenbucher, B. Seitz, ñCorneal endothelial cell density and pachymetry measured by contact and noncontact specular microscopy.ò J Cataract Refract Surg **28**: 1763ï 1769 (2002).
7. B.R. Masters, G. Kino, Confocal microscopy of the eye. In: Masters BR, ed. Non-invasive Diagnostic Techniques in Ophthalmology. New York, NY: Springer-Verlag NY Inc, 1990: 152ï 71.
8. Y. Feng, T.L. Simpson, ñComparison of human central cornea and limbus in vivo using optical coherence tomography.ò Optom Vis Sci **82**: 416ï 9 (2005).
9. M. A. Choma, A. K. Ellerbee, C. H. Yang, T. L. Creazzo, and J. A. Izatt, ñSpectral-domain phase microscopy,ò Opt. Lett. **30**: 1162ï 1164 (2005).
10. C. Joo, T. Akkin, B. Cense, B. H. Park, and J. F. de Boer, ñSpectral-domain optical coherence phase microscopy for quantitative phase-contrast imaging,ò Opt. Lett. **30**: 2131ï 2133 (2005).
11. A.K. Ellerbee, T.L. Creazzo, and J.A. Izatt, ñInvestigating nanoscale cellular dynamics with cross-sectional spectral domain phase microscopy,ò Opt. Express **15**: 8115-8124 (2007).

12. Z. Yaqoob, W. Choi, S.Oh, N. Lue, Y. Park, C. Fang-Yen, R.R. Dasari, K. Badizadegan, and M.S. Feld, ñImproved phase sensitivity in spectral domain phase microscopy using line-field illumination and self-phase reference,ò Opt. Express **17**: 10681-10687 (2009).
13. H. C. Hendargo, M. Zhao, N. Shepherd, and J. A. Izatt, ñSynthetic wavelength based phase unwrapping in spectral domain optical coherence tomography,ò Opt. Express **17**: 5039ï 5051 (2009).
14. J. Zhang, B. Rao, L. Yu, and Z. Chen, ñHigh-dynamic-range quantitative phase imaging with spectral domain phase microscopy,ò Opt. Lett. **34**: 3442ï 3444 (2009).
15. D. Moore and R. R. McLeod, ñPhase-sensitive swept-source interferometry for absolute ranging with application to measurements of group refractive index and thickness,ò Opt. Express **19**: 8117ï 8126 (2011).
16. Y. Zhu, N. T. Shaked, L. L. Satterwhite, and A. Wax, ñSpectral-domain differential interference contrast microscopy,ò Opt. Lett. **36**: 430ï 432 (2011).
17. C. Wang, Z. H. Ding, S. T. Mei, H. Yu, W. Hong, Y. Z. Yan, and W. D. Shen, ñUltralong-range phase imaging with orthogonal dispersive spectral-domain optical coherence tomography,ò Opt. Lett. **37**: 4555ï 4557 (2012).

Chapter 6 Algebraic reconstruction technique based optical coherence tomography

6.1 Introduction

In a SD-OCT system, a spectrometer with a fixed number of pixels is used to acquire spectral interferogram in the wavelength domain. The depth profile of a sample is subsequently obtained from the measured spectral interferogram by fast Fourier transform (FFT). The imaging depth is determined by the spectral resolution of the used spectrometer, and a high-resolution spectrometer is thus required in order to achieve sufficiently large imaging depth. On the other hand, the spectrometer also has to be broadband in order to achieve high axial resolution. Therefore, there is an ultimate trade-off between the axial resolution and the imaging depth because high resolution and broadband spectral range cannot always be achieved simultaneously for a given spectrometer that has a fixed number of sensor elements [1].

Very recently Seck et al. [2, 3] proposed an algebraic reconstruction technique (ART) that allows high axial resolution and large imaging depth to be achieved simultaneously. More importantly, the ART-OCT method could possibly reduce significantly the data acquisition time and volume, because it requires fewer measurement points than is conventionally required, in a similar way as the recently developed compressive sensing (CS) technology [1, 4-11]. In this chapter, we present a thorough experimental and theoretical investigation by applying the ART-OCT for characterising real-world samples.

In this work, the OCT cross-sectional images were reconstructed using the sparse approximation method with a fraction of measurement interferogram data points. In addition, a greedy sparse approximation method, namely Orthogonal Matching Pursuit (OMP), was proposed for image reconstruction. It has been demonstrated that only 30% of measurement data is sufficient in order to reconstruct the OCT cross-sectional image. Moreover, the proposed OMP method is found to be about 60 times faster than the L1-optimisation method used in [2, 3]. Furthermore, it is found that the proposed OMP method, when combined with a spectrum split approach [12], provides an improvement of 3.7 dB in SNR

6.2 OCT image reconstruction

6.2.1 SD-OCT

The spectral interferogram grabbed by the spectrometer at the exit of the interferometer is the superposition of the reflected/backscattered reference and sample light beam. After removing DC and autocorrelation terms [13], the interferogram can be expressed as:

$$I(\lambda) = \int_{-\infty}^{+\infty} \sqrt{R_r R_s}\, S(\lambda) \cos(4\pi z / \lambda) dz \tag{6.1}$$

Where ∂ is the wavelength, I(∂) is the interferogram, R_r and R_s are the reflectivity of reference reflector and sample respectively, S(∂) is the spectral power density of the light source and z is the OPD between reference and sample. In SD-OCT the FT is applied to the differential interferogram to extract the depth profile of a sample; and the differential interferogram has to be interpolated from the wavelength domain to the wavenumber domain before the FT.

According to the Shannon-Nyquist sampling theorem [1], the number of sensor pixels K in the wavenumber domain is correlated with the maximum imaging depth z_{max} and spectral bandwidth φk.

$$K \geq z_{max} \varphi k / \pi \tag{6.2}$$

As spectral bandwidth ∆k is inversely proportional to the axial resolution, $\Delta z = \frac{2\ln 2}{\pi} \cdot \frac{\lambda_0^2}{\Delta\lambda}$, the maximum imaging depth and the axial resolution cannot be improved simultaneously.

6.2.2 ART-OCT

The aim of ART-OCT is to reconstruct the depth profile by applying the sparse approximation method on the randomly resampled interferogram. It requires fewer interferogram data points to recover the depth profile compared with the conventionally used FT. The random resampled interferogram **I** can be expressed in a matrix form:

$$\mathbf{I}_{N\times 1} = \mathbf{\Phi}_{N\times M} \cdot \mathbf{R}_{M\times 1} \tag{6.3}$$

where **I** is the interferogram in wavelength domain, **R** is a sparse representation of the depth profile in depth domain:

$$\mathbf{I} = \begin{pmatrix} i(\lambda_1) \\ i(\lambda_2) \\ \vdots \\ i(\lambda_N) \end{pmatrix}, \quad \mathbf{R} = \begin{pmatrix} r(d_1) \\ r(d_2) \\ \vdots \\ r(d_M) \end{pmatrix} \tag{6.4}$$

and **Φ** is the sampling operator determining which data points are selected for reconstruction

$$\mathbf{\Phi} = \begin{pmatrix} S(\lambda_1)\cos\left(\frac{4\pi d_1}{\lambda_1}\right) & S(\lambda_1)\cos\left(\frac{4\pi d_2}{\lambda_1}\right) & \cdots & S(\lambda_1)\cos\left(\frac{4\pi d_M}{\lambda_1}\right) \\ S(\lambda_2)\cos\left(\frac{4\pi d_1}{\lambda_2}\right) & S(\lambda_2)\cos\left(\frac{4\pi d_2}{\lambda_2}\right) & \cdots & S(\lambda_2)\cos\left(\frac{4\pi d_M}{\lambda_2}\right) \\ \vdots & \vdots & & \vdots \\ S(\lambda_N)\cos\left(\frac{4\pi d_1}{\lambda_N}\right) & S(\lambda_N)\cos\left(\frac{4\pi d_2}{\lambda_N}\right) & \cdots & S(\lambda_N)\cos\left(\frac{4\pi d_M}{\lambda_N}\right) \end{pmatrix} \tag{6.5}$$

N is the number of selected interferogram data points in the wavelength domain and M is the number of sub-surfaces of concern in the depth domain.

6.2.3 Sparse approximation algorithm in ART-OCT to recover depth profile

Basically, the sparse depth profile can be recovered by solving an optimisation problem of L_0 norm:

$$\min\|\cdot\|_0 \quad \text{subject to} \quad \Phi\cdot = \cdot \tag{6.6}$$

where the notation $\|\cdot\|_0$ is the L_0 of a vector measured by the number of non-zero elements in the vector. However, the l_0 norm is non-convex and difficult to solve, thus many other optimisation algorithms including L_1-optimisation [14], OMP [15], and total variation minimisation (TV-min) [16], were developed to replace the L_0 optimisation stated in Eq. (6.6).

A. L_1-minimisation

In the previous work, Seck et al. [2, 3] used the L_1-optimisation algorithm. Considering the noisy measurement in practice, they perform a mixed L_1/L_2 -optimisation to recover the depth profile:

$$\min\|\cdot\|_0 \quad \text{subject to} \quad \|\Phi\cdot - \cdot\|_0 < \cdot \tag{6.7}$$

where $\|\cdot\|_0$ represents the L_1 norm of a vector which is the sum of the absolute value of all the vector elements.

B. OMP

The L_1-optimisation proposed in Seck's work is very time consuming. Here the greedy sparse approximation method OMP, which provides a much faster reconstruction speed, was proposed to reconstruct OCT depth profiles. The idea of the OMP algorithm is to pick the column of $\mathbf{\Phi}$ which most correlates with the residual of

I in greedy iterations [15]. At first, the residual $\mathbf{r}_0$ is initialised as the resampled differential interferogram **I**. In the k-th iteration, the index of non-zero element is selected by a maximisation problem expressed as

$$\varphi_k = \arg\max_{i=1,2,\ldots,N} | \mathbf{\Phi}_i^T \mathbf{r}_{k-1} | \tag{6.8}$$

where φ_k is the selected index, $\mathbf{\Phi}_i^T$ is the transpose of the i-th column in $\mathbf{\Phi}$, and $\mathbf{r}_{k-1}$ is the residual of interferogram calculated in the previous iteration. The index set $\mathbf{\Gamma}_k$ of non-zeros elements is updated as

$$\mathbf{\Gamma}_k = \mathbf{\Gamma}_{k-1} \cup \varphi_k \tag{6.9}$$

The current residual $\mathbf{r}_k$ that will be used in the next iteration can be found as

$$\mathbf{r}_k = \mathbf{I} - \mathbf{\Phi}_{\mathbf{\Gamma}_k} \mathbf{\Phi}_{\mathbf{\Gamma}_k}^{+} \mathbf{I} \tag{6.10}$$

where $\mathbf{\Phi}_{\mathbf{\Gamma}_k}$ stands for the selected subsets of matrix $\mathbf{\Phi}$, and $\mathbf{\Phi}_{\mathbf{\Gamma}_k}^{+}$ is its Moore-Penrose pseudo inverse matrix. $\mathbf{\Phi}_{\mathbf{\Gamma}_k} \mathbf{\Phi}_{\mathbf{\Gamma}_k}^{+} \mathbf{I}$ is the closest approximation of the differential interferogram. The iteration will stop when all the indices of non-zeros elements in depth profile are selected. Finally the reconstructed depth profile is determined as:

$$\mathbf{R} = \mathbf{\Phi}_{\mathbf{\Gamma}}^{+} \mathbf{I} \tag{6.11}$$

6.3 Performance of the algorithm

6.3.1 Reconstructed depth profile

To characterise the performance of the proposed OMP algorithm, the interferograms of a standard coverslip were measured by the single-point SD-OCT system equipped with a spectrometer with 3648 pixels and 0.5 nm spectral resolution. Fig. 6.1(a) shows the differential interferogram of the standard 150 εm coverslip. To recover the depth profile by the proposed OMP algorithm, the sparsity level of the depth profile should be predefined. Since the measured coverslip has only two surfaces, the number of scattering (sparsity level of the depth profile) was set as 2 in this case. The depth coordinates was set from 0 εm to 450 εm, with a step size of 1.5εm in air, corresponding to 0 - 300 εm with a step size of 1 εm in coverslip if the refractive

index of the cover slip is 1.5. The depth profile of the coverslip reconstructed by OMP with all the measured interferogram data points is shown in Fig. 6.1(b). For comparison, the depth profile reconstructed by L1-optimisation [17] with the same number of data points and reconstruction settings is shown in Fig. 6.1(c). In addition, the depth profile obtained by FT is shown in Fig. 6.1(d) as a reference. Both the proposed OMP method and the widely used L1-optimization method succeed in recovering the top and bottom features. However, the intensity of bottom surface peak in the OMP depth profile is relatively enhanced compared with the L1-optimisation.

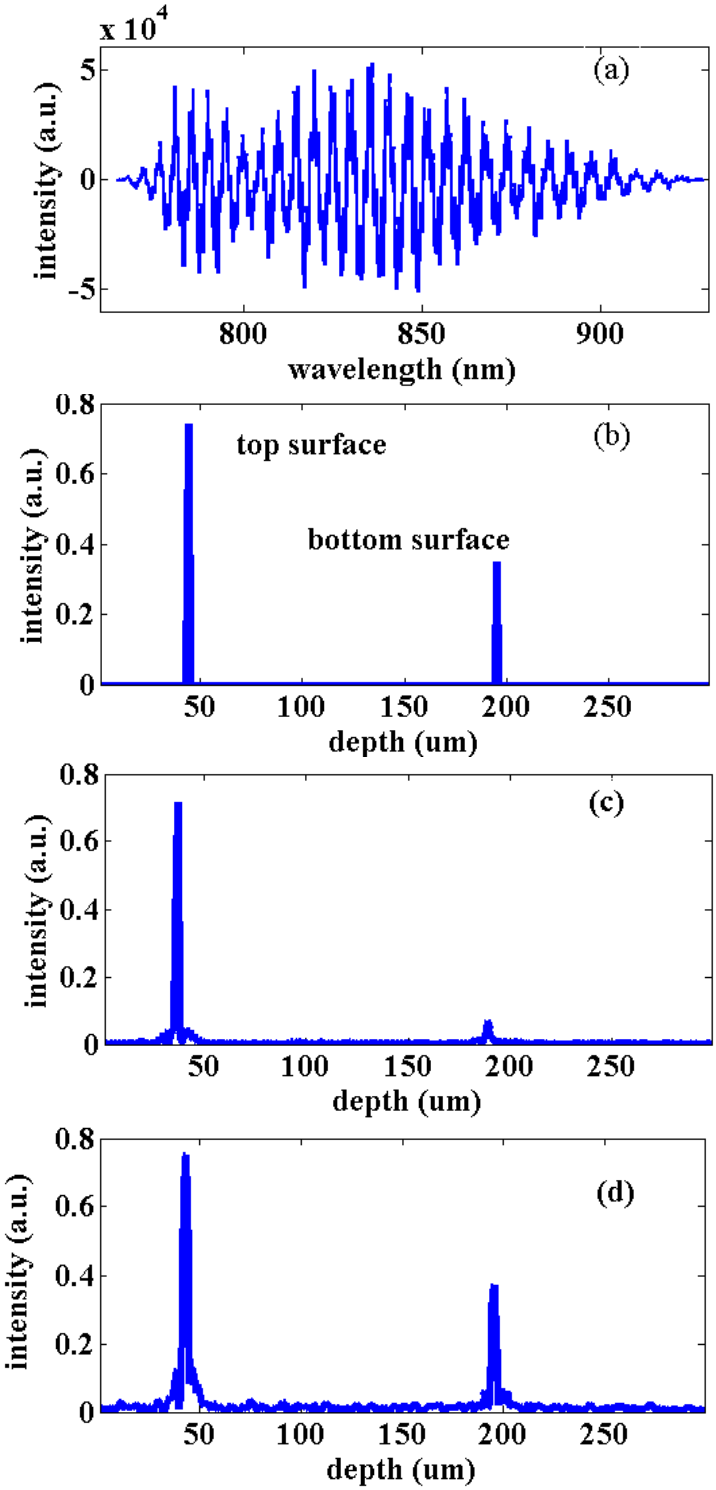

Figure 6.1 (a) Differential interferogram of an 150 μm coverslip. The depth profiles reconstructed by (b) the proposed OMP algorithm, (c) L1-optimisation, (c) Fourier tranform.

6.3.2 Sampling rate

A sparse approximation algorithm requires only a fraction of data points for depth profile reconstruction. The depth profile of the coverslip reconstructed by uniform random selected 60%, 30%, 20%, 10%, and 5% of differential interferogram data points is shown in Fig. 6.2. This shows an excellent reconstruction performance by the OMP algorithm, with only 5% of measurement data points.

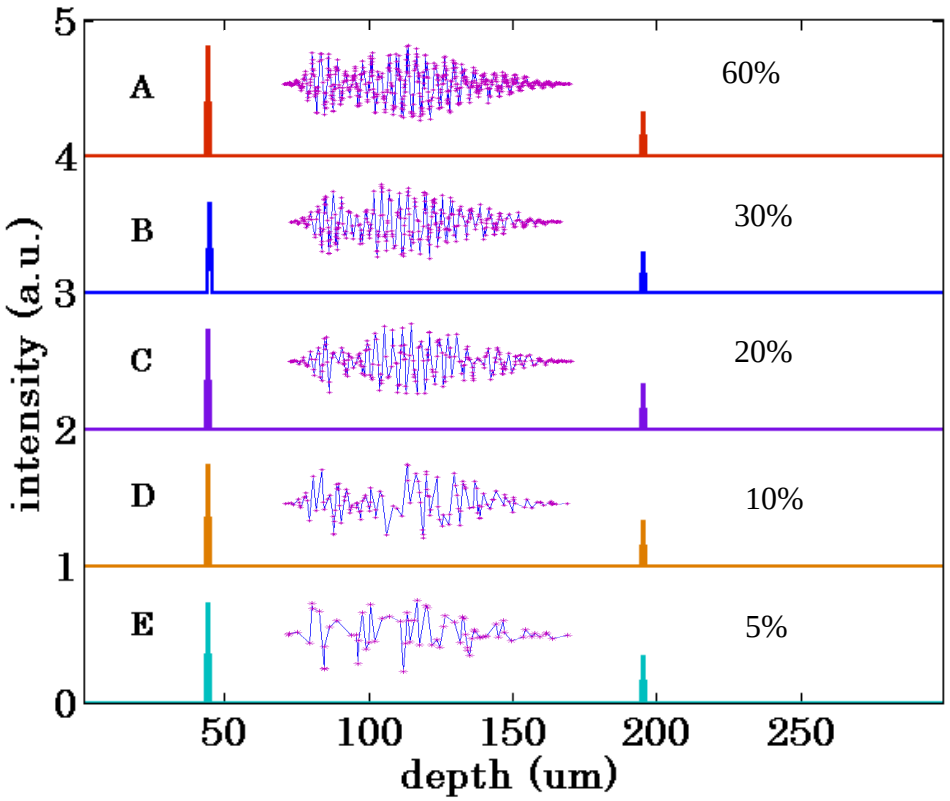

Figure 6.2 Depth profiles reconstructed by the proposed OMP algorithm with 60% (curve A), 30% (curve B), 20% (curve C), 10% (curve D), 5% (curve E). The insets are the uniform random resampled data points.

6.3.3 Improved axial resolution

In the experiment, a narrow band near infrared LED with 35 nm spectral FWHM instead of the broadband SLD was used to characterise the performance of the improved axial resolution. A pellicle beam splitter with a thickness of about 4 μm was

measured by the single-point SD-OCT system. The theoretical axial resolution calculated by Eq. (2.13) is about 7 μm if the refractive index of the pellicle beam splitter is 1.5. Hence the thickness is less than the axial resolution. Fig. 6.3 (a) and (b) show the depth profile and cross-sectional image generated by conventional SD-OCT. The two surfaces of the pellicle beam splitter appear to combine and cannot be distinguished from each other. Fig. 6.3 (b) and (d) show the depth profile and cross-sectional image reconstructed by OMP algorithm. The two surfaces are separated and can be distinguished clearly. Therefore, it can be concluded that, the axial resolution is improved using the OMP algorithm.

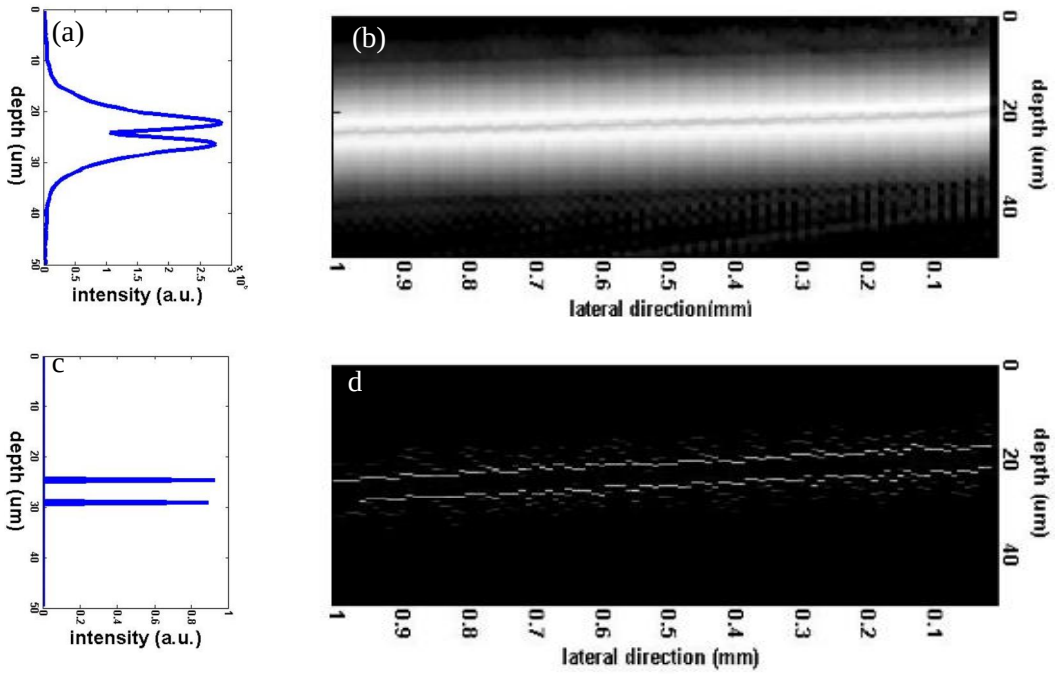

Figure 6.3 (a) Depth profile and (b) cross-sectional image generated by Fourier Transform. (c) Depth profile and (d) cross-sectional image reconstructed by the proposed OMP algorithm in ART-OCT.

6.3.4 Improved imaging depth.

For any given spectrometer, the maximum imaging depth, limited by Shannon-Nyquist sampling theorem, is inverse proportional to its spectral resolution. In order to characterise the imaging depth achieved by OMP, a 150 εm coverslip attached to a 650 εm glass was measured**.** Assuming the refractive index of glass is 1.5, the imaging depth of the conventional SD-OCT method can be calculated as 241 εm which is much less than the total thickness of the glass sample. Fig. 6.4 (a) and (b) are the cross-sectional image and one of the depth profiles generated by FT, the bottom surface feature of the 650 εm was not recovered. However, in Fig. 6.4 (c) and (d), a distinct feature at about 820 εm is clearly visible in the depth profile and cross-sectional image that were reconstructed using the proposed OMP algorithm. Therefore the ART-OCT method can indeed extend the imaging depth of an OCT system. Our experiment results verify earlier work reported by other groups [5, 6].

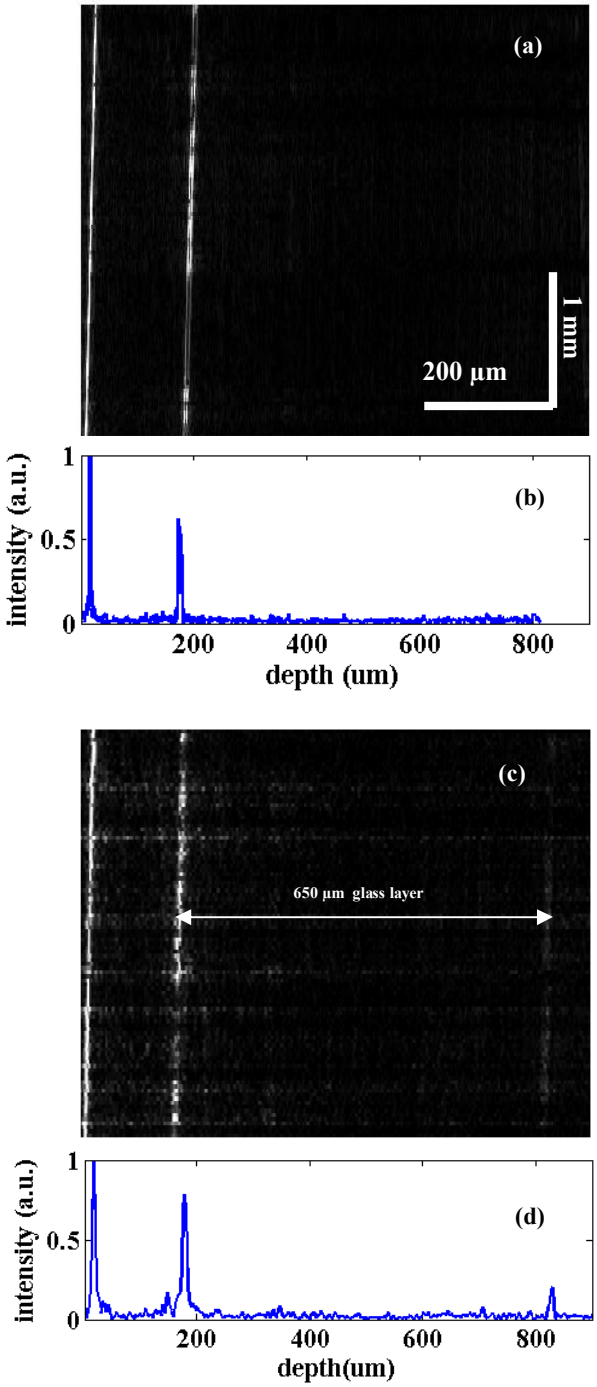

Figure 6.4 Cross-sectional images of a coverslip attached to a thick glass obtained by (a) Fourier transform and (c) OMP algorithm. One of the depth profiles obtained by (b) Fourier Transform and (d) OMP algorithm.

6.3.5 Computational complexity

The computational complexity of L1-optimisation and OMP are $O(N^2M^{3/2})$ and $O(kNM)$ [15], respectively, where k is the given number of non-zero elements in the reconstructed depth profile. N denotes the number of spectral data points used for reconstruction and M represents the total number of elements in depth profile. In the glass sample image reconstruction, M is 300, N is around 700 if the resampling rate is 50%, and the number of non-zero elements k is set as 2. The actual reconstruction time of each method for reconstruction of images with 50% resampling data was recorded in table 1. For a fair comparison, all calculations were performed using Matlab r2013a (hardware specifications: Intel i5 Quad Core CPU at 3.4 GHz, 8.00 GB memory). As shown in Table-1, the actual reconstruction speed of the proposed method is about 25 times faster than that of the L1-optimisation.

Table 1 Reconstruction time of conventional SD-OCT FFT method, L1-optimisation method and the OMP reconstruction method

Method	OMP	L1-optimisation	Conventional SD-OCT
Computational complexity	$O(kNM)$	$O(N^2M^{3/2})$	$O(N\log_2 N)$
Time (s)	0.3	7	0.006

6.4 Spectrum split approach combined with OMP

6.4.1 Spectrum split approach

For the proposed OMP method, it is necessary to set the precise sparsity level of depth profile before reconstruction. In samples that contain many particle-like features, the sparsity level could vary from point to point laterally. Therefore, in order to recover all the scattering features in the sample, a large number of non-zero elements should be predefined. This will result in some pseudo scattering features in the OMP reconstructed depth profile. Here we demonstrated that a spectrum split approach that was initially developed to reduce bulk-motion noise in angiography application [12], can be used to reduce pseudo scattering. As illustrated in Fig. 6.5, the selected differential interferogram data points are split into six separate spectra by

rectangular windows. The adjacent split spectrum could have an overlap. The OMP reconstruction method was subsequently applied to each of the six individual spectra. Real scattering features will be recovered in the same positions in all the sub depth profiles, but the pseudo scattering features appear in different positions. After that, the six recovered sub depth profiles are averaged and smoothed. The pseudo features in the final depth profile will be relatively reduced in contrast to the real scattering features. The spectrum split approach reduces the axial resolution when it is employed in conventional SD-OCT algorithm due to the narrowed bandwidth of the split spectra. But it will not be a drawback in the ART-OCT method because the axial resolution of ART-OCT depends only on the manual given interval of the depth coordinate.

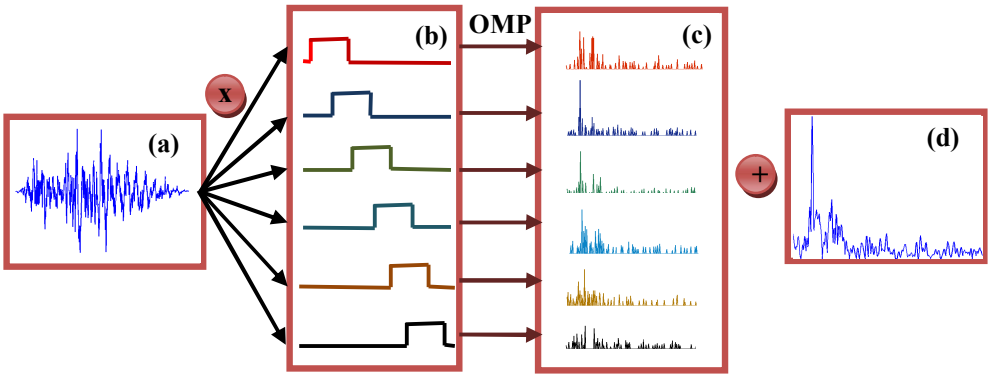

Figure 6.5 Flow chart of the spectrum split method combined with OMP algorithm. (a) Differential interferogram, (b) windowed differential interferograms, (c) sub depth profiles, (d) final depth profile.

6.4.2 OCT imaged reconstructed by OMP combined spectrum split approach

To characterise the performance of the spectrum split approach, a tablet with 1.82 mg/cm^2 weight gain polymer coating was imaged. By using the OMP method directly, the depth coordinate was set from 0 to 450 ɛm with 1.5 ɛm step in air corresponding to 300 ɛm imaging depth and 1 ɛm step if the refractive index is assumed to be 1.5. The number of scattering was set as 50 to ensure all the scattering could be captured. Fig. 6.6 (b) shows one of the recovered depth profiles using the proposed OMP method with the full differential interferogram. There are many

scattering features between 100-300um. The same differential interferogram were then employed to reconstruct using the OMP method with the spectrum split approach. The full spectrum was split into 6 separate spectra by rectangular windows. Each sub-spectra covers 327 pixels, and corresponding to approximately 40 nm in wavelength. The reconstruction settings were the same as in the previous reconstruction. Fig. 6.6 (d) is the final profile obtained by the OMP method with spectrum split approach. In contrast to the depth profile reconstructed by the OMP directly, the features during 100 to 300 um are reduced using the OMP and spectrum split combination. Fig. 6.6 (f) shows a depth profile obtained by conventional SD-OCT combined with the spectrum split approach. The axial resolution was found to have reduced dramatically. Fig. 6.6 (a) (c) and (e) are the cross-sectional images of the tablet coating reconstructed by OMP, OMP with spectrum split and conventional SD-OCT with spectrum split respectively.

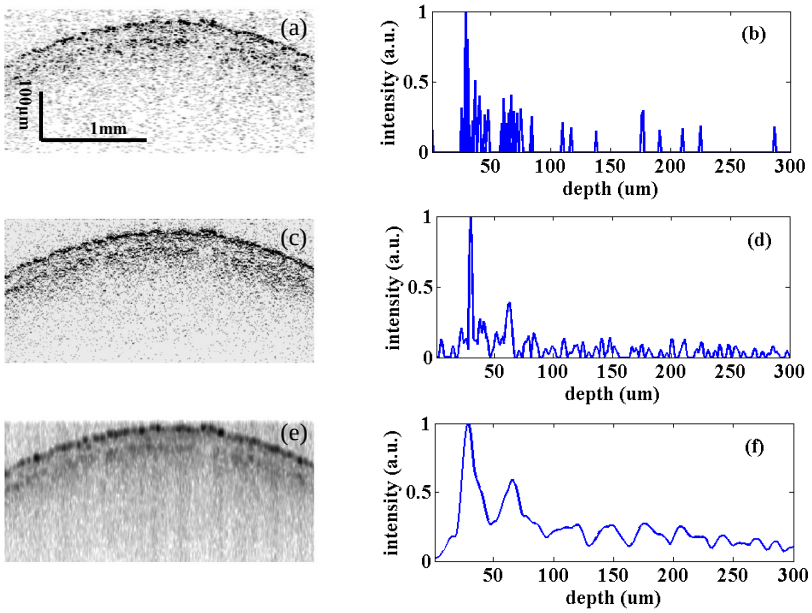

Figure 6.6 Cross-sectional images of a tablet coating with 1.82mg/cm2 weight gain by (a) the OMP algorithm, (c) the OMP algorithm with spectrum split method, (e) conventional SD-OCT algorithm with spectrum split approach. One of the depth profiles of the tablet coating with 1.82mg/cm^2 weight gain by (b) the OMP algorithm, (d) the OMP algorithm combined with spectrum split method, (f) conventional SD-OCT algorithm with spectrum split approach.

6.4.3 Signal to noise ratio

The cross-sectional images of the tablet coated with a polymer weight gain of 5.45 mg/cm^2 were reconstructed using 30%, 50% and 75% random selected measurement data. For fair comparison, the OCT images were reconstructed using both l1-optimisation and the proposed OMP method using the same reconstruction settings as proposed in the previous section. The number of scattering/sparsity level was set to 50 to ensure that all scattering features could be captured. Fig. 6.7(a) - (c) show the cross-sectional images reconstructed using OMP with spectrum split approach. The coating/core interface is clearly visible in all the images reconstructed by the proposed method. However, as shown in Fig. 6.7 (d) - (f), in the cross-sectional images reconstructed using L1-optimisation, it is difficult to see the coating/core interface.

In order to quantify their performance, the SNR [4, 5] is defined as:

$$SNR = 10\log_{10}\left(\frac{\max^2 I(x)}{\frac{1}{N}\sum (I(x)-i(x))^2}\right) \tag{8}$$

where *I(x)* is the image shown in Fig. 6.7 (g) which is obtained by conventional SD-OCT algorithm using 100% of measured interferogram, *i(x)* is the reconstructed image using the proposed method, and N is the total number of pixels in each images. As shown in Fig. 6.7 (h), it is clear that the proposed method provides about 3.7dB improvement in terms of SNR, as compared with the L1-optimisation method.

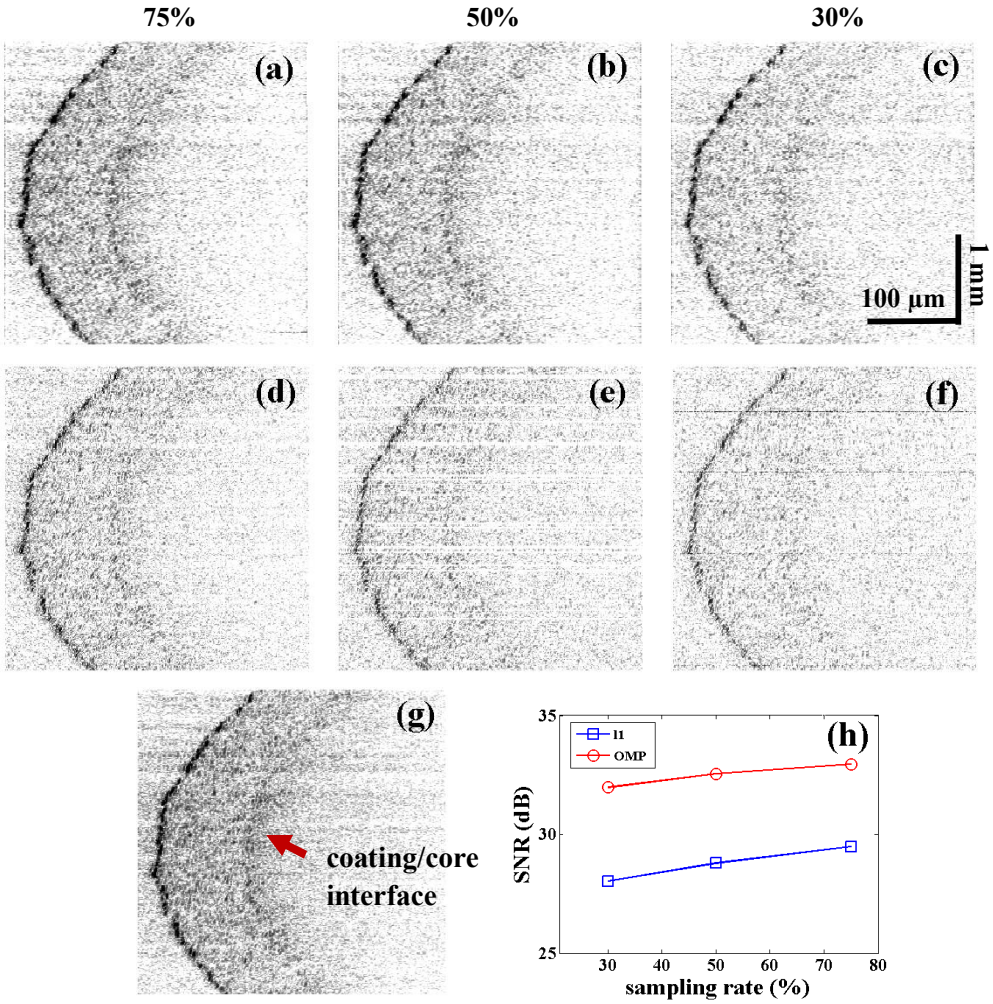

Figure 6.7 OMP reconstructed cross-sectional images of pharmaceutical tablet with weight gain of 5.45 mg/cm2, using (a) 75%, (b) 50%, and (c) 30% randomly selected differential interferogram. L1-reconstructed cross-sectional images of the same tablet using (d) 75%, (e) 50% and (f) 30% randomly selected differential interferogram. (g) Conventional SD-OCT cross-sectional image. (h) SNR of each reconstructed images. All the reconstructed images contain 300 depth profiles and the image size is 3×0.3 mm^2.

6.4.4 Assessment of pharmaceutical tablet coating thickness

In order to validate further the proposed method, both the L1-optimisation and our proposed method were applied to reconstruct the cross-sectional images of all 7 pharmaceutical tablets studied. The reconstruction settings were kept unchanged with a sampling rate of 75%. The reconstructed cross-sectional images are shown in Fig.

6.8. The coating/core interface of all the measured tablet samples are clearly visible in the cross-sectional images reconstructed by our proposed method. However, for L1-optimisation, the coating/core interface of the tablet with the thickest coatings (e.g., with a polymer weight gain of 12.73mg/cm^2) can no longer be recovered.

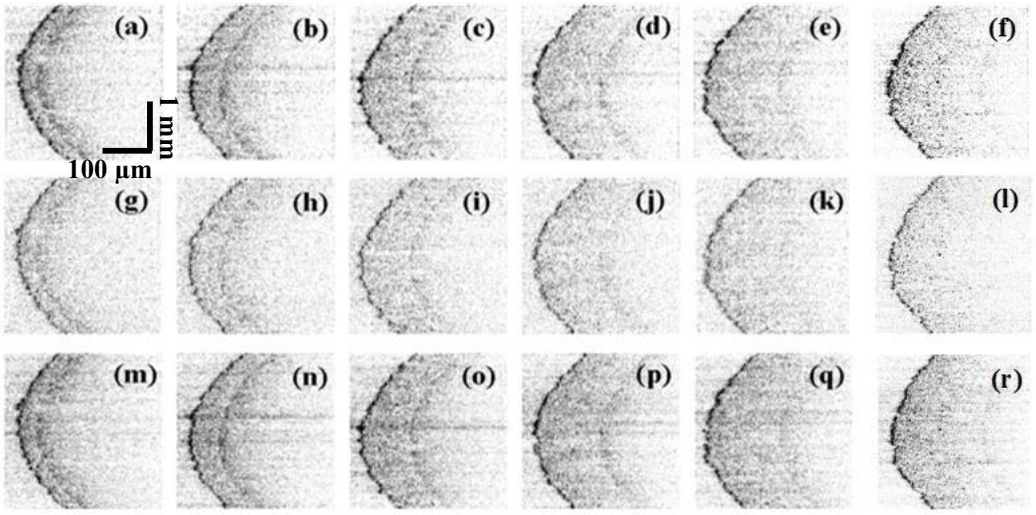

Figure 6.8 Cross-sectional images of tablet coating with weight gain of 1.82 mg/cm^2, 3.64mg/cm^2, 7.27mg/cm^2, 9.09mg/cm^2, 10.91mg/cm^2, and 12.73mg/cm^2 reconstructed by (a) - (f) OMP combined with spectrum split method. (g) - (l) L1-optimisation algorithm, (m) - (i) conventional SD-OCT.

In all the cross-sectional images of the tablets, there are lots of particle-like features. Hence, the position of coating/core peak may not be precisely determined using only a single OCT depth profile. In order to determine the coating thickness in a robust and automatic way, we propose to use the mean depth profile (e.g., averaged over all the 300 reconstructed depth profiles) to calculate the mean coating thickness [18]. Fig. 6.9 (a) shows 5 randomly selected OCT depth profiles of the tablet with a weight gain of 5.45 mg/cm^2. Indeed, there are many particle-like features originating from particles inside a coating layer. Consequently, it is difficult to define and calculate precisely the coating thickness. Fig. 6.9 (b) shows the mean depth profile of this tablet where the coating/core interface at about 105 ε m can be easily identified. Fig. 6.9 (c) shows the mean depth profiles of all 7 measured tablets generated by averaging all 300 reconstructed depth profiles. Again, a distinct peak denotes the coating/core

interface could be resolved. The mean thickness of the tablets can be subsequently calculated as the distance between the surface reflection peak and coating/core interface reflection peaks.

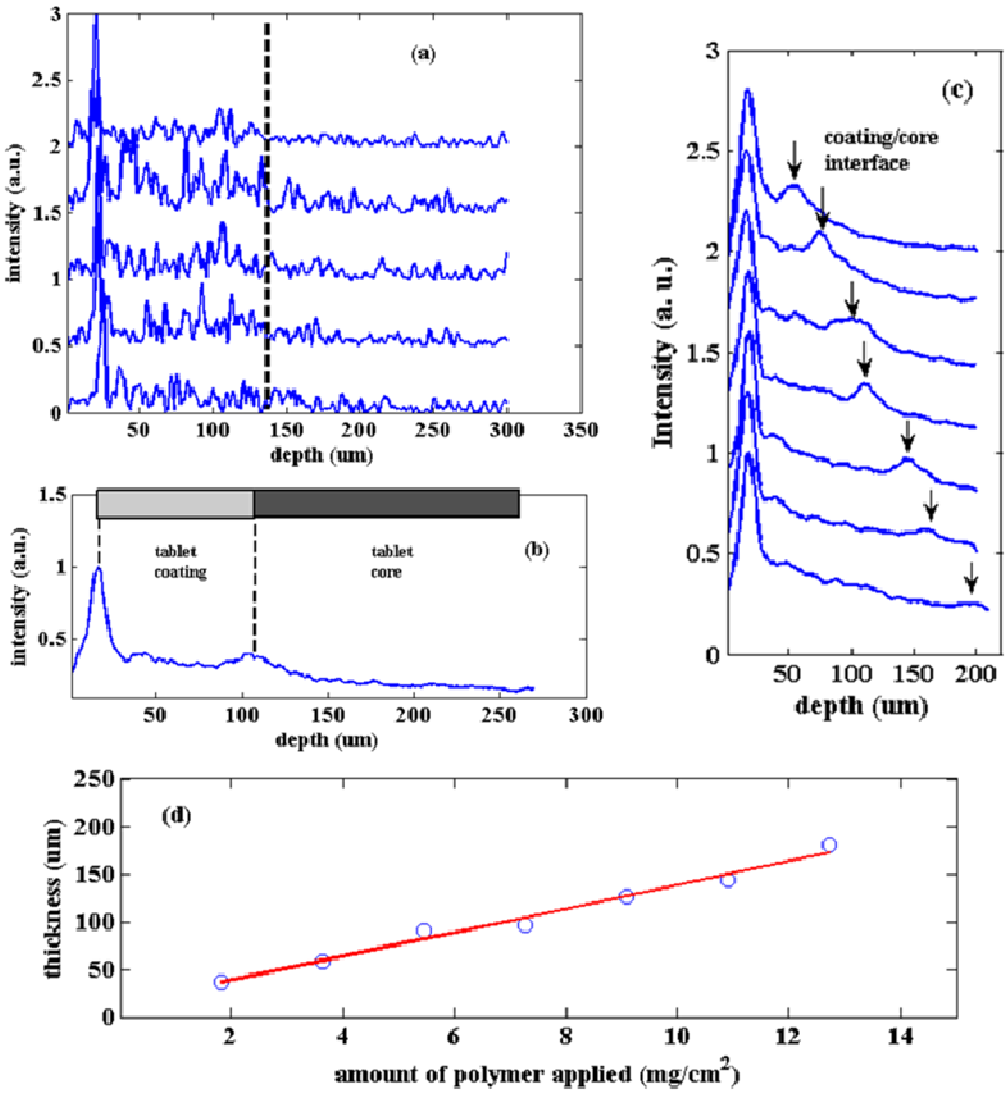

Figure 6.9 (a) Five randomly selected depth profiles and (b) mean depth profiles of the pharmaceutical tablet with weight gain of 5.45 mg/cm^2. (c) Mean depth profiles of all 7 imaged pharmaceutical tablets. (d) The coating thickness is calculated to be 30-180 μm, for the weight gain of 1.82-12.73 mg/cm^2 respectively.

6.5 Summary

In summary, it was found that the fast sparse optimization algorithm, namely OMP, can be used in the ART-OCT for the reconstruction of OCT depth profile. The method can reconstruct the depth profile of a sample directly in wavelength domain, without the need of interpolation. Meanwhile, when combined with a spectrum split approach, our proposed method can applied to extract layer thickness information for real-world pharmaceutical tablet samples. The coating thickness quantified from the reconstructed depth profile is in the range of 30-180 μm. It is also found that the proposed method is about 25 times faster than the more widely used L1-optimization. In addition, the cross-sectional images of the coated tablets reconstructed by our method show better imaging quality in term of SNR.

References:

1. X.A. Liu, and J.U. Kang, ñCompressive SD-OCT: the application of compressive sensing in spectral domain optical coherence tomography,ò Opt. Express **18**: 22010-22019 (2010).
2. H.L. Seck, Y. Zhang, and Y.C. Soh, ñHigh resolution optical coherence tomography by l1-optimization,ò Opt. Commun. **248**: 1752-1759 (2011).
3. H.L. Seck, Y. Zhang, and Y.C. Soh, ñOptical coherence tomography by using frequency measurements in wavelength domain,ò Opt. Express **19**: 1324-1334 (2011).
4. C.Y. Liu, A. Wang, K. Bizheva, P. Fieguth, and H.X. Bie, ñHomotopic, non-local sparse reconstruction of optical coherence tomography imagery,ò Opt. Express **20**: 10200-10211 (2012).
5. S. Schwartz, C.Y. Liu, A. Wang, D.A. Clausi, P. Fieguth, and K. Bizheva, ñEnergy-guided learning approach to compressive FD-OCT,ò Opt. Express **21**: 329-344 (2013).
6. D.G. Xu, N. Vaswani, Y.Huang, and J.U. Kang, ñModified compressive sensing optical coherence tomography with noise reduction,ò Opt. Lett. **37**: 4209-4211 (2012).
7. N. Zhag, T.C. Ho, C.M. Wang, T.Y. Chen, J.G. Zheng, and P.Xue, ñCompressed sensing with linear-in-wavenumber sampling in spectral domain optical coherence tomography,ò Opt. Lett. **37**: 3075-3077 (2012).
8. R. Nayak, and C.S Seelamantula, ñOptimal sparsifying bases for frequency-domain optical coherence tomography,ò Opt. Lett. **37**: 4907-4909 (2012).
9. L.Y. Fang, S.T. Li, Q. Nie, J.A. Izatt, C.A. Toth, and S. Farsiu, ñSparsity based denoising of spectral domain optical coherence tomography images,ò Biomed. Opt. Express **3**: 927-942 (2012).
10. D.G. Xue, Y. Huang, J.U. Kang, "Compressive sensing with dispersion compensation on non-linear wavenumber sampled spectral domain optical coherence tomography," Biomed. Opt. Express **4**: 1519-1532 (2013).

11. D.G. Xue, Y. Huang, J.U. Kang, "Real-time compressive sensing spectral domain optical coherence tomography," Opt. Lett. **39**: 76-79 (2013).

12. Y.L. Jia, O. Tan, J. Tokayer, B. Potsaid, Y.M. Wang, J.J. Liu, M.F. Karus, H. Subhash, J.G. Fujimoto, J. Hornegger, D. Huang, ñSplit-spectrum amplitude-decorrelation angiography with optical coherence tomography,ò Opt. Express **20**: 4710-4725 (2012).

13. R. Leitgeb, C.K. Hitzenberer, and A.F. Fercher, ñPhase shifting algorithm to achieve high speed long depth range probing by frequency domain optical coherence tomography,ò Opt. Lett. **28**:2201-2203 (2000).

14. B. Logan, "Properties of high-pass signals," PhD thesis, Columbia University, 1965.

15. J.A. Tropp, and A.C. Gilbert, ñSignal recovery from random measurements via orthogonal matching pursuit,ò IEEE Trans. Inf. Theory **53**: 4655-4666 (2007).

16. L. I. Rudin, S. Osher, and E. Fatemi, "Nonlinear total variation based noise removal algorithms," Physica D **60**: 259-268 (1992).

17. M. Grant and S. Boyd., CVX: Matlab software for disciplined convex programming (web page and software). http://cvxr.com/cvx/ (2014).

18. C. Li, J.A. Zeitler, Y. Dong, Y.C. Shen, "Non-destructive evaluation of polymer coating structures on pharmaceutical pellets using full-field optical coherence tomography," J. Pharm. Sci. **106**:161-166 (2013).

Chapter 7 Conclusion and future work

7.1 Conclusion

SD-OCT implementation

In conclusion, two types of free space and one fibre based SD-OCT configurations were implemented to investigate the pharmaceutical coating layer structures and real time corneal thickness dynamics.

For the single-point SD-OCT system, a broadband SLD with spectral FWHM of 132 nm was used as the light source. It led to an axial resolution of 2.6 µm. On the other hand, the achieved imaging depth of the system could be either 361 µm or 1800 µm that was dependent on the spectral resolution of the used spectrometer. The lateral scan could be achieved by either scanning the probe/sample beam or laterally moving the sample.

The developed single-shot SD-OCT system utilised the same light source as the single-point system. However, the bandwidth of the spectrometer could not cover all the spectral tange of the light source. Hence the achieved axial resolution was 5µm that was lower than the theoertical one determined by the spectral FWHM of the light source. The spectral resolution of the used spectrometer was 0.1 nm. It result in a imaging depth of 1.8 mm. The single-shot SD-OCT system grabs multiple spectral interferograms in parallel. Hence it can obtain an cross-sectional image without the need for mechanical lateral scan.

The fibre based SD-OCT configuration is much more compact and portable thus is more suitable for inline measurement. It used the same light source and spectrometer as the single-point free space configuration. Thus it has the same axial resolution of 2.6 µm and imaging depth of 1.8 mm that are the same as the single-point free space configuration has.

Pharmacutical application

The single-point free space SD-OCT was demonstrated as an off-line PAT tool to charactersise the coating sturcture of pharmaceutical tablets. A batch of coated tablets with a range of coating thickness were imaged by the single-point SD-OCT system. The mean thickness was determined to be in the range of 30 µm ï 220 µm. Furthermore, two types of small size pharmaceutical pellets with sub-mm diameter were also imaged. We found that the 850 µm pellet has two coating layers and their thickness are determined to be 38 µm and 50 µm respectively. The 350 µm pellet has only one coating layer with a layer thickness of 90 µm.

The single-shot SD-OCT system was employed to study the coating thickness of two selected pharmaceutical tablets as well. It grabbed the volumetric spectral interferograms in a single shot fashion. The volumetic coating maps of the two tablets were extracted from 3200 mean depth profiles. The mean thickness quntified by the mean depth profile is 72 µm and 107 µm that are the same as we obtained by the single-point configuration.

The online measurement of pellet coating was performed on a fibre based SD-OCT configration. Compared with the above-mentioned free space SD-OCT configurations, the fiber based configuration is more compact and portable. The flexible fibre sonsor head can be conviently integrated into a tablet coater for online monitoring and process control. Using the developed fibre-based SD-OCT system, we demonstarted for the first time that the layer thickness of all three coating layers of a moving pellets can be quatified. However, a degradation of axial and lateral resolution was found when the small pellets are moving at high speeds. We believe that this problem can be easily solved by using a high speed spectrometer.

Medical application

The single-shot SD-OCT system was used to study the human and bovine corneal thickness dynamics in real time. The human cornea samples were placed under different perfusion pressures, and the subsequent changes in thicknesses of corneal thickness were measured in real time. We found that the thickness of human cornea

tended to decrease with the increase of perfusion pressure in a range of 100-150 μm. For bovine corneas, two of them showed a similar trend of decreasing in thickness whilst the other three seems changed abnormal in thickness. Furthermore, we proposed to use the SDPM to evaluate the movement of front and back surface and the thickness changes and we found that such movement can be quantified with nanometre scale precision in real time. To the best of my knowledge, this represents the first experimental demonstration that the corneal thickness dynamics can be monitored on multiple lateral pixels simultaneously.

ART-OCT

We proposed a fast sparse approximation algorithm, which combines orthogonal matching pursuit (OMP) method with a spectrum split approach, for the reconstruction of the depth profile of a sample. We demonstrated that 5% random selected spectral data point is sufficient to reconstruct the depth profile of glass slide. We have also showed that the imaging depth has been improved about 3 times as compared with the conventional Fourier Transformed method. In addition, we applied ART-OCT to study pharmaceutical tablet coating in a thickness range of 30-183ε m. We showed that the proposed reconstruction method has low computational complexity which leads a much faster reconstruction speed as compared with the more widely used L1-optimisation method. Furthermore, the novel combination of the OMP method with the spectrum split approach has also led to over 3.7dB improvement in SNR of the reconstructed cross-sectional image of the coated tablets.

7.2 Future works

In-line pellet coating thickness assessment in the coating process

TPI has been demonstrated as a practical in-line technique to determine the coating thickness of tablets during film coating in a pan coating unit. It measures the film coating thickness directly ranging from 40 εm to 1 mm in real time. However, due to its relative larger spatial resolution and lower data acquisition rate, TPI is not suitable for in-line coating thickness measurement of small size pellets with thin coating layers.

Since the SD-OCT is a high resolution and high speed imaging technique, it will be suitable for in-line measurement of both large-sized tablet and small-sized pellet samples with thin coating layers. However, there are still problems to solve. For example, the measurement range of an SD-OCT system is typically several millimetres. The moving pellets/tablets inside a coater might be out of the measurement range. The full-range technique can be used as it can double the measurement range and in the same time be able to remove the mirror items as well. Another problem is the spatial resolution degradation due to limited data acquisition of spectrometer. Either a high speed spectrometer or a pulsed light source with short pulse width could address this issue.

3-D OCT image reconstruction by sparse approximation

One of the advantages of CS or ART technique is that it can significantly reduce the measurement data volume required for imaging reconstruction. The measurement data is typically several Mega Bytes for 2-D B-scan data whereas it could be several Giga Bytes for 3-D data cube. Hence the use of CS or ART technique is more significant to 3-D application. However, the reconstruction speed of the algorithm used in CS and ART technique is much slower than the FT, it takes hours or even days to reconstruct a 3-D OCT image. Hence fast sparse approximation algorithm is required to speed up the reconstruct speed.

Graphic Processing Unit (GPU) and parallel computing to improve imaging speed

Both in-line monitoring and 3-D image reconstruction requires to process large amount of data. The use of parallel computing will improve the image speed by hundreds times.